Chapter 5
Perspectives of Micro and Nanofabrication of Carbon for Electrochemical and Microfluidic Applications

R. Martinez-Duarte, G. Turon Teixidor, P.P. Mukherjee, Q. Kang, and M.J. Madou

Abstract This chapter focuses on glass-like carbons, their method of micro and nanofabrication and their electrochemical and microfluidic applications. At first, the general properties of this material are exposed, followed by its advantages over other forms of carbon and over other materials. After an overview of the carbonization process of organic polymers we delve into the history of glass-like carbon. The bulk of the chapter deals with different fabrication tools and techniques to pattern polymers. It is shown that when it comes to carbon patterning, it is significantly easier and more convenient to shape an organic polymer and carbonize it than to machine carbon directly. Therefore the quality, dimensions and complexity of the final carbon part greatly depend on the polymer structure acting as a precursor. Current fabrication technologies allow for the patterning of polymers in a wide range of dimensions and with a great variety of tools. Even though several fabrication techniques could be employed such as casting, stamping or even Computer Numerical Controlled (CNC) machining, the focus of this chapter is on photolithography, given its precise control over the fabrication process and its reproducibility. Next Generation Lithography (NGL) tools are also covered as a viable way to achieve nanometer-sized carbon features. These tools include electron beam (e-beam), Focused-ion beam (FIB), Nano Imprint Lithography (NIL) and Step-and-Flash Imprint Lithography (SFIL). At last, the use of glass-like carbon in three applications, related to microfluidics and electrochemistry, is discussed: Dielectrophoresis, Electrochemical sensors, and Fuel Cells. It is exposed how in these applications glass-like carbon offers an advantage over other materials.

Keywords Carbon · Glass-like carbon · Carbon MEMS · SU-8 · Photolithography · Electron-beam · Focused ion beam · Nanoimprint lithography · Microfluidics · Dielectrophoresis · Electrochemistry · Nanoelectrodes · Fractal electrodes · Fuel cells

---

R. Martinez-Duarte (✉)
Department of Mechanical and Aerospace Engineering, University of California, Irvine 4200 Engineering Gateway, Irvine, CA 92697, USA
e-mail: drmartnz@gmail.com

S. Chakraborty (ed.), *Microfluidics and Microfabrication*,
DOI 10.1007/978-1-4419-1543-6_5,

5.1 Introduction

Etymologically, the English name for carbon comes from the Latin name for burnt wood, *carbo*. Historically, carbon has played an important role in the daily lives of humans since prehistoric times when it could be commonly encountered as soot and as main component in blac inks for body painting. The use of carbon for odor control is well known and dates back to the Egyptians. Charcoal derivation as we know it today dates back to the Roman civilization. However, it was not until the late 18th century when carbon began to be treated as a chemical element. In 1722, René A. F. de Réaumur demonstrated that iron could be transformed into steel by the absorption of certain substance, now known to be carbon [1]. In 1772 the French scientist Antoine Lavoisier proved that diamond is a crystalline allotrope of carbon by comparing the results from heat treating carbon and diamond samples. In 1779, following a similar method than the one used by Lavoisier, Carl Scheele determined that graphite, considered at the time a form of lead, was indeed another carbon allotrope. Lavoisier later listed Carbon as a separate element in his 1789 textbook *Traité Élémentaire de Chimie* [2]. Carbon is the chemical element with symbol C and atomic number 6. It is nonmetallic, tetravalent and has an atomic weight of 12.0107. Its electron configuration, $1\ s^2 2\ s^2 2p^2$, makes it a member of group 14 and period 2 on the periodic table. Carbon has the highest melting and sublimation point of all elements (3800 K). It forms more compounds than any other element, with almost 10 million pure organic compounds described to date. It is also the fourth most abundant element in the Universe by mass after hydrogen, helium and oxygen. Nevertheless, it is present in all known life forms and in the human body is the second most abundant element by mass (about 18.5%) after oxygen. This abundance and the easiness of carbon to polymerize make this element the chemical basis of all known life on Earth.

5.2 Carbon Allotropes

Several allotropes of carbon exist (see Fig. 5.1 for some examples), resulting in a large variety of molecular configurations for multi-atomic structures. This is partially due to the fact that atomic carbon is a very short-lived species that requires to be promptly stabilized [3, 4]. Carbon allotropes include diamond, lonsdaleite, buckminsterfullerenes, graphene, carbyne [5–11], graphite, carbon nanofoams, diamond-like carbon, amorphous carbon and those carbons derived from the pyrolysis of organic materials, better known as glass-like carbons. It is important to describe these allotropes and show how they compare to glass-like carbon for the reader to understand the advantages and possible disadvantages of the use of the latter in the proposed applications. The physical properties of carbon vary widely with the allotropic form. For example, diamond is highly transparent while graphite is opaque and black; diamond is among the strongest materials while graphite is soft enough to allow its use as solid lubricant; diamond is an excellent electrical insulator while graphite is a good

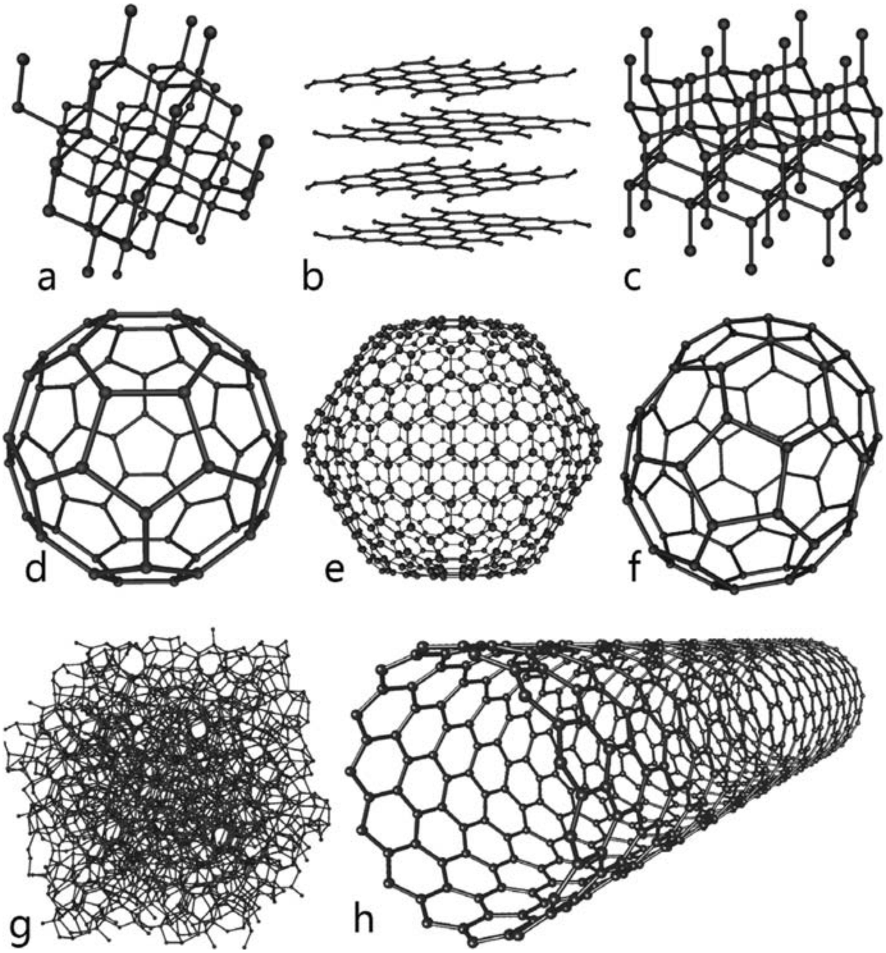

Fig. 5.1 Some carbon allotropes: (**a**) Diamond, (**b**) Graphite and (**c**) Lonsdaleite. Examples of Buckminsterfullerenes: (**d**) C_{60} (buckyball), (**e**) C_{540}, (**f**) C_{70} (**g**) Amorphous carbon, and (**h**) single-walled carbon nanotube. Illustration by Michael Ströck. Reprinted under a GNU free documentation license www.gnu.org

electrical conductor; diamond is the best known naturally occurring thermal conductor but some forms of graphite are used in thermal insulation.

Diamond is an allotrope of carbon that is twice as dense as graphite. It is formed at very high pressures with the conversion of graphite into diamond. The resulting chemical bonding between the carbon atoms is covalent with sp3 hybridization. Diamond has a cubic crystalline structure and is thermodynamically stable at pressures above 6 GPa at room temperature and metastable at atmospheric pressure. At low pressures it turns rapidly into graphite at temperatures above 1900 K in an inert atmosphere.

Lonsdaleite, on the other hand, presents an hexagonal crystalline structure. This carbon allotrope is believed to form from graphite present in meteorites upon their impact on Earth. The sudden great heat and stress of the impact causes graphite to crystallize retaining its hexagonal crystal lattice. With a translucent brownish-yellow color, Lonsdaleite was first discovered in 1967 in the Canyon Diablo meteorite at Barringer Crater (also known as Meteor Crater) in Arizona [12]. Hexagonal diamond was also first lab-synthetized in 1967 by compressing and heating graphite [13].

Buckminsterfullerenes, or fullerenes, are carbon allotropes that have a graphite-like structure but instead of purely hexagonal packing, they also contain pentagonal or even heptagonal carbon rings that bend the sheet into spheres, ellipses or cylinders. Fullerenes are discrete molecular species in contrast to the theoretically infinite lattices of diamond or graphite. Buckyballs, buckytubes (now better known as nanotubes) and nanobuds are all forms of fullerenes. The first fullerene, a soccer-ball-shaped carbon molecule called C_{60} was discovered in 1985 [14]. The name buckminsterfullerenes and its derivatives are given after Richard Buckminster Fuller, the American architect who popularized the use of geodesic domes, which resemble the structure of fullerenes. Interestingly, other names that were considered in the original 1985 publication were ballene, spherene, soccerene and carbosoccer [14].

A basic structural element of some forms of fullerenes (such as nanotubes) is graphene. Graphene is a one-atom-thick sheet of hexagonally arranged carbon atoms. The term graphene appeared in the late 1980s but was not experimentally derived until 2004 [15] and not characterized until 2007 [16]. Graphene is the strongest material known to man, 200 times stronger than steel, and as of 2008, one of the most expensive [17].

Graphite is formed by stacking graphene layers parallel to each other in a three-dimensional, crystalline, long-range order. There are two allotropic forms with different stacking arrangements: hexagonal and rombohedral, but the chemical bonds within the layers are covalent with sp2 hybridization in both cases. Carbon atoms in graphite, as in graphene, are bonded trigonally in a plane composed of fused hexagonal rings. The resulting network is 2-dimensional and the resulting flat sheets are stacked and loosely bound through weak Van der Waals forces. Because of the delocalization of one of the outer electrons of each atom to form a π-cloud, graphite conducts electricity preferentially in the plane parallel to the covalently bonded sheets.

Carbon nanofoam is yet another carbon allotrope discovered as recently as 1997 [18]. It consists of a low-density cluster of carbon atoms strung together in a loose three-dimensional web. Each cluster is about 6 nanometers wide and consists of about 4000 carbon atoms linked in graphite-like sheets. The clusters present a negative curvature by the inclusion of heptagons among the regular hexagonal pattern. Up to this date, it has been synthesized by high-repetition-rate laser ablation of an ultrapure carbon target in Ar environment [18–21]. The large-scale structure of carbon nanofoam is similar to that of an aerogel, yet unlike carbon aerogels, carbon nanofoam has a high electrical resistance. The most unusual feature of this allotrope is its attraction to magnets and its capability to become magnetic below 90 K [20, 21].

Other family of allotropes that feature a certain degree of amorphousness are the diamond-like carbon (DLC) films [22–27]. These films are hard and present a significant fraction of sp3 hybridized carbon atoms that can contain a significant amount of hydrogen atoms. Depending on the deposition conditions, these films can be fully amorphous or contain diamond crystallites. The deposition parameters are (low) total pressure, hydrogen partial pressure, type of precursor molecules, and use (or not) of plasma ionization. High ionization favors amorphous films while high atomic hydrogen contents favor diamond crystallite formation. Because of the confusion about structure generated by the term "diamond-like carbon" films, the term "hard amorphous carbon" has also been suggested as a synonym [28].

Amorphous carbon is an assortment of carbon atoms in a non-crystalline, irregular state that is essentially graphite without a crystalline macrostructure. Short range order exists, but with deviations in the interatomic distances and/or interbonding angles with respect to the graphite and diamond lattices. The term amorphous carbon is restricted to the description of carbon materials with localized π-electrons as described in [29]. Deviations in the bond angles occur in such materials because of the presence of "dangling bonds". This description of amorphous carbon is not applicable to carbon materials with two-dimensional structural elements, such as the ones present in all pyrolysis residues of carbon compounds. Even if coal, soot, carbon black and glass-like carbons are informally called amorphous carbon, they are products of pyrolysis, which does not produce true amorphous carbon under normal conditions [28]. Glass-like carbon is an allotrope with a very high isotropy of its structural and physical properties and with a very low permeability for liquids and gases. The original surfaces and the fracture surfaces have a pseudo-glassy appearance. Glass-like carbons cannot be described as amorphous carbon because they consist of two-dimensional structural elements and do not exhibit "dangling" bonds.

5.3 Glass-Like Carbons

Glass-like carbons are derived through the carbonization, or thermal degradation, of organic polymers in inert atmospheres. The resultant carbon has a glass-like appearance in the sense that is smooth, shiny and exhibits a conchoidal fracture[1] [30]. Because of its appearance, glass-like carbon has also been referred historically as "vitreous carbon" or "glassy carbon". It is impermeable to gases and extremely

---

[1] Some crystals do not usually break in any particular direction, reflecting roughly equal bond strengths throughout the crystal structure. Breakage in such materials is known as fracture. The term conchoidal is used to describe fracture with smooth, curved surfaces that resemble the interior of a seashell; it is commonly observed in quartz and glass. Conchoidal fracture. (2009). In Encyclopaedia Britannica. Retrieved April 08, 2009, from Encyclopaedia Britannica Online: http://www.britannica.com

inert, with a remarkable resistance to chemical attack from strong acids such as nitric, sulfuric, hydrofluoric or chromic and other corrosive agents such as bromine. Even when it does react with oxygen it only does so at high temperatures. Its rates of oxidation in oxygen, carbon dioxide or water vapor are lower than those of any other carbon. It has a hardness of 6–7 on Mohs' scale, a value comparable to that of quartz. Its density ranges from 1.4 to about 1.5 g/cm^{-3}, compared to 2.3 g/cm^{-3} for graphite, which suggests a significant degree of porosity. X-ray diffraction studies have shown that glass-like carbon presents an extremely small pore size of a closed nature, and that has an amorphous structure [31–38]. Glass-like carbon features a coefficient of thermal expansion of 2.2–3.2 $\times$ 10^{-6}/K which is similar to some borosilicate glasses. Its Young Modulus varies between 10 and 40 GPa. Because its thermal conductivity is about a tenth of that of typical graphite, it has been considered as thermally inert [39–44]. Glass-like carbon also has a wider electrochemical stability window than platinum and gold, which makes it ideal in electrochemistry experiments [45]. Even when the overall properties of the resulting carbon depend on the nature of the precursor used, they do not change very significantly [46] and the above values could be employed as an initial reference. Up to this date a consensus on the crystalline structure of glass-like carbon has not been reached. The most widely known and accepted model is the one that considers this type of carbon as made up of tangled and wrinkled aromatic ribbon molecules that are randomly cross-linked by carbon-carbon covalent bonds as shown in Fig. 5.2. The ribbon molecules form a networked structure, the unit of which is a stack of high strained aromatic ribbon molecules. Such structure of crystallites reflects the features of thermosetting resins structure which are commonly used as precursors for glass-like carbons. This model explains the most experimental results obtained so far on glass-like carbons including its impermeability, brittleness and conductivity [44, 46–49]. Other models exist including the "oxygenated Tetrahedral-Graphitic parts" model of Kakinoki [47], the "crumpled sheets" model of Oberlin [38], the "closed pores" model by Shiraishi [50] and the "globular" model by Fedorov [51]. Excellent reviews on the structure of glass-like carbon can be found in [44] and [49]. While the physical structure and chemical properties of glass-like carbons have been

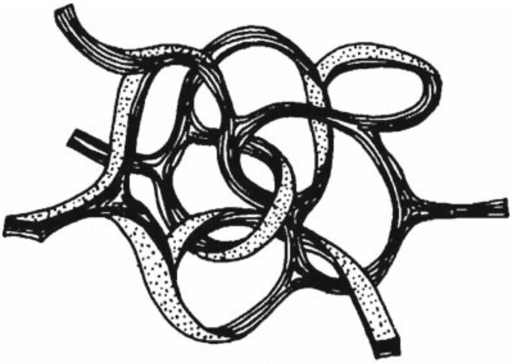

Fig. 5.2 Structural model of glass-like carbon as proposed by Jenkins in 1971. This model is able to explain most of the properties exhibit by glass-like carbon up to this day. Adapted by permission from Macmillan Publishers Ltd: Nature, from Jenkins and Kawamura [48] copyright 1971

extensively studied and debated since the early 1960s it was not until recent years when extended studies on the electric and electronic properties of this carbon appeared [49, 52, 53].

Carbonization is the process by which solid residues with a high content of carbon are obtained from organic materials, usually by pyrolysis in an inert atmosphere [28]. Different precursors to obtain glass-like carbon may be used, including phenolic resins, polyfurfuryl alcohols, cellulose, polyvinyl chloride and polyimides [34, 44, 46, 54–64]. Different degrees of shrinkage and carbon yield (the ratio of the weight of carbon to the weight of the original polymer sample) are obtained during carbonization depending on the precursor used. Phenol-formaldehyde, polyfurfuryl alcohol and polyvinyl alcohol have the highest yields, with an approximate 50% carbon [44]. Novolac resins, or acid-catalyzed phenol formaldehyde resins, are commonly used as photoresists and have recently become the material of choice to derive carbon structures featuring micro and nano dimensions. Their volume shrinkage varies from 50 to 90% [45, 65–67]. As with all pyrolytic reactions, carbonization is a complex process with many reactions taking place concurrently, including dehydrogenation, condensation, hydrogen transfer and isomerization [68–76]. The pyrolysis process of organic compounds can be divided into three major steps: pre-carbonization, carbonization and annealing. During pre-carbonization ($T < 573$ K) molecules of solvent and unreacted monomer are eliminated from the polymeric precursor. The carbonization step can be further divided into two stages. From 573 to 773 K (300 to 500°C), heteroatoms such as oxygen and halogens are eliminated causing a rapid loss of mass while a network of conjugated carbon systems is formed. Hydrogen atoms start being eliminated towards the end of this stage. The second stage of carbonization, from 773 to 1473 K (500 to 1200°C), completely eliminates hydrogen, oxygen and nitrogen atoms and forces the aromatic network to become interconnected. At this point, permeability decreases and density, hardness, Young's modulus and electrical conductivity increase. Sulfur does not evolve until even higher temperatures (> 1800 K), and certain metallic impurities, e.g. iron, may even require a leaching process to be eliminated. The final step, annealing, is carried out at temperatures above 1473 K, allowing to gradually eliminate any structural defects and evolve further impurities [44]. The final pyrolysis temperature determines the degree of carbonization and the residual content of foreign elements. For instance, at $\mathrm{T}{\sim}1200$ K the carbon content of the residue exceeds a mass fraction of 90% in weight, whereas at $\mathrm{T}{\sim}1600$ K more than 99% carbon is found [34, 73, 77]. Glass-like carbon is characterized as a type of Char[2] and is classified as a non-graphitizable, or non-graphitizing, carbon. It is important to mention that glass-like carbon is usually derived from thermosetting resins which do not melt during the carbonization process but rather maintain their shape

---

[2] Char is a solid decomposition product of a natural or synthetic organic material. If the precursor has not passed through a fluid stage, char will retain the characteristic shape of the precursor (although becoming of smaller size). For such materials the term "pseudomorphous" has been used. In contrast, coke is produced by pyrolysis of organic materials that have passed, at least in part, through a liquid or liquid-crystalline state during the carbonization process.

along the process. Glass-like carbon does not graphitize even when heat treated at 3273 K (3000°C). The inability of the graphitic planes to grow and stack parallel to each other even at high temperatures is due to the entangled nature of glass-like carbon structure, as mentioned above. Non-graphitizable carbons are mechanically hard and are sometimes referred as hard carbons [78]. For the sake of clarity, even when the term pyrolytic carbon might suggest a synonym for glass-like carbons, the former term only refers to carbon materials deposited from gaseous hydrocarbon compounds. The term pyrolytic carbon does not describe the large range of carbon materials obtained by thermal degradation (thermolysis, pyrolysis) of organic compounds when they are not formed by chemical vapor deposition. Materials deposited by physical vapor deposition are not covered either by the term pyrolytic carbon. Fig. 5.4 illustrates a variety of carbon products obtained with different processes.

The first derivation of a carbon material from a phenolic resin appears to be from 1915, when Weintraub and Miller in Massachusetts derived disks of a "very bright, shiny looking carbon with hardness equal or greater than 6 on the Mohs mineral scale". These disks were used to improve the useful life of microphones employed in telephone transmitters. In their patent, they describe the slowly heating of a hardened resin to a temperature close to 700°C in about one week and the subsequent firing at temperatures from 800 to 1100°C in a few hours. They also recognized the alternative and easiness of shaping the resist prior to carbonization instead of directly machining carbon [80]. A sustained flow of publications on glass-like carbon did not begin until 1962, when Davidson at the General Electric Co. in Kent, England derived glass-like carbon from cellulose [81] and Yamada and Sato, at the Tokai Electrode Manufacturing Co. in Nagoya, Japan, published preliminary characterization results of carbon derived from organic polymers, which they referred to as glassy carbon [39]. In 1963 Lewis, Redfern and Cowlard postulated a similar glass-like carbon, named "vitreous carbon" by the authors, as an ideal crucible material for semiconductors [40]. Later that year, Redfern disclosed several production processes to derive this vitreous carbon in a patent [82]. Redfern, Lewis and Cowlard worked for the Plessey Company in the United Kingdom. In 1965, X-ray studies of the material were conducted by Bragg at the Lockheed Missiles and Space Co. in Palo Alto, CA [31], while their tensile properties and pore size were characterized by Kotlensky at the Jet Propulsion Laboratory in Pasadena, CA [83] and a preliminary model of the structure was published by Kakinoki in Osaka, Japan [47]. That same year the advantages of glassy carbon electrodes for voltammetry and analytical chemistry were characterized by Zittel and Miller from Oak Ridge National Laboratory using a proprietary glassy carbon from the Tokai Electrode Manufacturing Co. [84] while Lee explored the mechanics of thermal degradation of phenolic condensation polymers [68]. In 1967, Cowlard and Lewis published a detailed description of the properties of vitreous carbon, the fabrication process and its potential applications [41]. In 1968, Rothwell conducted a more detailed study on the small-angle X-ray scattering of glassy carbon upon the suggestion of Bragg in Palo Alto [32]. Starting in 1969, glassy carbon was already receiving mainstream attention and started to be reviewed by different authors [42, 55]. That same year, Halpin and Jenkins studied its interaction with alkali metals and

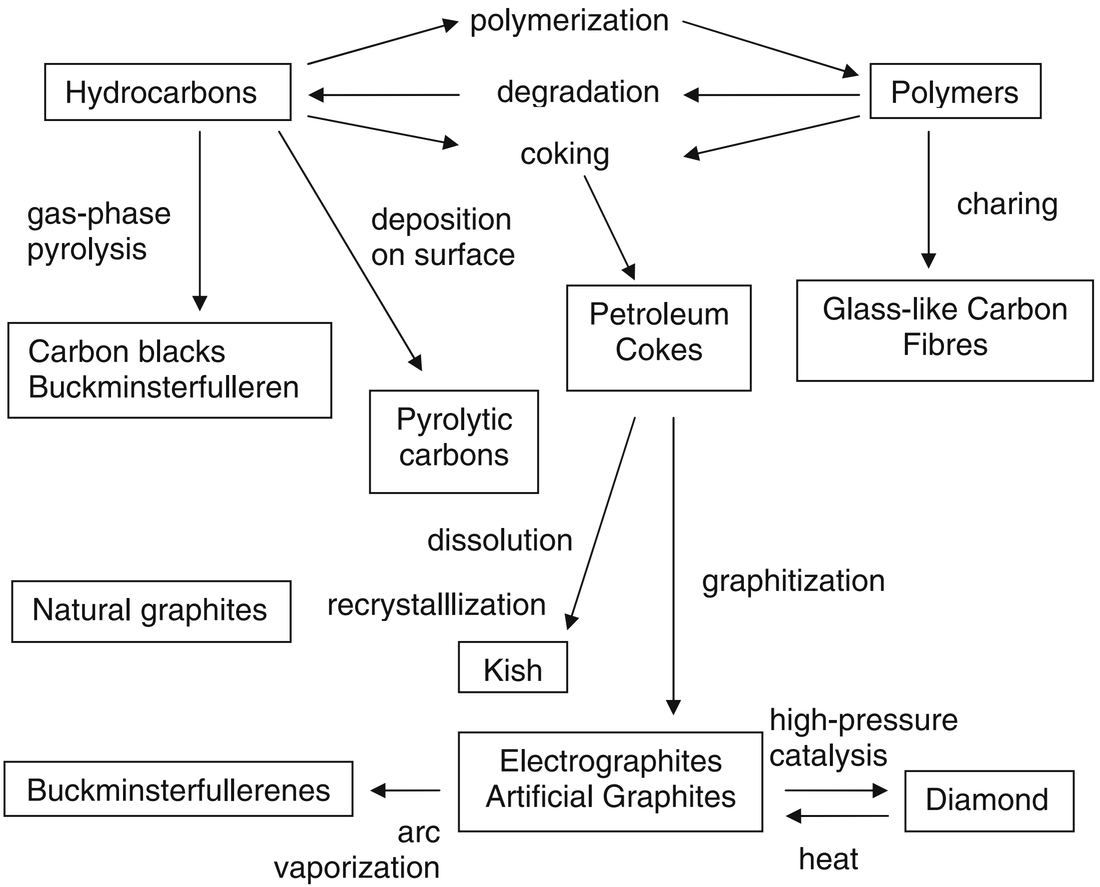

Fig. 5.3 Carbon products obtained by different processes. Adapted from Pocard et al. [79] – Reproduced by permission of The Royal Society of Chemistry

demonstrated potassium intercalation in glassy carbon [43]; Fitzer and Schafer delved on the formation of glasslike carbon by pyrolysis of polyfurfuryl alcohol and phenolic resins [54] and Lewis, Murdoch and Moul published on the heat of combustion of vitreous carbon [85]. In 1970, Fitzer and Schafer further studied the effect of crosslinking on the formation of glasslike carbons from thermosetting resins [69]. At the same time, Benson suggested the use of this carbon as implantable material in the human body [86] and reviewed the advantages of elemental carbon as a biomaterial [87]. The decade of 1970 brought a significant interest on the use of glassy carbon as a material for different implants and biomedical instrumentation. A large volume of publications exist, few examples are [88–95]. In 1971 a new structural model was postulated by Jenkins and Kawamura which was further corroborated in 1972 [46, 48]. This model is up to date the only one capable of explaining most of the experimental results obtained with glass-like carbon in the last 40 years [49]. Other models were later suggested in 1978 [51], 1983 [38], 1984 [50] and 2002 [52]. Further characterization of glass-like carbon was done by Williams, Dobbs and Taylor, who investigated the optical properties [96], fracture behavior [30] and electron-transfer kinetics [97] of glassy carbon respectively. Nathan conducted Raman spectroscopy on glassy carbon in 1974 [98]. The 1970s also witnessed an explosion of the interest on glassy carbon by the analytical and electrochemistry communities which still remains strong [37, 58–60, 79, 99–106]. In 1990, a novel synthesis of glassy carbons at relatively low temperatures (600°C) yielded to homogeneously doped glassy carbon (DGC) materials for electrochemistry [58–60, 79]. Few reviews on the contemporary state-of-the-art of glass-like carbon exist for different years [44, 49, 107–109]. As it can be seen from the historic review above, the same material -carbon derived from organic polymers by pyrolysis in inert atmosphere- was referred to with three different names: vitreous carbon, glassy carbon or glass-like carbon. The term vitreous carbon was first introduced by Redfern, Lewis and Cowlard at the Plessey Company in 1963. Although highly referenced in implant-related publications during the 1970s, the term vitreous carbon started to fall in disuse by the end of that decade. Vitreous carbon is now better identified with Reticulated Vitreous Carbon (RVC), a material introduced in the late 70s by Chemotronics International Inc. from Ann Arbor, MI. The use of RVC in electrochemistry was first documented in 1977 by [101] and was dubbed “optical transparent vitreous carbon”. Extensive reviews on RVC are given in [110] and [111] . The term “glassy carbon” was introduced by Yamada and Sato at the Tokai Electrode Manufacturing Corporation in 1962. The commercialization of Tokai’s glassy carbon electrodes targeting the electrochemistry market made glassy carbon the term of preference for the electroanalytical chemistry community to refer to glass-like carbon. In 1995 the IUPAC (International Union of Pure and Applied Chemistry) defined glass-like carbon as the material derived by the pyrolysis of organic polymers and recommended that the terms “Glassy carbon” and “Vitreous carbon”, which had been introduced as trademarks, should not be used as synonymous for glass-like carbon. From a scientific viewpoint, the terms vitreous and glassy suggest a similarity with the structure of silicate glasses which does not exist in glass-like carbon, except for the pseudo-glassy appearance of the surface

[28]. Since the 1960s the term glass-like carbon has been the term of choice in most of the publications dealing with the mechanisms of thermal degradation and pyrolysis of polymer precursors. The latest review on glass-like carbon was published in 2002 by Pesin [49].

From the microfabrication standpoint, glass-like carbon microstructures were not reported until the late 1990s by Schueller and co-workers at Harvard University. In their process, polydimethylsiloxane (PDMS) molds were fabricated using soft lithography and then used to pattern furfuryl alcohol-modified phenolic resins and phenol-formaldehyde resins, which were subsequently carbonized [61, 112–115]. This fabrication technique allowed them to work with flat or curved surfaces and derive different structures (including free-standing lateral comb drives, diffraction gratings and grids) with dimensions as small as a few micrometers and featuring high aspect ratios if desired [115]. Microelectromechanical functions were also demonstrated [112]. During the same decade, initial work on the derivation of carbon from photoresists emerged in the quest for alternatives to carbon films produced by physical deposition techniques. The interest was driven by the use of pyrolyzed photoresists in batteries, electrochemical sensors, capacitors and MicroElectroMechanical Systems (MEMS). Electrochemical studies of carbon films derived from positive photoresists were conducted in 1998 by Kim et al. in Berkeley, CA [64] and later by Ranganathan et al. [65] at Ohio State University (OSU). By 2000, Kostecki, Song, and Kinoshita patterned these carbon films as microelectrodes and studied the influence of the geometry in their electrochemical response [116]. Pyrolyzed Photoresist Films, or PPF, still derived from positive resists were surface-characterized in 2001 and determined to have a near-atomic flatness [117]. The resultant carbon showed an electrochemical behavior similar to glass-like carbon although with decreased surface roughness. In 2002 the derivation of carbon from negative photoresists was reported by Singh, Jayaram, Madou, and Akbar at OSU. They used SU-8, a relatively new epoxy-based photoresist at that time [118, 119], and polyimide to fabricate circular patterns. The carbon obtained with this precursor showed higher resistivity and vertical shrinkage than the one synthesized from positive resists. Furthermore, the carbon derived from SU-8 showed higher vertical shrinkage and poorer substrate adhesion than that from polyimide. Nevertheless, resistivity from SU-8 carbon was slightly lower than polyimide's [66]. In 2005, structures with aspect ratios higher than 10 were reported by Wang, Jia, Taherabadi, and Madou at the University of California, Irvine (UCI). This achievement was possible thanks to the use of a two-step heating process during pyrolysis. This novel process allowed for the release of residual oxygen contained in the polymer structures that had caused the precursor to burn rather than pyrolyze, even in an oxygen-free atmosphere. A variety of complex high-aspect ratio Carbon-MEMS (C-MEMS) structures, such as posts, suspended carbon wires, bridges, plates, self organized bunched posts and networks, were built in this way. The variation in structure shrinkage depending on the original polymer was also reported [45, 120]. For example, structures with thickness below 10 μm usually shrink approximately by 90%, while hundreds-of-microns thick features shrink approximately 50%. Also in 2005, the electrical properties and shrinkage behavior of both positive and negative resists after pyrolysis were characterized by Park and co-workers at UCI. They corroborated the decrease in resistivity of glass-like carbons as the pyrolysis final temperature increases. They also demonstrated how the largest shrinkage takes place below 873 K (600°C) for all the photoresists tested [121]. Electron beam lithography (EBL) was used in 2006 to fabricate suspended glass-like carbon microstructures [67]. Continuous work on C-MEMS has been conducted since 2004 by the same group at UCI and collaborators in a variety of applications including Lithium-ion batteries [122–125], fuel cells [126, 127], electrochemical sensors [128], cell culturing substrates [129], dielectrophoresis [130–137], micromolding [138] and fractal electrodes [139, 140]. Other groups have also recently integrated carbon structures for their use in gas sensors [141].

The development of novel fabrication techniques keeps reducing the smallest dimensions that can be achieved in carbon. While 40 years ago glass-like carbon was only used in applications requiring large dimensions, such as metallurgy crucibles and laboratory beakers, it can now be employed to fabricate nano-electrodes. Its unique properties have been beneficial to various applications along the years. Initially, its extreme chemical inertness and gas impermeability were exploited to fabricate laboratory equipment such as beakers, basins and boats. Since glass-like carbon is not wetted by a wide range of molten metals, it is an ideal material for the fabrication of crucibles with applications in metallurgical and chemical engineering. Its resistance to erosion and high melting point makes it an ideal material for mandrels, steam, fuel and rocket nozzles and other equipment in mechanical and electrical applications. Moreover, glass-like carbon has also been used in heart valve implants and other biomedical devices thanks to its biocompatibility. "Glassy" carbon electrodes have become so popular that they represent a significant fraction of the multi-billion electrochemistry market.

Carbon-MEMS (or C-MEMS) can be defined as the set of methods that can be used to derive glass-like carbon structures from patterned organic polymers, featuring dimensions ranging from hundreds of micrometers down to tens of nanometers. C-MEMS combines different polymer micro and nanofabrication techniques with pyrolysis or thermal degradation to derive glass-like carbon features. These fabrication techniques include, but are not limited to, stamping, casting, machining and lithography. The choice of each technique is dictated by the quality, complexity and final dimensions of the desired carbon part. In this regard, the incorporation of photolithography (shown in Fig. 5.4) to the C-MEMS toolbox enabled a more precise control on the dimensions and complexity of the precursor polymer structures. The addition of Next-Generation Lithography (NGL) techniques, such as electron beam lithography (EBL), nanoimprint lithography (NIL) and focused-ion beam (FIB), will further reduce the dimensions and greatly increase the intricacy of the resulting carbon structures. Moreover, the existence of commercial high-quality precursors and standardized photolithography tools make the fabrication process and the dimensional control highly reproducible. The fabrication of high-aspect ratio structures [45], nano-electrodes, overhanging motifs [67], free-standing all-carbon micromolds [138] and the integration of carbon electrodes in polymer devices [134, 135, 141] are included in the latest achieved milestones.

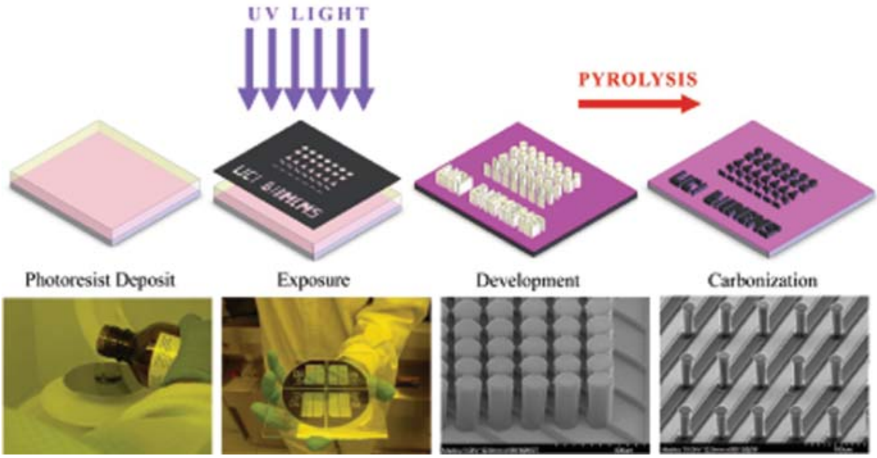

Fig. 5.4 Schematics and figures depicting the C-MEMS process when using photolithography. The case of a negative tone resist is pictured

It is important to differentiate the fabrication of glass-like carbon with nanometer dimensions, as in the case of electrodes derived from polymers patterned with NGL techniques, from the use of Carbon NanoTubes (CNT). One of the main differences is that micro and nanofabrication methods achieve a wider range of length scales, from a few nanometers to several millimeters. In the case of CNT, the dimensions are limited between 1 and 100 nm, depending on the synthesis method being used, the type of CNT (single-walled or multi-walled) [142] and the size of the catalytic particles used to synthesize them [143]. An additional advantage of using NGL methods to pattern carbon is the enhanced placement precision, since the structure geometry is pre-determined using lithography methods. On the other hand, the growth of CNT cannot be pre-patterned, and they need to be positioned after processing when they are to be used individually.

As stated above, the embracing of photolithography in the micro and nanofabrication of glass-like carbon has brought significant advantages and enabled rapid and notable developments. In the following section, the focus is on the derivation of polymer structures using photolithographic methods. Next Generation Lithography technologies are then presented as an alternative to achieve smaller and more complex patterns than those possible with photolithography.

5.4 Photolithography Overview

The most widely used form of lithography is photolithography which is basically the use of light to pattern the substrates. In the Integrated Circuits (IC) industry, pattern transfer from masks onto thin films is accomplished almost exclusively via photolithography. This essentially two-dimensional process has a limited tolerance for non-planar topographies and creates a major constraint for building non-IC miniaturized systems, such as microfluidic devices and polymer precursors for C-MEMS.

Fortunately, research over the last ten years in high-aspect-ratio resists is finally improving dramatically photolithography's capabilities, allowing for it to cover wider ranges of topographies and to resolve ever-smaller features. Performance of a photolithographic process is determined by its resolution (the minimum feature size that can be transferred with high fidelity), the registration (how accurately patterns on successive masks can be aligned), and throughput (the number of parts or devices that can be transferred per hour, a measure of the efficiency of the lithographic process).

Photolithography generally involves a set of basic processing steps: photoresist deposition, soft bake, exposure, post-exposure treatment and developing. Descumming and post-baking might also be part of the process is illustrated in Fig. 5.5. Each one of these steps are detailed below, together with their related topics. For example, alternatives to spin coating for resist deposition are explored, and the properties and types of resists are discussed. Different masking techniques that can be used during the exposure step are also presented.

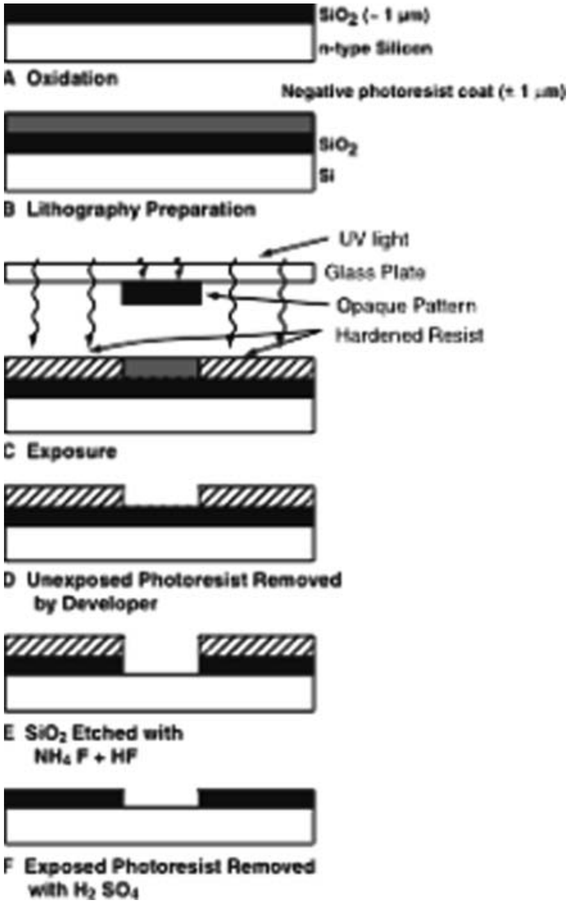

Fig. 5.5 Basic photolithography and pattern transfer. Example uses an oxidized Si wafer and a negative photoresist system. Process steps include exposure, development, oxide etching, and resist stripping. Steps B to D are detailed in the text. For details on steps A, E and F refer to [144]

5.4.1 Substrate Cleaning and the Clean Room

Substrate cleaning is the first and a very important step in any lithographic process, as the adhesion of the resist to the substrate could be severely compromised by the presence of impurities and residual coatings if it is not carried out properly. Contaminants include solvent stains (methyl alcohol, acetone, trichloroethylene, isopropyl alcohol, xylene, etc.), and airborne dust particles from operators, equipment, smoke, etc. In the manufacturing of MEMS and NEMS devices, several substrate choices are available: silicon, glass, quartz, metals and even polymer films such as polyimide (PI) and polyester (PET). Depending on the substrate and the type of contaminants, several cleaning techniques can be used. Wet immersion cleaning might be carried out using diluted hydrofluoric acid, Piranha (a mix of sulfuric acid and hydrogen peroxide at different ratios), RCA (a process involving ammonium hydroxide, hydrogen peroxide, water, hydrofluoric and hydrochloric acids at different stages) or milder, but not as effective, procedures such as DI water rinsing followed by solvent rinse. Other methods include ultrasonic agitation, polishing with abrasive compounds, and supercritical cleaning. Dry methods include vapor cleaning; thermal treatments, for example baking the substrate at 1000°C in vacuum or in oxygen; and plasma or glow discharge techniques, for example in Freons with or without oxygen. In general, vapor phase cleaning methods use significantly less chemicals than wet immersion cleaning. In the case of wet immersion cleaning, dehydration prior to resist deposition is recommended.

In order to increase yield, micro and nanofabrication processes are highly recommended to take place inside a *clean room*, a specially designed area with environmentally controlled airborne particulates, temperature (± 0.1 °F), air pressure, humidity (from 0.5 to 5% RH), vibration, and lighting. Clean rooms are classified based on the maximum particle count per unit volume of air. The size of the particles considered in the count is traditionally of 0.5 μm or larger, and the volume of air is a cubic foot. For example, in a Class 1 clean room, the particle count needs not to exceed one 0.5 μm particle (or larger) per cubic foot. However, the acceptable particle size in IC manufacturing has been decreasing hand in hand with the ever-decreasing feature sizes. With a 64-Kilobyte dynamic random access memory (DRAM) chip, for example, one can tolerate 0.25 μm particles, but for a 4-Megabyte DRAM, one can only tolerate 0.05 μm particles.

5.4.2 Photoresist Deposition

Photoresist deposition is one of the more expensive steps in photolithography, since photoresists may cost as much as $1000 per liter and most of the resist deposition processes waste significant amounts of material. For miniaturized 3D structures, much greater resist thicknesses than those used by the IC industry are often required, and complex topographies might also call for a conformal resist coat over very high aspect ratio features. To deposit photosensitive materials for MEMS and NEMS, spin coating is the most common method for thicknesses smaller than 1 mm. Other coating techniques are also available, such as roller, curtain or extrusion coating, although they are not as efficient when depositing layers thicker than 200 μm. For very thick resist coats (>1 mm), techniques such as casting and the use of thick sheets of dry photoresists replace the use of resist spinners. For conformal coating, resist spraying, or better yet, electrodeposition (ED) of photoresist might be preferable.

Spin Coating. The most common method to deposit photoresists is spin coating. In this method, centrifugal forces causes the resist to flow to the edges, where it builds up until expelled when its surface tension is exceeded. The resulting polymer thickness, T, is a function of spin speed, solution concentration, and molecular weight (measured by intrinsic viscosity). Generally, the photoresist is dispensed onto the substrate, which is held in place by a vacuum-actuated chuck in a resist spinner (see Fig. 5.6) [145]. A rotating speed of about 500 rpm is commonly used during the dispensing step to spread the fluid over the substrate. After the dispensing step, it is common to accelerate to a higher speed to thin down the fluid near to its final desired thickness. Typical spin speeds for this step range from 1500 to 6000 rpm, depending on the properties of the fluid (mostly its viscosity) as well as the substrate. This step can take from a few seconds to several minutes. The combination of spinning speed and time will generally define the final film thickness. An empirical expression to predict the thickness of the spin coated film as a function of its molecular weight and solution concentration is given in [146]

Fig. 5.6 *Left*: A programmable spin coating system with a Si wafer being held in place by a vacuum chuck. *Right*: Manual dispensing of SU-8 photoresist

The photoresist film, after being spin coated into the substrate, must have a uniform thickness and be chemically isotropic so that its response to exposure and development is uniform. The application of too much resist results in edge covering or run-out, hillocks, and ridges, reducing manufacturing yield. Application of too little resist may leave uncovered areas. Optimization of the photoresist coating process in terms of resist dispense rate, dispense volume, spin speed, ambient temperature, venting of the resist spin station and humidity presents a growing challenge.

The need for an alternative photoresist deposition technique arises as the amount of waste material generated by spin coating becomes higher, with most of the resist solution (> 95%) thrown off the substrate during the spin casting process (the wasted resist must be disposed off as a toxic material). Inherent to this process is the formation of edge beads, which might require an additional removal process prior to subsequent processing steps. Oftentimes, the edge of the substrate exhibits resist ridges that are about 10 times higher the mean thickness on the rest of the substrate. Different edge bead removal (EBR) solutions are commercially available, such as AZ EBR Solvent or Microchem's EBR. The main obstacle to overcome when using spin coating in MEMS is caused by varying topography: deeply etched features cause a physical obstruction to the flow of photoresist, preventing complete coverage and often causing striation or resist thickness variation. For example, resist thickness variations can occur on the near and far sides of a cavity, or in cavities at different locations on the substrate. Sizes and shapes of the cavities also have influence on the resist uniformity and coating defects. For substrates with moderate topography, alternative coating techniques, like spray coating, offer better prospects.

5.4.2.1 Alternative Photoresist Deposition Methods

In this section, alternatives to spin coating are compared, closely following James Webster's treatise of the subject [147]. First, the techniques used in conformal coatings are presented. Subsequently, the techniques used to deposit resist thicknesses less than 200 μm are exposed. This sub-section ends with the details of the lamination process for dry resist films.

Spray Coating. In spray coating, the substrates proceed under a spray of photoresist solution. Compared to spin coating, spray coating does not suffer from the variation in resist thickness caused by centrifugal forces, since the droplets of resist stay where they are being deposited. Another major advantage of this method is its ability to uniformly coat over non-uniform surfaces, making the technique appropriate for MEMS processing. More importantly, sprayed coatings do not present the internal stress forces that are common to spin coated films. However, control of the deposited film thickness is not as precise as with spin and extrusion coated substrates (see below), and some waste of photoresist solution occurs as part of this processing technique. It is difficult to deposit layers of resist thicker than 20 μm with spray coating.

Electrostatic Spraying. Electrostatic spraying or electrostatic deposition (ED) is a variant of spray coating. During the atomization of the resist by air or nitrogen pressure, the formed droplets are statically charged by applying a large voltage (e.g., 20 kV). The charge causes the droplets to repel each other, maintaining the integrity of the mist of resist formed.

Electrodeposited (*electrophoretic*) (*ED*) [148]. Electrophoretic photoresist deposition is an appropriate technique for the coating of substrates with extreme topography. It uses electric fields to accelerate charged micelles, comprising resist, resist solvent, dye and photoinitiator molecules, towards the substrate to be coated. It is important to emphasize that the solution must be rather resistive for a strong enough electrophoretic field to be established. Typical coating thicknesses, highly dependent on the voltage and the temperature, are in the range of 5–10 microns, but specific resist systems can be deposited up to 35 μm. The main advantage is that it yields a pore-free deposit of the resist, even at very low thicknesses.

Other thin film coating techniques include *Silkscreen Printing, Plasma-Deposited Resist, Meniscus Coating and Dip Coating*. Alternative techniques to spin coating for thicknesses less than 200 μm include:

Roller Coating. Roller, curtain and extrusion coating are all variations of directly casting the coating solution on the substrate. Grooved rubber rolls are used to transfer the liquid resist to the substrate surface. The pitch of the grooves on the roller, the non-volatile content of the resist and the coating roller-to-substrate pressure affect the final thickness of the resist film. Excess resist flows back to a sump for recycling via an automatic viscosity controller and filter unit, thus limiting waste. In general, it is incapable of producing uniform coatings below 5 μm in thickness.

Curtain Coating. In curtain coating the substrate is moved on a conveyor through a sprayed "curtain" of resist. The liquid resist is pumped into a head from which the only exit is a thin nip on the head's underside. The resist forced through this nip forms a curtain of resist through which the substrates to be coated are passed. Typically, thickness in the 25–60 μm range can be obtained with curtain coating. Undeposited material is re-circulated back to the coating head. By carefully controlling the material viscosity, belt speed, and pump speed, reproducible thicknesses can be achieved and maintained over the substrate surface with less than 10% variation in the overall thickness.

Extrusion Coating. In extrusion coating, the extrusion head is positioned at a short, predetermined height above the substrate. A thin curtain of resist falls on the substrate, which is moving horizontally at a controlled rate. Film thicknesses from less than 1 μm to greater than 150 μm in a single coating pass have been demonstrated [147]. Disadvantages of the technique include variation in the substrate surface uniformity and the formation of edge beads along the leading edge of extrusion coated substrates, although not to the extent encountered in spin-coated films. This method requires many controls to achieve good results, and if performed well, can yield very satisfactory coatings.

It is important to mention that there is no forced drying during roller, curtain and extrusion coating other than evaporation. Therefore, the coating material has time to flow and planarize over surface features. The degree of coverage into deep features is highly dependent on the surface wettability and the solution viscosity.

Lamination. Most resists in IC and MEMS fabrication are deposited as liquids, whereas resists used in printed wiring board (PWB) manufacturing are usually rolls of dry film resists that are laminated onto the substrate instead of being spin coated on it. Dry film resist formulations are sandwiched between a polyolefin release sheet and a polyester base, and rolled up onto a support core. These protective covers shield the film from environmental oxygen and facilitate its handling. The dry film resist layers are available in thicknesses ranging from 25 up to 100 μm. Resist thicknesses of 1–1.5 millimeters are common for imaging purposes, and thicker resists (1.5–2.0 mm) are used for plating rather than etch resists. Dry film resists offer advantages such as excellent adhesion on most substrates, no liquid handling since there is no solvent, high processing speeds, excellent thickness uniformity over a whole substrate (even in substrates with holes), facile handling, no formation of edge beads, low exposure energy, low cost, short processing time and near vertical sidewalls. Conformation of the resist to the substrate is achieved by heating under pressure in a hot-roll or cut-sheet laminator. The heat and pressure of the laminating rollers causes the dry film to soften and adapt to surface topologies. The resist is then exposed to a UV light source for patterning. Modern dry film resists are developed in a simple sodium carbonate solution (1–2%) after removal of the top cover layer. The biggest disadvantage of dry resist is its relatively low resolution compared to liquid resists. Two major reasons for this poorer resolution are the thicker resist coating and the fact that the mask is positioned on top of a thick protective cover film. By removing the top cover sheet from the photoresist prior to exposure, higher resolutions are possible. There are a variety of dry film photoresists widely used and commercially available. Examples include Riston®, Ordyl BF 410, Etertec® 5600, DF 4615 and DFR-15. They are all used in the manufacture of circuit boards, can be made quite thick and are all candidates for broad use in MEMS as well. The potential benefits of using dry resist films as permanent components in the mass production of biosensors and microfluidics were recognized and described early on, for example, by Madou et al. [149]. These authors suggest that continuous, web-based manufacturing may finally make ubiquitous, disposable miniaturized devices such as biosensors and microfluidics possible. Dry resist film materials are less expensive than Si and form a convenient substrate. Furthermore, they are available in rolls so that large sheets can be processed. A continuous lithographic process, including exposure and development, taking place between a dry resist supply roll and a pick-up reel has been envisioned by these authors.

5.4.2.2 Resists

In order to understand the photolithographic process better it is necessary to study in detail its basic element: the photoresist. The principal components of a photoresist are the polymer (base resin), a sensitizer, and a casting solvent. The polymer changes its structure when is exposed to electromagnetic radiation; the solvent allows for spin application and the formation of thin layers over the substrate; and sensitizers control the chemical reactions in the polymeric phase. Resists without sensitizers are single-component systems, whereas sensitizer-based resists are two-component systems. Solvents and other potential additives do not directly relate to the photoactivity of the resist. Photoresists must meet several rigorous requirements: good adhesion, high sensitivity, high contrast, good etching resistance (wet or dry etching), good resolution, easy processing, high purity, long shelf life, minimal solvent use, low cost, and a high glass transition temperature, T_g. Most resins used as base for photoresists, such as novolacs, are amorphous polymers that exhibit viscous flow with considerable molecular motion of the polymer chain segments at temperatures above the glass transition. At temperatures below T_g, the motion of the segments is halted, and the polymer behaves as a glass rather than a rubber. If the T_g of a polymer is at or below room temperature, the polymer is considered a rubber; if it lies above room temperature, it is considered to be a glass. For the purpose of deriving glass-like carbon from photopatterned polymers it is of extreme importance to guarantee that the heating rate during pyrolysis is slower than the thermal degradation rate of the resin. In other words, the temperature in the furnace must always be lower than the T_g of the resin and the different compositions it goes through before becoming carbon. If this principle is not followed, the photopatterned polymer melts and flows, resulting in a shapeless carbon piece. In general, polymers that crystallize are not useful as resists because the formation of crystalline segments prevents the formation of uniform high-resolution isotropic films [146].

If the photoresist is of the type called *positive* (also *positive tone*), the photochemical reaction during exposure of a resist weakens the polymer by rupture or scission of the main and side polymer chains, and the exposed resist becomes more soluble in developing solutions. If the photoresist is of the type called *negative* (also *negative tone*), the photochemical reaction strengthens the polymer, by random cross-linkage of main chains or pendant side chains, thus becoming less soluble. Fig. 5.7 illustrates chain scission (positive resists) and cross-linking (negative resists).

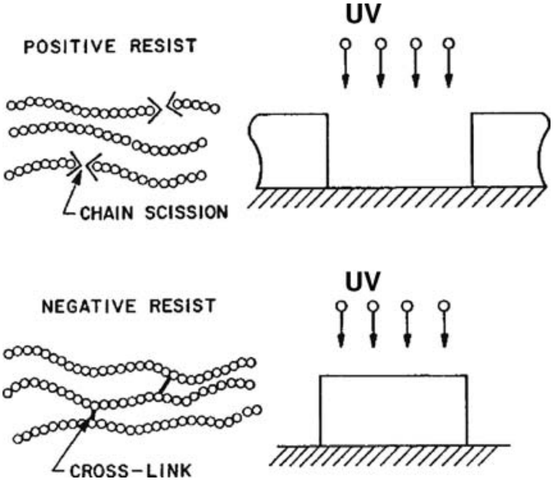

Fig. 5.7 Polymer chain scission (positive resists) and cross-linking (negative resists)

Positive Resists. Two well-known families of positive photoresists are the single component poly(methylmethacrylate) (PMMA)[3] resists and the two-component DNQ resists comprised of a photoactive component (PAC) such as diazonaphtoquinone ester (DNQ) (20–50 wt%) and a phenolic novolac resin.

PMMA becomes soluble through chain scission under Deep UV (DUV) illumination (150 nm < λ < 300 nm). Although the resolution of PMMA is very good, its

---

[3] Poly(methyl methacrylate) (PMMA) or poly(methyl 2-methylpropenoate) is the synthetic polymer of methyl methacrylate. This thermoplastic and transparent plastic is sold by the trade names Plexiglas, Limacryl, R-Cast, Perspex, Plazcryl, Acrylex, Acrylite, Acrylplast, Altuglas, Polycast and Lucite and is commonly called acrylic glass or simply acrylic.

plasma etch tolerance is very low. Besides traditional photolithography, PMMA is also used in electron beam, ion beam, and X-ray lithography.

The diazonapthoquinone (DQN) resist system is a "workhorse," near-UV (300 nm $< \lambda <$ 400 nm), two-component positive resists, which photochemically transforms into a polar, base-soluble product [150]. The hydrophilic novolac resin (N) is in itself alkali soluble because of the OH groups. Diazonaphthaquinone (DQ) is a hydrophobic and non-ionizable compound and when phenolic resins are impregnated with DQ, they become hydrophobic and are rendered insoluble. The addition of 20–50% in weight of DQ forms a complex with the phenol groups of the novolac resin and reduces the solubility rate of the unexposed resist to less than 1–2 $\text{nm}\cdot\text{s}^{-1}$. During exposure, DNQ undergoes photolysis, which destroys the inhibitory effect of DQ on film dissolution. The photolysis causes the DNQ to undergo a reaction forming a base-soluble carboxylic acid that can be rapidly developed in aqueous solution of hydroxide ions (e.g. 1% NaOH). In contrast with cross-linked resists, the film solubility is controlled by chemical and polarity differences rather than molecular size. The novolac resin matrix itself is a condensation product of a cresol isomer (para-cresol) and formaldehyde consisting of hydrocarbon rings with two methyl groups and one OH group attached. Phenolic resins are readily cross-linked by thermal activation into rigid forms (Bakelite was the first thermosetting plastic). A novolac resin absorbs light below 300 nm, and the DNQ addition adds an absorption region around 400 nm. The 365, 405, and 435 nm mercury lines can all be used for exposure of DNQ. The intense absorption of aromatic molecules prevents the use of this resist at exposing wavelengths less than about 300 nm; at those shorter wavelengths, linear acrylate and methacrylate copolymers have the advantage. Positive attributes of novolac-based resist are that the unexposed areas are essentially unchanged by the presence of the developer. Thus, line width and shape of a pattern is precisely retained. Most positive resists are soluble in strongly alkaline solutions and develop in mildly alkaline ones.

Negative Resists. The first negative photoresists were based on free-radical-initiated photo-cross-linking processes of main or pendant polymer side chains, rendering the exposed parts insoluble. They were the very first types of resists used to pattern semiconductor devices and still comprise the largest segment of the overall photoresist industry, being widely used to define circuitry in printed wiring boards (PWBs) [151]. A negative photoresist becomes insoluble in organic (more traditional negative resists) or water-based developers (newer negative resist systems) upon exposure to UV radiation. The insoluble layer forms a "negative" pattern that is used as a stencil (usually temporarily) to delineate many levels of circuitry in semiconductors, microelectromechanical systems (MEMS), and printed wiring boards (PWBs). In latest years, features fabricated from negative resist also act as structural elements. The insolubilization of radiated negative resists can be achieved in one of two ways: the negative resist material increases in molecular weight through UV exposure (traditional negative resists), or it is photochemically transformed to form new insoluble products (newer negative resist products).

A disadvantage of negative resists is that the resolution is limited by film thickness. The cross-linking process starts topside, where the light hits the resist first.

Consequently, overexposure is needed to render the resist insoluble at the substrate interface. The greater the desired resist thickness, the greater the overdose needed for complete polymerization and the larger the scattered radiation. Scattered radiation at the resist/substrate interface in turn reduces the obtainable resolution. To improve the resolution of a negative resist, thinner resist layers can be used; however, when using thin layers of negative resist, pinholes become problematic. Negative photoresists, in general, adhere very well to the substrate, and a vast amount of compositions are available. They are highly resistant to acid and alkaline aqueous solutions as well as to oxidizing agents. As a consequence, a given thickness of negative resist is more chemically resistant than a corresponding thickness of positive resist. This chemical resistance ensures better retention of resist features even during a long, aggressive wet or dry etch. Negative resists are also more sensitive than positive resists but exhibit a lower contrast. A good and very practical example of negative resists is that of SU-8.

SU-8 is an acid-catalyzed negative photoresist, made by dissolving EPON®-SU-8 resin (a registered trademark of Shell Chemical Company) in an organic solvent such as cyclopentanone or GBL (gamma-butyloractone) and adding a photoinitiator. The viscosity and hence the range of thicknesses accessible, is determined by the ratio of solvent to resin. The EPON resist is a multifunctional, highly-branched epoxy derivative that consists of bisphenol-A novolac glycidyl ether. On average, a single molecule contains eight epoxy groups which explain the eight in the name SU-8. The material has become a major workhorse in miniaturization science. In a chemically amplified resist like SU-8, one photon produces a photoproduct that in turn causes hundreds of reactions to change the solubility of the film. Since each photolytic reaction results in a "amplification" via catalysis, this concept is dubbed "chemical amplification" [152].

Scientists at IBM discovered that certain photo-initiators, such as onium salts, polymerize low-cost epoxy resins such as EPON®-SU-8. Compositions of SU-8 photoresist were patented by IBM as far back as 1989 [153] and 1992 [154]. Original compositions were intended for printed circuit board and e-beam lithograpy. SU-8 photoresists became commercially available in 1996. Because of its aromatic functionality and highly cross-linked matrix, the SU-8 resist is thermally stable and chemically very inert. After a hard bake, it withstands nitric acid, acetone, and even NaOH at 90°C and it is more resistant to prolonged plasma etching and better suited as a mold for electroplating than Poly(methyl methacrylate) (PMMA) [155]. The low molecular weight [~ 7000 ± (1000) Da] and multifunctional nature of the epoxy gives it the high cross-linking propensity, which also reduces the solvent-induced swelling typically associated with negative resists. As a result, very fine feature resolution, unprecedented for negative resists, has been obtained and epoxy-based formulations are now used in high-resolution semiconductor devices. Low molecular weight characteristics also translate into high contrast and high solubility. Because of its high solubility very concentrated resist casting formulations can be prepared. The increased concentration benefits thick film deposition (up to 500 μm in one coat) and planarization of extreme topographies. The high epoxy content promotes strong SU-8 adhesion to many types of substrates and makes the material highly sensitive to UV exposure. On the negative side, strong adhesion makes stripping of the exposed SU-8 material currently one of the most problematic aspects in those applications where the resist must be removed such as in the IC industry. Stripping of SU-8 may be carried out with hot NMP (1-methyl-2-pyrrolidon), plasma or laser ablation. There are other issues to be resolved with this resist; for example, thermal mismatch of SU-8 on a Si substrate (the thermal expansion coefficient for Si is 2.361 10^{-6}/K versus 21–52 10^{-6}/K for SU-8) produces stress and may cause film cracking. Moreover, the absorption spectrum of SU-8 shows much higher absorption coefficients at shorter wavelengths. As a result lithography using a broadband light source tends to result in over-exposure at the surface of the resist layer and under-exposure at the bottom. The resulting developed photoresist tends to have a negative slope, which is not good for mold applications: the mold sidewall should have a positive or at least a vertical slope for easy release of the molded part from the mold. The exaggerated negative slope at the top of the resist structure surface is often called *T-topping* (See Fig. 5.8). UV light shorter than 350 nm is strongly absorbed near the surface creating locally more acid that diffuses sideways along the top surface. Selective filtration of the light source is often used to eliminate these undesirable shorter wavelengths (below 350 nm) and thus obtain better lithography results. For example, Reznikova et al. used a 100 μm thick SU-8 resist layer to filter exposure radiation at 334 nm [156] and Lee et al. reported using a Hoya UV-34 filter to eliminate the T-top (over-exposed top part) [157]. Nearly vertical sidewalls can be achieved using a Hoya UV-34 filter. Aspect ratios up to ~25 for lines and trenches have been demonstrated in SU-8-based contact lithography. When patterned at 365 nm, the wavelength at which the photoresist is the most sensitive, total absorption of the incident light in SU-8 is reached at a depth of 2 mm. In principle, resist layers up to 2 mm thick can be structured [158]. Yang and Wang recently confirmed this astounding potential experimentally [159]. This group at Louisiana State University (LSU), using both wavelength optimization by patterning using a filtered i-line (365 nm) and air gap compensation (with glycerin or a Cargille refractive index matching fluid), demonstrated aspect ratios above 190

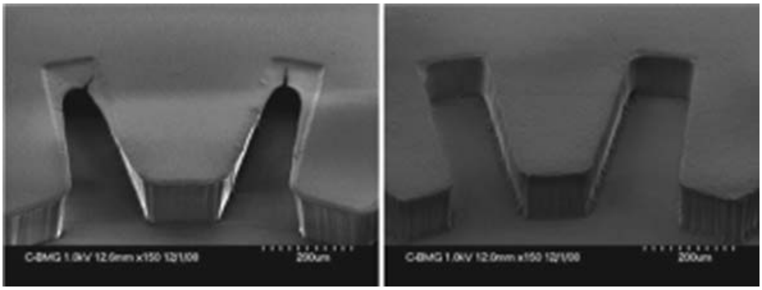

Fig. 5.8 The effect of T-topping. *Left*: Gear pattern showing T-topping. *Right*: Same gear pattern but now T-topping is minimized by the use of an in-house fabricated filter (A 50 μm layer of SU-8 on quartz)

(for a feature with a 6 μm thickness and a height of 1150 μm) and structures as high as 2 mm. Several publications exist on SU-8, a recent review is [160].

A comparison of negative and positive photoresist features is presented in Table 5.1. This table is not exhaustive and is meant only as a practical guide for selection of a resist tone. The choice of whether to use a negative or a positive resist system depends upon the needs of the specific application, such as resolution, ease

Table 5.1 Comparison of traditional negative and positive photoresists

	Resist type	
Characteristic	Positive resist	Negative resist
Adhesion to Si	Fair (priming required)	Excellent (priming not required)
Available compositions	Many	Vast
Baking	In air (+)	In Nitrogen (−) or Air (+)
Contrast γ	Higher, e.g., 2.2	Lower, e.g., 1.5
Cost	More expensive	Less expensive
Developer	Temperature sensitive (−) and aqueous based (Ecologically sound)	Temperature insensitive (+) and organic solvent (−), aqueous based has been introduced.
Developer process window	Small	Wide, relatively insensitive to overdeveloping
Influence of oxygen	No (+)	Yes (−). Minimized in the case of SU-8.
Lift-off	Yes, usually with multiple layer resist (MLR)	Yes, even in single layer resist (SLR)
Mask type	Dark-field: lower-defects	Clear-field: higher-defects
Opaque dirt on clear portion of mask	Not very sensitive to it	Causes printing of pinholes
Photospeed	Slower	Faster
Pinhole count	Higher	Lower
Pinholes in mask	Prints mask pinholes	Not so sensitive to mask pinholes
Plasma etch resistance	Not very good	Very good
Proximity effect	Prints isolated holes or trenches better	Prints isolated lines better
Residue after development	Mostly at < 1 μm and high aspect ratio	Often a problem
Resolution	High	Low (>1 μm)
Sensitizer quantum yield ϕ	0.2–0.3	0.5–1
Step coverage	Better	Lower, can be higher with diluted solutions such as SU-8 2000.5 or 2002.
Strippers of resist over		
Oxide steps	Acid	Acid
Metal steps	Simple solvents	Chlorinated solvent compounds
Swelling in developer	No	Yes
Thermal stability	Good	Fair, good with SU-8.
Wet chemical resistance	Fair	Excellent

of processing, speed, and cost. If the objective is to obtain high-aspect ratios, the use of negative resist is preferred.

5.4.3 Soft Baking or Prebaking

After resist coating, the resist still contains up to 15% solvent and may contain built-in stresses. The photoresist is therefore soft baked (also named pre-exposure baked or prebaked) for a given time in an oven or hotplate at temperatures ranging from 70 to 100°C to remove solvents and stress and to promote adhesion of the resist layer to the substrate. This is a critical step in that failure to sufficiently remove the solvent will affect the resist profile. Excessive baking destroys the photoactive compound and reduces sensitivity. Thick resists may benefit from a longer bake time. The resist thickness, for both negative and positive resists, is typically reduced by 10–25% during soft baking. Hot plating the resist is faster, more controllable, and does not trap solvent like convection oven baking does. In convection ovens the solvent at the surface of the resist is evaporated first, and this can cause an impermeable resist skin, trapping the remaining solvent inside. Commercially, microwave heating or IR lamps are also used in production lines. The optimization of the prebaking step may substantially increase device yield.

5.4.4 Exposure

After soft baking, the resist-coated substrates are transferred to an illumination or exposure system where they are aligned with the features on a mask. For any lithographic technique to be of value, it must provide an alignment technique capable of a precise superposing of mask and substrate that is a small fraction of the minimum feature size of the devices under construction. In the simplest case, an exposure system consists of a UV lamp illuminating the resist-coated substrate through a mask without any lenses between the two. The purpose of the illumination systems is to deliver light with the proper intensity, directionality, spectral characteristics, and uniformity across the wafer, allowing a nearly perfect transfer or printing of the mask image onto the resist in the form of a latent image. The incident light intensity (in W/cm^2) multiplied by the exposure time (in seconds) gives the incident energy (J/cm^2) or dose, D, across the surface of the resist film. Radiation induces a chemical reaction in the exposed areas of the photoresist, altering the solubility of the resist in a solvent either directly or indirectly via a sensitizer. The smaller the dose needed to “write” or “print” the mask features onto the resist layer with good resolution, the better the lithographic sensitivity of the resist.

The absolute size of a minimum feature in an IC or a miniature device, whether it involves a line-width, spacing, or contact dimension, is called the *critical dimension* (CD). The overall resolution of a process describes the consistent ability to print a minimum size image, a critical dimension, under conditions of reasonable manufacturing variation [161]. Many aspects of the process, including hardware, materials, and processing considerations can limit the resolution of lithography. Hardware limitations include diffraction of light or scattering of charged particles (in the case of charged-particle lithography or hard X-rays), lens aberrations and mechanical stability of the system. The resist material properties that impact resolution include contrast, swelling behavior, thermal flow, and chemical etch resistance. The most important process-related resist variables include swelling (during development) and stability (during etching and baking steps).

In photolithography, wavelengths of the light source used for exposure of the resist-coated wafer range from the very short wavelengths of extreme ultraviolet (EUV) (10–14 nm) to deep ultraviolet (DUV) (150–300 nm) to near ultraviolet (UV) (350–500 nm). In near UV, one typically uses the g-line (435 nm) or i-line (365 nm) of a mercury lamp. The brightness of shorter-wavelength sources is severely reduced compared to that of longer-wavelength sources, and the addition of lenses further reduces the efficiency of the exposure system. As a consequence, with shorter wavelengths, higher resist sensitivity is required, and newer DUV sources that produce a higher flux of DUV radiation must be used. In general, the smallest feature that can be printed using projection lithography is roughly equal to the wavelength of the exposure source. The current generation of lithography is using 193 nm light [150] from ArF lasers. Step and scan printing Extreme Ultra-Violet (EUV) systems are expected to come on-line by the end of this decade. In order to stretch the lower limits of photolithography, sophisticated Resolution-Enhancing Techniques (RETs) are employed. RET methods enable one to go quite a bit beyond the conventional Rayleigh diffraction limit and may be used to produce features of 160 nm and below. These methods are classified depending on the element or part of the process they enhance: resist, mask or exposure procedure. RETs improving the resist include chemically amplified resists and anti-reflection coatings – thin film interference effects. Those enhancing the mask are Phase Shifting Masks (PSM) and Optical Proximity Correction (OPC). Enhancements to the exposure procedure include Off-Axis Illumination (OAI), Kohler Illumination and Immersion Lithography. RETs are beyond the scope of this work and the reader is referred to [144].

5.4.4.1 Masks and Grayscale Lithography

Standard Photolithography Masks. The stencil used to repeatedly generate a desired pattern on resist-coated wafers is called a mask. In typical use, a photomask – a nearly optically flat glass (transparent to near ultraviolet [UV]) or quartz plate (transparent to deep UV) with an absorber pattern metal layer (e.g., an 800 Å thick chromium layer) – is placed above the photoresist-coated surface, and the mask/substrate system is exposed to UV radiation. The absorber pattern on the mask is generated by e-beam lithography, a technique that yields higher resolution than photolithography (see below). Like resists, masks can be positive or negative. A positive or dark field mask is a mask on which the pattern is clear with the background dark. A negative or clear field mask is a mask on which the pattern is dark with the background clear. A light field or dark field image, known as mask polarity, is then transferred to the surface. This procedure results in a 1:1 image of the entire mask onto the substrate.

Different types of exposure masks are shown in Fig. 5.9. Masks making direct physical contact (also referred to as hard contact) with the substrate, are called contact masks. Unfortunately, these masks degrade faster due to wear than noncontact, proximity masks (also referred to as soft contact masks), which are slightly raised, say 10–20 μm, above the substrate. However, diffraction effects are minimized with the use of hard contact masks. Hard and soft contact masks are still in use in R&D, in mask making itself, and for prototyping (see Fig. 5.10). Contact mask and proximity mask printing are collectively known as shadow printing. A more reliable method of masking is projection printing where, rather than placing a mask in direct contact with (or in proximity of) a substrate, the photomask is imaged by a high-resolution lens system onto the resist-coated substrate. In projection printing, the only limit to the mask lifetime results from operator handling. The imaging lens can reduce the mask pattern by 1:5 or 1:10, making mask fabrication less challenging. Diffraction can be minimized by the use of highly collimated light sources and/or collimator lenses. Projection printing is the masking method employed in Very Large Scale Integration (VLSI)-based devices such as ICs.

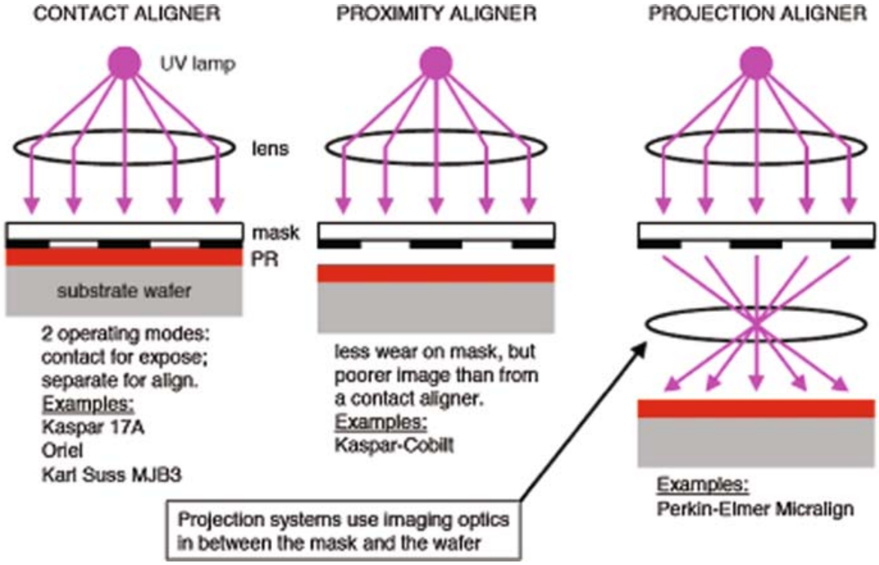

Fig. 5.9 Contact printing, proximity printing and projection printing

In miniaturization science, one often is looking for low-cost and fast-turnaround methods to fabricate masks. This may involve in-house fabricated masks by manually drawing patterns on cut-and-peel masking films and photo reducing them. Alternatively, it may involve direct writing on a photoresist-coated plate with a laser-plotter (~ 2 μm resolution) [162]. Simpler yet, using a drawing program such as Canvas® (ACD Systems, Ltd.), Freehand®, Illustrator® (Adobe Systems, Inc.), or

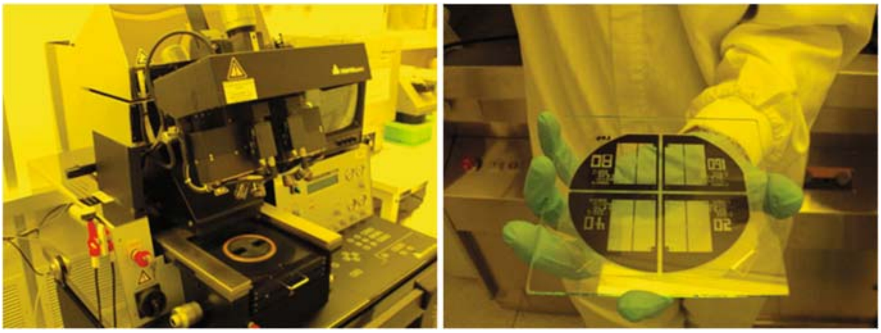

Fig. 5.10 *Left*: A SUSS MicroTec MA/BA6 mask aligner featuring bottom and top-side-alignment microscopes (Integrated Nanosystems Research Facility, UC Irvine). *Right*: A transparency mask taped to a low UV absorption glass holder

L-Edit® (Tanner Research, Inc.) a mask design can be created on a computer and saved as a Postscript® or Gerber® file to be printed with a high-resolution printer on a transparency [163]. The transparency with the printed image may then be clamped between a pre-sensitized chrome-covered mask plate and a blank plate to make a traditional photomask from it. After exposure and development, the exposed plate is put in a chrome etch for a few minutes to generate the desired metal pattern, and the remaining resist is stripped off. Simpler yet, the printed transparency may be attached to a quartz plate to be used as mask directly (See Fig. 5.10). Resolution with these methods is currently in the order of few micrometers and is highly dependent on the photo-plotter used to print the transparency. Even when these masks are significantly less expensive and have a fast-turnaround time, the quality of the exposed patterns, i.e. wall roughness, is obviously less than that obtained with photomasks patterned with e-beam lithography (where resolution can be less than 50 nm) (see Fig. 5.11).

Grayscale Lithography. Photolithography, as described so far, constitutes a binary image transfer process – the developed pattern consists of regions with resist (1) and regions without resist (0). In contrast, in grayscale lithography, the partial exposure of a photoresist renders it soluble to a developer in proportion to the local exposure dose and as a consequence, after development, the resist exhibits a surface relief. Grayscale lithography has a great potential use in miniaturization science as it allows for the mass production of micromachines with varying topography. The possibility of creating profiled micro 3D structures offers tremendous additional flexibility in the design of microelectronic, optoelectronic and micromechanical components [164]. A key part in the development of a grayscale process is the characterization of the resist thickness as a function of the optical density in the mask for a given lithographic process. It is also desirable to use photoresists that exhibit a low contrast in order to achieve a wide process window. Ideally, the resist response can be linearized to the optical density within the mask. Grayscale lithography can be achieved without the use of physical masks (software masks) or by employing Gray-tone masks (GTMs).

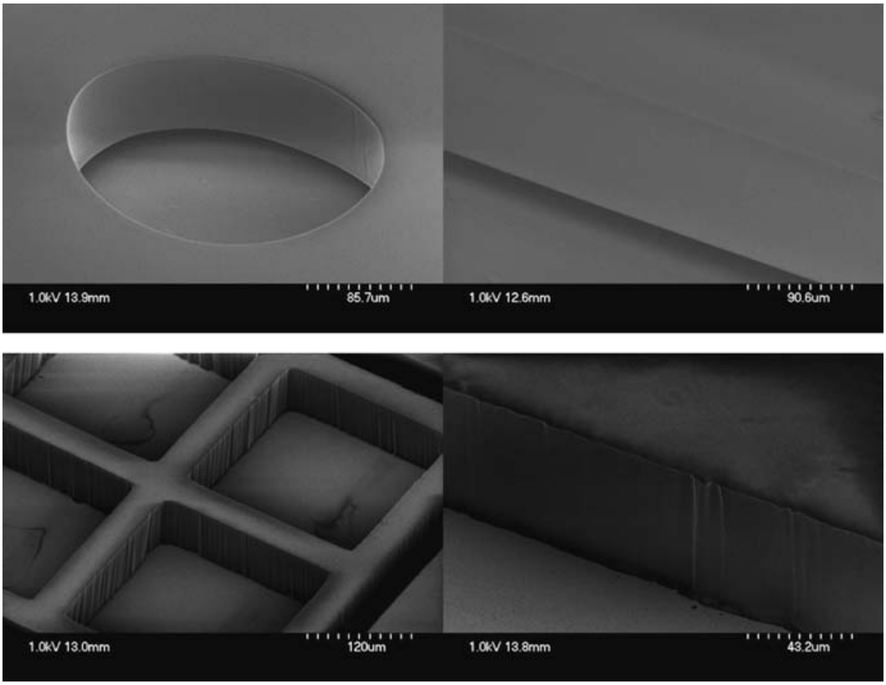

Fig. 5.11 The quality of a pattern is obviously far superior when using photomasks patterned with e-beam lithography (*top*) than when using transparency masks printed with a commercial photo-plotter (*bottom*)

Possible methods for making GTMs, or variable transmission masks, include magnetron sputtering of amorphous carbon (a-C) onto a quartz substrate. Essentially any transmittance (T) desired in the $0 < T < 100\%$ range can be achieved by controlling the film thickness (t) in the $200 > t > 0$ nm range with subnanometer precision [165]. Perhaps more elegantly, gray levels may be created by the density of dots that will appear as transparent holes in a chromium mask. These dots are small enough not to be transferred onto the wafer because they are below the resolution limit of the exposure tool. Another attractive way to fabricate a GTM is with High Energy Beam Sensitive (HEBS) glass. HEBS-glass turns dark upon exposure to an electron beam; the higher the electron dosage, the darker the glass turns. In HEBS-glass, a top layer, a couple of microns thick, contains silver ions in the form of silver-alkali-halide $(AgX)_m\ (MX)_n$ complex nanocrystallites that are about 10 nm or less in size, and are dispersed within cavities of the glass SiO_4 tetrahedron network. Chemical reduction of the silver ions produces opaque specks of silver atoms upon exposure to a high-energy electron beam (> 10 kV) [164].

Due to problems caused by the use of masks, such as expense and time consumed in fabricating them, contamination introduced by them, their disposal, and the difficulties in their alignment, research into Maskless Optical Projection Lithography

(MOPL) is growing rapidly and broadly. One approach to make multi-level photoresist patterns directly, without a physical mask but instead with a *software mask*, is by variable-dose e-beam writing, in which the electron dosage (the current multiplied by the dwell time) is varied across the resist surface [166]. A laser writer can produce the same result but at a lower resolution. However, variable-dose e-beam and laser writing are serial, slow and costly thus making gray-tone masks (GTMs) a desirable alternative, especially if high throughput production is required. Another MOPL or *software mask* approach already on the market (by Intelligent Micro Patterning LLC), is based on the Digital Micromirror Device (DMD) chip from Texas Instruments Inc. (TI), and relies on the same spatial and temporal light modulation technology used in DLP (Digital Light Processing) projectors and HDTVs (high definition televisions). Enormous simplification of lithography hardware is feasible by using the movable mirror arrays in a DMD chip to project images on the photoresist. This technique is capable of fabricating micromachined elements with any surface topography, and can, just like e-beam lithography or laser writing, be used for implementing maskless binary and grayscale lithography. The maximum resolution of DMD-based maskless photolithography (currently about 1 μm) is less than with e-beam lithography (less than 50 nm) or laser writers (<1.0 μm), but it is a parallel technique and for many applications, i.e. in microfluidics, the lower resolution might not be an obstacle. The unique capability of representing a gray scale is probably the most essential merit of this type of maskless lithography. When a mirror is switched on more frequently than off, it reflects a light gray pixel; a mirror that is switched off more frequently reflects a darker gray pixel. In this way, the mirrors in a DMD system can reflect pixels in up to 1,024 shades of gray to convert the video or graphic signal entering the DMD chip into a highly detailed grayscale image. Examples of grayscale features obtained with a SF-100 are shown in Fig. 5.12.

5.4.5 Post Exposure Treatment

A post-exposure treatment of the exposed photoresist is often desired because the reactions initiated during exposure might not have run to completion. To halt the reactions or to induce new ones, several post-exposure treatments are common: post-exposure baking (PEB), flood exposure with other types of radiation, treatment with a reactive gas, and vacuum treatment. Post-exposure baking (sometimes in vacuum) and treatment with reactive gas are used in image reversal and dry resist development. In the case of a chemically amplified resist, such as SU-8, the post-exposure bake is most critical. Although reactions induced by the catalyst that forms during exposure take place at room temperature, their rate is greatly increased by baking at 60–100°C. The precise control of PEB times and temperatures critically determines the subsequent development and the quality of the final features. Extended PEB times will introduce significant amounts of stress in the polymer that will most likely cause structure bending and peeling from the substrate; especially in

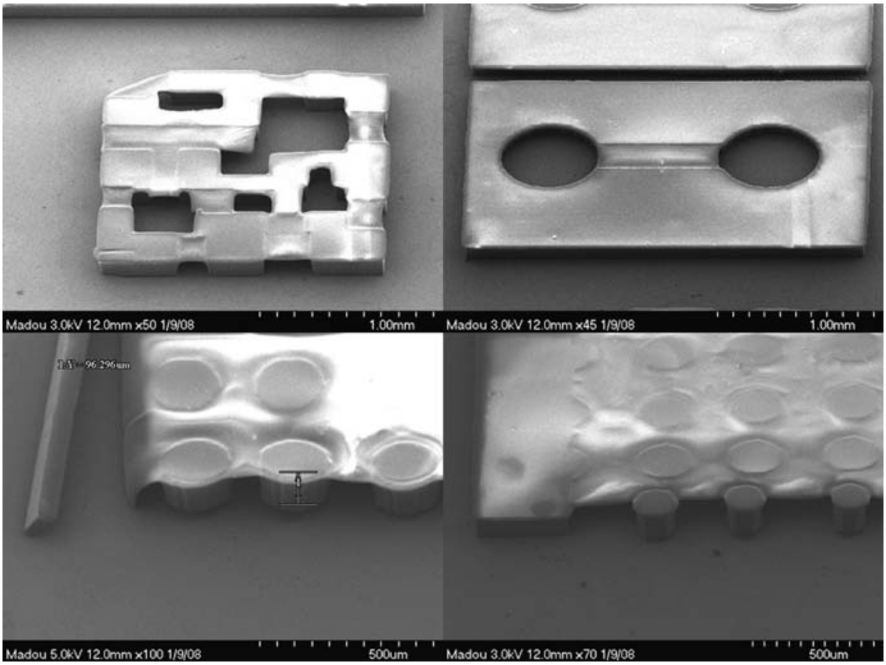

Fig. 5.12 Examples of grayscale lithography obtained with the SF-100 (Intelligent Micro Patterning, LLC) using SU-8 as resist. These features were fabricated by one of the authors in the Indian Institute of Technology in Kanpur, India

extended, large surface area features. Reduced times will yield structures that are not completely cross-linked and can be attacked by the developer. This causes extremely high surface roughness or even complete dissolution. An optimal PEB improves adhesion, reduces scumming (resist left behind after development), increases contrast and resist profile (higher edge-wall angle) and reduces the effects of standing waves in a regular resist.

5.4.6 Development

Development is the dissolution of un-polymerized resist that transforms the latent resist image, formed during exposure, into a relief image that will serve as a mask for further subtractive and additive steps, as a permanent structural element, or as a precursor for carbonization as in the case of C-MEMS. During the development of an exposed resist, selective dissolving takes place. Two main technologies are available for development: wet development, which is widely used in circuit and miniaturization manufacture in general, and dry development, which is starting to replace wet development for some of the ultimate line-width resolution applications. Wet development by solvents can be based on at least three different types of exposure-induced changes: variation in molecular weight of the polymers (by cross-linking or by chain scission), reactivity change, and polarity change [167]. Two main types of wet development setups are used: immersion and spray developers. During batch immersion developing, substrates are batch-immersed for a timed period in a developer bath and agitated at a specific temperature.

During batch spray development, fan-type sprayers direct fresh developing solution across wafer surfaces. Positive resists are typically developed in aqueous alkaline solutions, and negative resists in organic ones. Each developer has a different dilution, and some require longer development times than others. They are generally matched to a type of photoresist. Though they may be interchangeable to some extent, changing the type of developer used in a process will usually change the development time necessary to resolve the pattern.

The use of organic solvents leads to some swelling of the resist (especially for negative resists) and loss of adhesion of the resist to the substrate. Dry development overcomes these problems, as it is based either on a vapor phase process or a plasma [168]. In the latter, oxygen-reactive ion etching (O_2-RIE) is used to develop the latent image. The image formed during exposure exhibits a differential etch rate to O_2-RIE rather than differential solubility to a solvent [146]. Dry developed resists should not be confused with dry film resists, which are resists that come in film form and are laminated onto a substrate rather than spin coated. With the continued pressure by the U.S. Environmental Protection Agency (EPA) for a cleaner environment, dry development and dry etching are becoming the predominant technologies to use.

5.4.7 De-Scumming and Post-Baking

A mild oxygen plasma treatment, so-called de-scumming, removes unwanted resist left behind after development. Negative, and to a lesser degree positive, resists leave a thin polymer film at the resist/substrate interface.

Post-baking or hard baking removes residual coating solvent and developer, and anneals the film to promote interfacial adhesion of the resist that has been weakened either by developer penetration along the resist/substrate interface or by swelling of the resist (mainly for negative resists). Unfortunately, post-bake does induce some stress and resist shrinkage. Nevertheless, hard baking improves the hardness of the film and avoids solvent bursts during vacuum processing. Improved hardness increases the resistance of the resist to subsequent etching steps. Post-baking frequently occurs at higher temperatures (120°C) and for longer times than soft baking. The major limitation for heat application is excessive flow or melt, which degrades wall profile angles and enables impurities to be easily incorporated into the polymer matrix due to the plastic flow of the resist. Special care needs to be taken to prevent the post-baking temperature from exceeding the glass transition temperature, T_g, of the developed resist. However, resist reflow may be used for tailoring resist sidewalls.

5.4.8 Resist Profiles – An overview

Manipulation of resist profiles is one of the most important concerns of a lithography engineer. Depending on the final objective, one of the three resist profiles shown in Fig. 5.13 is attempted. A reentrant, undercut or a reverse resist profile (resist sidewall > 90°) is required for metal lift-off. Some authors confusingly call slopes > 90° *overcut* [168]; most, including these authors, refer to this type of resist profile as an *undercut.* Shallow resist angles (< 90°) enable continuous deposition of thin films over the resist sidewalls. A vertical (90° resist sidewall angle) slope is desirable when the resist is intended to act as a permanent structural element such as in microfludics and molding applications. Vertical walls are also usually desirable in C-MEMS applications. For more details refer to [144].

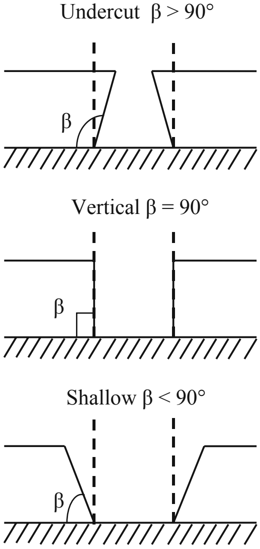

Fig. 5.13 The three important resist profiles. Top: reentrant, undercut or a reverse resist profile (resist sidewall $\beta > 90°$) is required for metal lift-off. A vertical ($\beta = 75$–$90°$ resist sidewall angle) slope is desirable for a perfect fidelity transfer of the image on the mask to the resist. Shallow resist angles ($45° < \beta < 90°$) enable continuous deposition of thin films over the resist sidewalls

5.5 Next Generation Lithography (NGL)

We now introduce the concept of Next Generation Lithography (NGL). This group of techniques are the ones regarded today as sufficiently developed to be postulated as replacements to traditional photolithography in the everlasting race to shrink feature dimensions. Techniques classified now as NGL include: extreme ultraviolet lithography (EUVL), X-ray lithography, charged particle beam lithography based on electrons and ions (such as electron and ion projection techniques) and imprint lithography [Nanoimprint lithography (NIL) and Step-and-Flash Imprint

Lithography (SFIL)]. IC and miniaturization science are taking increasingly separate paths in adopting preferred lithography strategies. For ICs, throughput and finer geometries are needed and batch processing is a prerequisite. In miniaturization science, modularity, good depth-of -focus (DOF), extension of the z-direction, that is, the height of features (skyscraper-type structures), incorporating nontraditional materials (e.g., gas-sensitive ceramic layers, polymers), and replication methods catch the spotlight and batch fabrication is not always a prerequisite. We emphasize on charged-particle-based and imprint lithographies because they represent a more affordable and readily available way to obtain nano-sized structures for Carbon NEMS or nanofluidics applications. EUVL and X-ray lithography may also be used but they are more expensive and are not readily available due to their required infrastructure. EUVL and X-ray are touted by the IC industry as strong candidates to replace DUV lithography in the quest to achieve the 32 nm node although no clear solution has been envisioned yet (International Technology Roadmap for Semiconductors). EUV is actively being promoted by the Extreme Ultraviolet Limited Liability Company (EUV LLC) which is a consortium lead by Intel Corporation with partners such as Motorola Corporation, Advanced Micro Devices Corporation, IBM, Infineon, Micron Technology and the Sandia and Lawrence Livermore National Laboratories. X-ray lithography is being championed by IBM in the US and by NTT, Toshiba, Mitsubishi and NEC in Japan [169]. Other techniques currently in the R&D stage but that could emerge as serious NGLs in the coming years include lithography based on very thin resist layers and block copolymers, zone plate array lithography (ZPAL), quantum lithography (two-photon lithography) and proximal probe based techniques such as atomic force microscopy (AFM), scanning tunneling microscopy (STM), dip-pen lithography (DPL) and near-field scanning optical microscopy (NSOM), and apertureless near-field scanning optical microscopy (ANSOM). In this section we will only explore electron beam, ion beam and nanoimprint lithography. An extensive review on the other techniques mentioned can be found in [144].

Before moving forward it is worth mentioning the LIGA (a German acronym for Lithographie, Galvanoformung, Abformung) technique as an alternative to fabricate very high aspect ratio structures using X-ray lithography. The LIGA technique was invented about 20 years ago [170]. The process, illustrated in Fig. 5.14, involves a thick layer of resist (from micrometers to centimeters), high-energy X-ray radiation, and resist development to make a resist mold. By applying galvanizing techniques, the mold is filled with a metal. The resist structure is removed, and metal products result. Alternatively, the metal part can serve as a mold itself for precision plastic injection molding. Several types of plastic molding processes have been tested, including reaction injection molding, thermoplastic injection molding, and hot embossing. The so-formed plastic part, just like the original resist structure, may also serve as a mold for fast and cheap mass production, since one does not rely on a new X-ray exposure. Of particular interest to miniaturization science is the possibility of creating three-dimensional shapes with slanted sidewalls and step-like structures. The unprecedented precision attainable with LIGA makes this technique stand out against other 3D lithography methods such as Deep UV with SU-8. LIGA

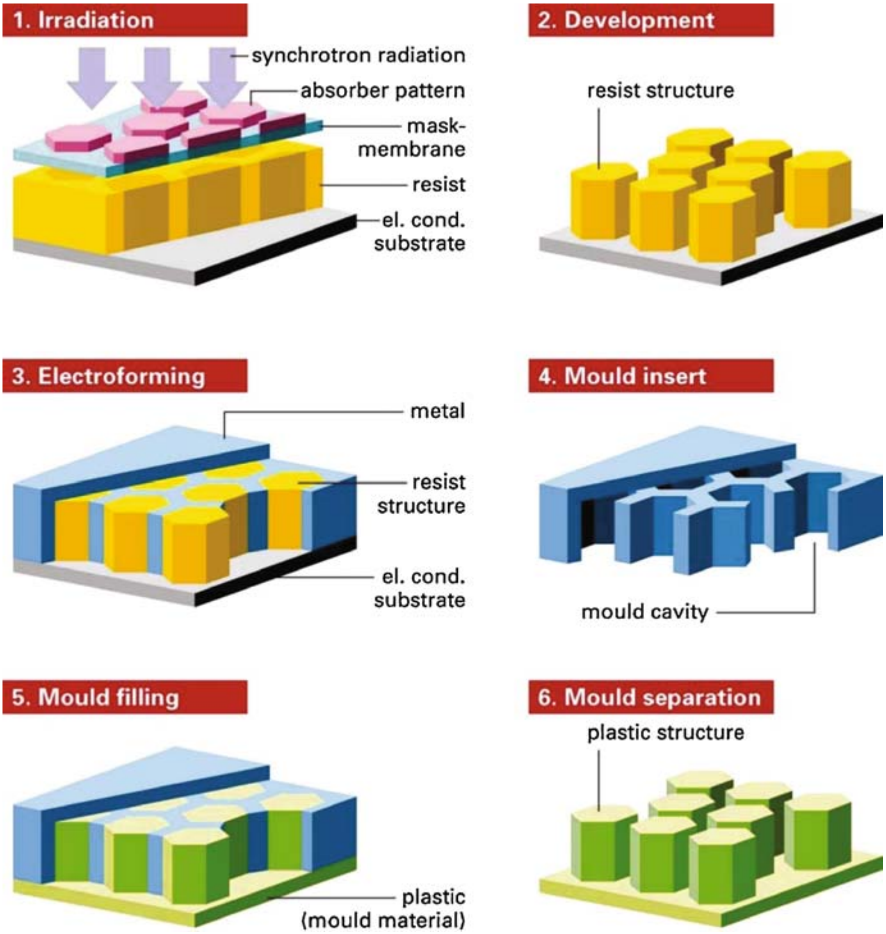

Fig. 5.14 The LIGA process

enables new building materials and a wider dynamic range of dimensions and possible shapes but its wider adoption for commercial and research applications have been halted by the need of an X-ray source (a synchrotron) in the fabrication process. We now proceed to explore charged-particle-beam and imprint lithography techniques.

5.5.1 Charged-Particle-Beam Lithography

Charged-particle-beam lithography includes both narrow beam direct-writing and flood exposure projection systems with electrons and ions. One of the major advantages of direct writing over flood exposure is its independence from a mask and thus a mask fabrication process.

In direct writing systems, the computer-stored pattern is directly converted to address the writing charged particle beam, enabling the pattern to be exposed sequentially, point by point, over the whole wafer. In other words, the mask is a *software mask*. Electron-beam (e-beam) and ion-beam (i-beam) lithographies involve high current density in narrow electron or ion beams. The smaller the beam sizes, the better the resolution, but more time is spent writing the pattern. This sequential (scanning) type system exposes one pattern element or pixel at a time. Within that area, the charged-particle beam delivers maximum current (i), which is limited primarily by the source brightness and column design. The experimental setup imposes a limit on the speed at which the writing beam can be moved and modulated, resulting in a "flash" time in seconds (t). The maximum dose D_{max} (in coulombs per cm^2) deliverable by a particular beam is given by the product of the current and time divided by the pixel area (in cm^2). It will then be necessary to work with resists that react sufficiently fast at D_{max} to produce a lithographically-useful, three-dimensional image (latent or direct image). The continued development of better charged-particle-beam sources keeps widening the possibilities for nanoscale engineering through direct write lithography, etching, depositing, analyzing, and modifying a wide range of materials, well beyond the capability of classical photolithography. Table 5.2 lists some ion-beam and electron-beam applications.

Table 5.2 Electron- and Ion-Beam Applications

Electron-Beam Applications	Ion-Beam Applications
Nanoscale lithography	Micromachining and ion milling
Low-voltage scanning electron microscopy	Microdeposition of metals
Critical dimension measurements	Maskless ion implantation
Electron-beam-induced metal deposition	Microstructure failure analysis
Reflection high-energy electron diffraction (RHEED)	Secondary ion mass spectroscopy
Scanning auger microscopy	–

Flood exposure of a mask in a projection system (that is, parallel exposure of all pattern elements at the same time, as done in Deep UV) is possible with ions and electrons as well. Technologies such as SCattering with Angular Limitation Projection Electron beam Lithography (SCALPEL) and Ion Projection Lithography (IPL) have the potential of making electron-beam and ion-beam high throughput. Exposure masks are fabricated from heavy metals on semi-transparent organic or inorganic membranes. The high cost of mask fabrication and the instability of the mask due to heating have postponed commercial acceptance of these high-energy exposure systems. Moreover, with ion and electron beams, flood exposure is limited to chip-size fields due to difficulties in obtaining broad, collimated, charged-particle beams. The most prevalent use of charged-particle beams remains the narrow beam scanning mode. Because of this reason we emphasize on Direct write Electron-Beam (e-beam) and Focused Ion Beam (FIB) lithography. Details on SCALPEL and IPL can be found elsewhere [144].

5.5.1.1 Direct Write Electron-Beam Lithography

Direct write electron-beam lithography or simply e-beam is a high-resolution patterning technique in which high-energy electrons (10–100 keV) are focused into a narrow beam and are used to expose electron-sensitive resists. There are two basic ways to scan an electron beam. In raster scanning, the patterns are written by an electron beam that moves through a regular pattern. The beam scans sequentially over the entire area and is blanked off where no exposure is required. On the contrary, in vector scanning, the electron beam is directed only to the requested pattern features and hops from features to features. Time is therefore saved in a vector scan system. The direct write technique was first developed in the 1960s using existing SEM technology. As a research solution, several groups modify their standard scanning electron microscopes to create customized electron-beam writing systems. Rosolen, for example, modified a Hitachi S2500 with a purpose built pattern generator and alignment system. The instrument does not require alignment marks on the sample and is able to compensate for positional errors caused by the sample stage and mask tolerances [171]. The e-beam lithography method, like X-ray lithography, does not limit the obtainable feature resolution by diffraction, because the quantum mechanical wavelengths of high-energy electrons are exceedingly small. Advantages and disadvantages of e-beam lithography are shown in Table 5.3. Because of such, the use of electron-beam lithography has been limited to mask making and direct writing on wafers for specialized applications. Usually,

Table 5.3 Advantages and Disadvantages of e-beam lithography

Advantages	Disadvantages
Precise control of the energy and dose delivered to a resist-coated substrate	Proximity effects. Electrons scatter quickly in solids, limiting practical resolution to dimensions greater than 10 nm
Deflection and modulation of electron beams with speed and precision by electrostatic or magnetic fields	Electrons, being charged particles, need to be held in a vacuum, making the apparatus more complex than for photolithography
Imaging of electrons to form a small point of <100 Å, as opposed to a spot of 5000 Å for light in the case of photolithography	The slow exposure speed -an electron beam must be scanned across the entire wafer (for a 4-in wafer with a high feature density this requires ~ 1 h)
No need for a physical mask; only a *software mask* is required	Low throughput. Approximately 5 wafers per hour at less than 0.1 μm resolution.
The ability to register accurately over small areas of a wafer	High system cost
Lower defect densities	–
Large depth of focus because of continuous focusing over varying topography. At 30 keV, electrons will travel on average > 14 μm deep into a PMMA resist layer.	–

this type of slow, expensive fabrication technique prohibits commercial acceptance. Some microstructures, especially intricate microsystems, might be worth the bigger price tag. Nanostructures could also be readily achieved featuring dimensions not possible with photolithography. In those cases, serial microfabrication techniques may not be as prohibitive as they would be in the case of ICs.

Numerous commercial e-beam resists are produced for mask-making and direct write applications. Bombardment of polymers by electrons causes bond breakage and, in principle, any polymer material can function as a resist. However, important considerations include sensitivity, tone, resolution, and etching resistance. PMMA exemplifies an inexpensive positive e-beam resist with a high-resolution capability and a moderate glass transition temperature T_g (114°C). Microposit SAL601 is an often used negative e-beam resist. SAL601, being novolac-based, has much better dry etch resistance than PMMA resists. The same materials act as X-ray resists as well. This is not coincidental, as there is a strong relation between X-ray and e-beam sensitivity. A copolymer of glycidyl methacrylate and ethyl acrylate (COP) is another frequently used negative resist in mask manufacture. This material has (as is typical for acrylates) poor plasma-etching resistance but exhibits good thermal stability.

E-beam has been used by one of the authors on the fabrication of polymer nanostructures [172]. After pyrolysis, the resulting carbon nanoelectrodes are used for the detection of reversible redox species, such as the ferro/ferricyanide couple and dopamine (unpublished results). In the long term, the objective is to take advantage of the biocompatibility of the glass-like carbon and the higher sensitivity of the interdigitated electrode configuration to detect dopamine in living cells in vitro.

5.5.1.2 Focused Ion Beam Lithography

In ion-beam lithography, resists are exposed to energetic ion bombardment in a vacuum. Direct write ion-beam lithography or Focused Ion Beam (FIB) lithography consists of point-by-point exposures with a narrow ion beam generated by a source of liquid metal. Ion-beam lithography uses ions of a kinetic energy from a few keV up to several MeV. For ion-beam construction, liquid metal ion (LMI) sources are becoming the choice for producing high-current-density submicrometer ion beams. With an LMI source, liquid metal (typically gallium) migrates along a needle substrate. By applying an electrical field, a jet-like protrusion of liquid metal forms at the source tip. The gallium-gallium bonds are broken under the influence of the extraction field and are uniformly ionized without droplet or cluster formation. LMI sources hold extremely high brightness levels and a very small energy spread, making them ideal for producing high-current-density submicrometer ion beams. Beam diameters of less than 50 nm and current densities up to 8 A/cm^2 are the norm. In addition to gallium, other pure element sources are available, such as indium and gold. By adopting alloy sources, the list expands to dopant materials such as boron, arsenic, phosphorus, silicon, and beryllium.

Compared to photons (X-rays and DUV light) or electrons, ions chemically react with the substrate, allowing for a greater variety of surface modifications such as patterned doping. The ion-beam spot size is the smallest possible, smaller than UV, X-ray, or electron-beam spots. The smallest FIB spot achieved upto this date is about 8 nm, accomplished by using a two-lens microprobe system and a single-isotope gallium ion source. Ion lithography achieves higher resolution than optical, X-ray, or electron beam techniques because ions undergo almost no diffraction and scatter much less than electrons, since the secondary electrons produced by an ion beam are of lower energy and have a short diffusion range. The total spread including forward and backward scattering of the "stiffer" ion-beams is typically less than 10 nm and they only require about 1–10% of the electron dose to expose a resist. Materials that can be used as resists include an ordinary PMMA resist [173, 174] and SU-8 [175]. FIB shares the same drawbacks with an electron-beam system in that it requires a serially-scanned beam and a high vacuum. Because FIB systems operate in a similar fashion to a scanning electron microscope (SEM) they can be used for imaging (when operated at low beam currents) or for site specific sputtering or milling (when operated at high beam currents).

FIB can be used to perform maskless implantation and metal patterning with submicrometer dimensions. It has also been applied to milling in IC repair, maskless implantation, circuit fault isolation, and failure analysis. FIB systems have been produced commercially for approximately ten years, primarily for large semiconductor manufacturers. As a machining tool, FIB is very slow. Except for research, it may take a long time to become an accepted "micromachining tool." For additional reading on ion-beam lithography in general refer to [176]; for more specific reading on focused ion-beam-induced deposition, see [177].

FIB milling has been employed recently for the patterning of commercial "glassy" carbon. The resultant structures are used for the molding of borosilicate glasses and quartz [178–180]. A comparison between FIB, laser and mechanical milling for the patterning of carbon is given in [181, 182].

5.5.2 Nano Imprint Lithography

Nano Imprint Lithography (NIL) patterns a resist by deforming the resist shape through embossing (with a mold/stamp/template), rather than by altering the resist's chemical structure through radiation (with particle beams for instance). After imprinting the resist, a dry anisotropic etch is used to remove the residual resist layer in the compressed area to expose the substrate underneath. In NIL, a template (the mold/stamp/template) is made of a hard material (usually Ni or Si) and is pressed against a layer of polymer. High temperature and pressure conditions mold and harden the polymer layer. Stephen Chou, now at Princeton University but with the University of Minnesota at the time, invented the technique in 1995 [183, 184] The method relies on the excellent replication fidelity obtained with polymers and combines thermo-plastic molding with common pattern transfer methods. Once a solid stamp with a nano-relief on its surface is fabricated it can be used for the replication of many identical surface patterns. The resolution of the NIL process is a direct function of the resolution of the original template/stamp fabrication process. Electron beam writers that provide high resolution, but lack the throughput required for mass production, are used to make them.

The University of Texas (UT)-Austin developed its version of nanoimprint lithography, step-and-flash imprint lithography (SFIL), in 1998 [185]. In 2001, the SFIL concept was licensed to Molecular Imprints, Inc. (MII), a company that develops SFIL-capable tools (S-FIL® systems) and related processes. The SFIL method is distinct from the original NIL in its use of UV-assisted nanoimprinting that molds photocurable liquids in a step-and-repeat, die-by-die fashion rather than by heat-assisted molding of full, polymer-coated wafers. As shown in Fig. 5.15, in SFIL, a hard but transparent template/stamp/mold (fused silica) is used to mold

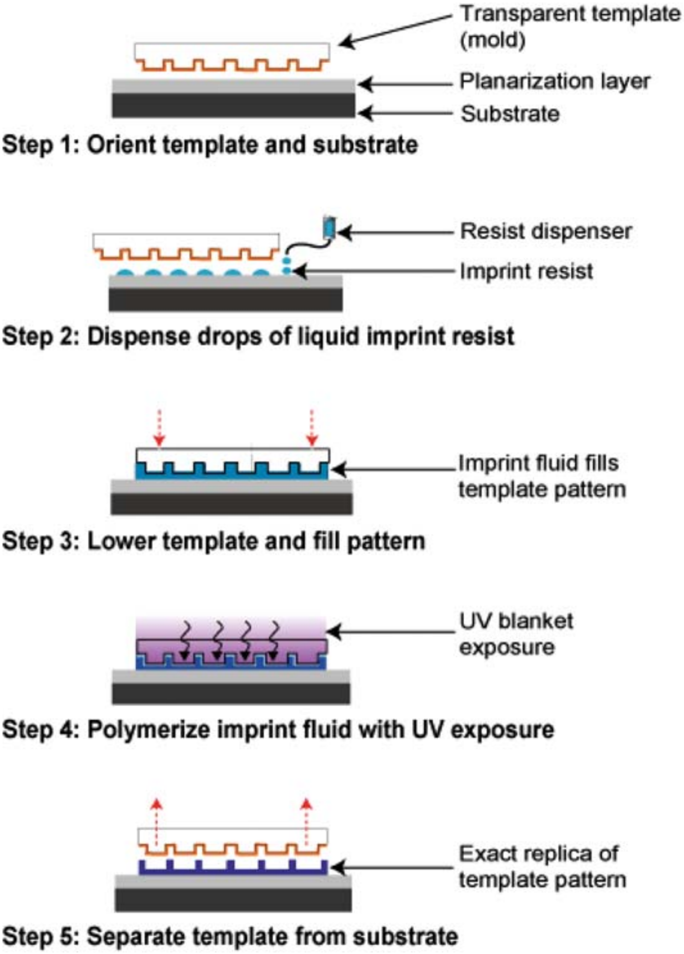

Fig. 5.15 Schematic of step-and-flash imprint lithography (SFIL). Adapted from www.molecularimprints.com

a polymer photoresist layer. The fused silica surface of the stamp, coated with a release layer, is gently pressed into the thin layer of low viscosity photoresist. The photoresist is subsequently exposed to UV light through the transparent template in order to harden it. Upon separation of the fused silica template, one layer of the circuit pattern is left on the wafer surface. Molecular Imprints uses a family of photo-curable, low viscosity materials called MonoMat$^{\mathrm{TM}}$ as its imprint resists. MonoMat$^{\mathrm{TM}}$ is comprised of an organic monomer that polymerizes in seconds using low cost, broadband UV light sources. Only the template fabrication process, typically accomplished with an e-beam writer, limits the resolution of the features. It has been demonstrated that the mold templates do not deteriorate even after 1500 imprints with sub-100 nm feature sizes.

Imprinting processes are economical due to the simplicity of the equipment involved and the potential for high-throughput. As the rate of improvements in optical lithography decelerates and the costs of manufacturing continue to escalate, there is an increased interest in imprinting and molding as alternative processes for micro and nanofabrication. SFIL is one of the few methods currently available for low-volume prototyping at the 32 nm node. Sub-20 nm features have been made to date that exceed the present requirements in the International Technology Roadmap Semiconductors (ITRS). The SFIL process is now also being explored for manufacturing of several emerging technologies, such as photonic crystals, micro/nano-optical components, and nanopatterned magnetic media for future hard disk drives. The original Thermal NIL using thermoplastic polymer films is focused on applications such as bio-chips, life sciences, storage media and optical devices. Progress in these new areas has been such that Imprint Lithography is likely to find its first commercial manufacturing application in one of these emerging technologies well before it would be required for high-volume, sub-50-nm semiconductor lithography. A notable feature of nanoimprint technologies is their relatively low cost, which allows researchers to explore applications of nanopatterning that would never be economically feasible given the extraordinary cost associated with extreme ultraviolet (EUV) lithography or even current-generation 193 nm steppers. However, the approach faces alignment challenges, and critics say the cost of making the reticles will be high. Unlike conventional lithography, with mask patterns that are 4 × larger than the printed image, nanoimprint is a 1:1 template technology.

5.6 Microfluidic and Electrochemistry Applications

Micro and nanofabrication techniques like the ones presented above have recently made possible a significant number of breakthroughs in different fields, including environmental, clinical, pharmaceutical and biochemical technologies. The miniaturization of analytical systems offers important advantages such as lower cost, reduced sample and reagent consumption, shorter response time, and greater sensitivity and portability [186–190]. Moreover, quality and performance improvements are making it possible for microanalytical systems to become common aids to many different applications [187, 191, 192].

Although the above-mentioned techniques were described as ways to fabricate polymer precursor structures for carbonization, they can also be utilized to fabricate the polymer designs to be used as fluidic manifolds for a variety of applications. Polymer structures can further serve as master molds for casting of elastomers and other polymers such as in Soft Lithography [193–196]. The reader is encouraged to review further references on polymeric microfluidic devices and their means of fabrication [197–199].

Even when glass-like carbon does not strike as the ideal structural material for microfluidic manifolds, it does offer several advantages in the fabrication and of elements to be incorporated in microfluidic devices, i.e., electrodes. These electrodes can be used for sensing, as in the case of electrochemical detection of glucose or dopamine, or for actuating, as in dielectrophoresis-based particle manipulation. The use of glass-like carbon brings several advantages: (1) Carbon has a wider electrochemical stability window than gold or platinum, so that more voltage can be applied to the carbon electrodes without inducing electrolysis in the solution, (2) it has an excellent biocompatibility, carbon is the building block of nature, (3) carbon is chemically inert to most solvents and (4) it presents excellent mechanical properties. It is important to mention that as with other commonly used materials, polymers in particular, it is possible to change the hydrophobic properties of carbon using surface treatments [200]. This is a very important feature for the fabrication of microfluidic devices, as contact angle plays a very important role in most of them. The following applications detail the use of glass-like carbon elements in microfluidic and electrochemical applications.

5.6.1 Carbon-Electrode Dielectrophoresis (carbon-DEP)

Separation and sorting techniques strive to isolate a targeted particle population from a mixture of various populations by taking advantage of the differences between particle's characteristics. Properties that can be exploited include size, geometry, density, protein affinity and light scattering but additional tags, such as fluorescent or magnetic, might be attached to a particle population to enhance the level of discrimination. These additional tags enable flow cytometry technologies such as FACS^{TM} (Fluorescence Activated Cell Sorting) and other cell sorting technologies like MACS^{TM} (Magnetic Activated Cell Sorting). However, the required linkage of these tags to expensive antibodies increases the cost of the assay per patient.

Dielectrophoresis (DEP) [201, 202] uses only the dielectric properties of the targeted particles for their isolation from a mixture. Different particles present characteristic dielectric properties based on their phenotype, i.e., their membrane structure and surface properties, their internal compartmentalization and other physical characteristics. The collection of these properties gives to each particle a unique dielectric signature and a characteristic dielectrophoretic behavior when under the influence of a non uniform electric field [203–207]. This approach eliminates the use of additional tags and potentially reduces the cost of a given assay.

DEP refers to the induction of a dielectrophoretic force, F_{DEP} [4], on a polar particle immersed in a polar media by a non uniform AC or DC electric field. As the particle interacts with the established electric field gradient, a dipole moment, with a specific magnitude and direction, is induced on it [208, 209]. The magnitude of F_{DEP} is mainly determined by the value of the electric field gradient and the radius of the particle while the direction is given by the relative difference of the dielectric properties between the particles and their surrounding media.[5] DEP is a non-destructive electrokinetic transport mechanism and is highly amenable to miniaturization since the magnitude of the induced force scales favorably with the reduction of the distance between the electrodes [210]. F_{DEP} is also strongly dependent on the voltage applied between electrodes and it gradually vanishes as the distance from an electrode surface is increased and the electric field gradient tends to disappear (see Fig. 5.16).

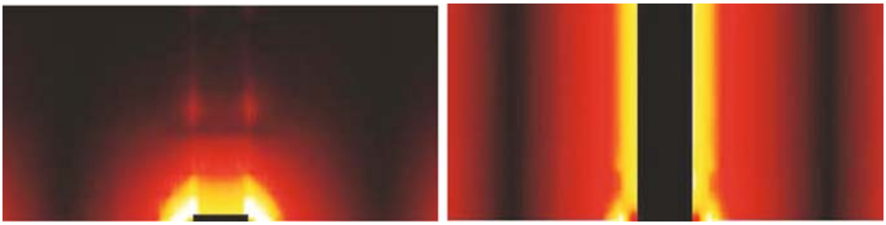

Fig. 5.16 Finite Element Analysis of the electric field induced by two different electrode geometries: (*left*) 2D and (*right*) 3D. Note how in both cases the F_{DEP}, directly dependent on the induced electric field gradient, gradually vanishes as one moves away from the electrode surface. F_{DEP} is strongest in lighter areas and weakest in darker areas. The darkest square areas in the middle represent the electrodes. Results obtained in collaboration with Tecnológico de Monterrey, Campus Monterrey in Mexico

Due to advances in microfabrication technology achieved in the last 20 years by the IC industry, the traditional method to induce DEP has been based on the use of planar metal electrodes [211–214]. The main advantage of this approach is the

---

[4] F_{DEP} is given by the equation $2\pi\varepsilon_m r^3 \mathrm{Re}[f_{CM}]\mathrm{grad}(E_{rms}^2)$ where ε_m is the permittivity of the medium, r is the particle radius, $\mathrm{Re}[f_{CM}]$ denotes the real part of the Clausius-Mossotti factor and $\mathrm{grad}(E_{rms}^2)$ illustrates an electric field gradient. E is given by V/d where V is the voltage applied to the electrodes and d represents the distance between them.

[5] This difference is given by the Clausius-Mossotti factor. This factor is named after the Italian physicist Ottaviano-Fabrizio Mossotti, whose 1850 book analyzed the relationship between the dielectric constants of two different media, and the German physicist Rudolf Clausius, who gave the formula explicitly in his 1879 book in the context not of dielectric constants but of indices of refraction. The Clausius-Mossotti factor is given by $(\varepsilon_p^* - \varepsilon_m^*)/(\varepsilon_p^* + 2\varepsilon_m^*)$. ε^* denotes complex permittivity and is given by $\varepsilon + (\sigma/i\omega)$ where ε is the permittivity, σ is conductivity, i denotes the square root of -1 and ω is the angular frequency of the applied electric field; p and m denote particle and media respectively.

creation of high electric field gradients employing low applied voltages. However, the use of metal electrodes limits the magnitude of the applied voltage in order to prevent electrolysis. In terms of fabrication, even when the fabrication of planar metal electrodes is relatively easy and readily achievable, the fabrication of three-dimensional electrodes is rather cumbersome. 3D structures require the use of more complicated techniques, such as electroplating, that might result in low fabrication yields. This limitation often results in expensive devices that halt the wider adoption of metal-electrode DEP for commercial applications. An alternative to metal electrodes is the use of insulator-based DEP (iDEP) [215–219]. In this approach, a uniform electric field is applied across an array of insulating structures by a couple of conductive electrodes. The presence of the insulating structures distorts the uniform electric field rendering it non uniform around them. Because the conductive electrodes on either side of the insulating electrode array are separated by a few millimeters, the magnitude of the applied voltage must be significant. One of the primary drawbacks of an iDEP system is precisely the requirement of a high-voltage excitation source to apply the required high electric fields across the insulating array. Another major disadvantage is that such fields can cause significant Joule heating and damage biological particles. iDEP also greatly depends on sample composition. In order to avoid Joule heating, only low-conductivity samples can be used. On the positive side, the possibility of electrolyzing the sample is greatly reduced in iDEP, since the sample is only in contact with an insulating material. Furthermore, insulating structures can be readily fabricated in planar or 3D shapes with fabrication techniques that do not require infrastructure as expensive as metal deposition equipment.

Regardless of the material, the use of 3D electrodes in DEP applications allows for higher separation throughputs than when 2D electrodes are used. This advantage is provided by the fact that, given a channel cross-section, many targeted particles immersed in the bulk volume of the channel flow over the planar electrodes without experiencing any force. This makes it necessary to re-flow the same sample several times, a procedure that negatively impacts biological samples. The use of 3D structures that penetrate the bulk of the channel greatly reduces the mean distance of any particle to its closest electrode surface (see Fig. 5.17).

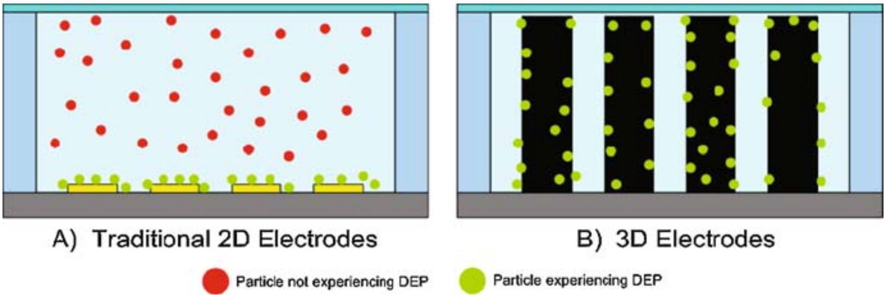

Fig. 5.17 A schematic showing how the use of 3D electrodes is advantageous over 2D ones. Given a channel cross-section, more particles will experience F_{DEP} when using 3D electrodes

DEP has been successfully applied to the manipulation and concentration of a wide array of bioparticles; from proteins [219–221] to microorganisms [222–226], including mammalian cells [214, 227–232] and viruses [205, 233–236]. Several applications have been demonstrated using planar (2D) metal [230, 237, 238] or volumetric (3D) insulator-based electrodes [239, 240], until now the two main trends on the material choice and geometry for electrodes.

Even when the general tendency when employing metals has been to use planar electrodes, few examples of micro fabricated three-dimensional (volumetric) electrodes have been recently implemented. Wang et al. [241] and Voldman et al. [242] used electroplated gold electrodes for particle focusing and for particle trapping for cytometry applications, respectively. Illiescu [243] used complex microfabrication techniques to obtain volumetric doped silicon electrodes in a multi-step process. Another true 3D approach, although not technically microfabricated, is the one described by Fatoyinbo et al. [244], who in an elegant solution used a drilled insulator-conductor sandwich to obtain wells with electrodes all along their walls.

In contrast to the approaches exposed above, carbon-electrode Dielectrophoresis (carbon-DEP) is a technology that employs carbon structures or surfaces as electrodes. The use of carbon as electrode material offers several advantages that make it a more suitable material than those traditionally used in DEP including gold, platinum or other conductive materials such as Indium Tin Oxide (ITO) or doped silicon. Carbon-DEP combines the advantages of metal-based and insulator-based DEP. More specifically, carbon has a wider electrochemical stability window making electrodes less likely to induce electrolysis and less prone to fouling when compared to metal electrodes. Carbon electrodes (planar, volumetric or a combination of both) can also be fabricated relatively inexpensively and with high yields when using fabrication techniques such as C-MEMS. When compared to insulator-based electrodes, or iDEP, the main advantage is that carbon electrodes prevent the use of high voltages and high fields to induce DEP. Carbon is conductive enough to allow for the use of low voltages to apply the required electric fields to induce DEP, thereby minimizing damage to biological particles. Furthermore, it has already been demonstrated that carbon is a highly biocompatible material [86, 129]

The fabrication of carbon-DEP devices, as it is done currently, emanates from the manufacturing of polymer structures. Such structures have commonly been fabricated in SU-8 photoresist following a two-step photolithography process (see Fig. 5.18a). Two steps are needed in order to fabricate the connection leads to

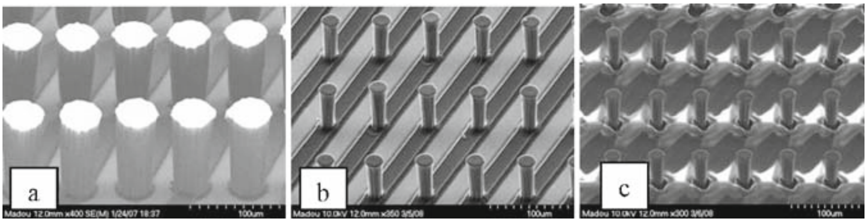

Fig. 5.18 (**a**) SU-8 polymer arrangement featuring posts and connection leads. (**b**) Carbon electrodes obtained after pyrolysis. (**c**) A thin polymeric layer patterned around carbon electrodes

the electrodes and the electrodes themselves since they do not usually feature the same topography. An alternative is to pattern the connection leads out of evaporated metal. The substrates have been limited so far to silicon wafers with a thick layer of silicon dioxide, which acts as the electrical insulator underneath the carbon electrodes. This limitation is mainly due to (1) the high temperatures of the pyrolysis process and (2) the fact that structures will lift-off from substrates that have a coefficient of thermal expansion that does not match the one of the different products being synthesized during pyrolysis, from the precursor polymer to the final glass-like carbon. Carbon and silicon happen to have very similar coefficients of thermal expansion (CTE) during the pyrolysis process; the CTE of glass-like carbon changes from 2.85 to 3.7×10^{-6}/K [245, 246] while that of silicon falls in between 2.6 and 4.442×10^{-6}/K [247]. Quartz wafers have been employed before as substrates with limited success. Titanium and chromium leads have also been fabricated with no better results.

Once the polymer precursor is patterned, it is introduced inside a high temperature furnace for carbonization. This requires the use of an inert atmosphere in the furnace during pyrolysis to prevent combustion of the structures. The carbonization process takes approximately 4 h with an additional 6–8 h for cooling.

An example of the resulting carbon electrodes and their connection leads is shown in Fig. 5.18b. A certain degree of isometric shrinkage with respect to the original polymer structures is always obtained. An optional further step is the patterning of a thin polymeric layer around the electrodes as shown in Fig. 5.18c. This layer serves two purposes: (1) to planarize the channel bottom and (2) to protect the carbon leads and electrodes from lifting-off when immersed in aqueous media.

The next step is to embed the DEP active area, delimited by the carbon electrodes, in a fluidic network. This network includes channels, chambers and fluidic interfaces to the outside world for sample loading and retrieval. Several approaches and materials for the fabrication of the fluidic network have been implemented by the authors, including SU-8, Poly(dimethylsiloxane) (PDMS) and polycarbonate (PC). The polycarbonate approach has yielded the most rapid, affordable and robust solution. An example of a carbon-DEP device and its cross section using PC is shown in Fig. 5.19. For more fabrication details the reader is referred to [134]

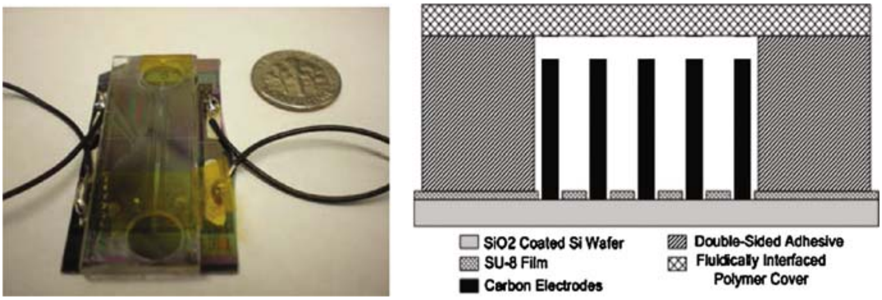

Fig. 5.19 An example and cross-section of a CarbonDEP chip using polycarbonate to fabricate the fluidic network

Fluido-dynamic and electromagnetic modeling and simulation of carbon-DEP devices have already been conducted [121, 130, 133, 134]. Figure 5.20 shows some of these results obtained with Finite Element Analysis. As depicted in the electromagnetic simulation results (Fig. 5.22c and d), an electric field gradient is established in the media with an electric field magnitude that has its maximum at the electrode surfaces and decreases as one moves away from them. This electric field distribution yields two different regimes of DEP: positive DEP (pDEP) and negative DEP (nDEP). The sign, or direction, of F_{DEP} is given by $\mathrm{Re}[f_{CM}]$. From the particle's point of view, it will experience pDEP when its permittivity is higher than that of the media ($\mathrm{Re}[f_{CM}]$ is positive), and it will undergo nDEP when the media permittivity is higher than its own. In other words, the most polarizable element always gets directed to the regions with highest electric field magnitude. The magnitude of F_{DEP} is given by the magnitude of the established gradient; the sharper

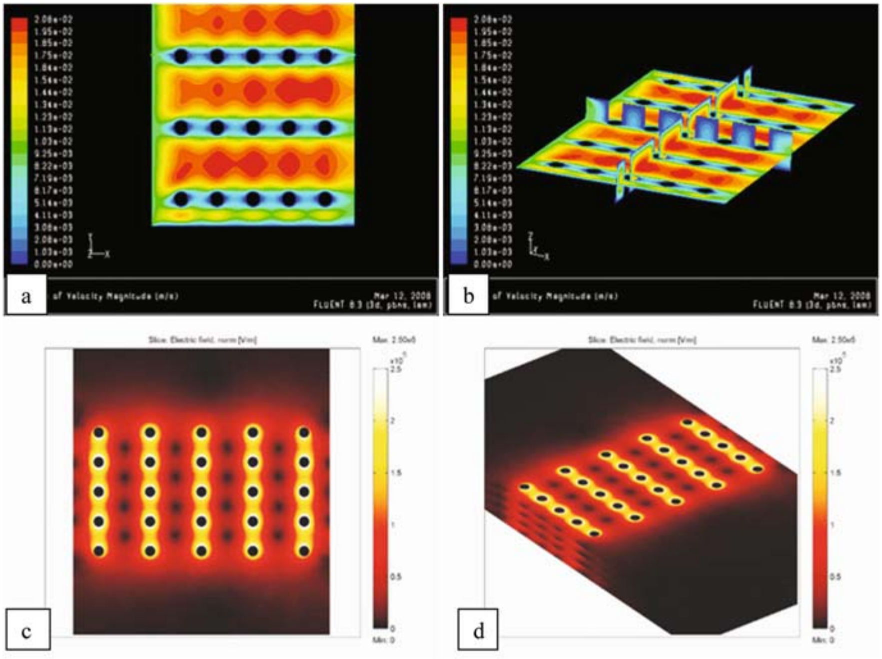

Fig. 5.20 Flow velocity and electric fields induced in a DI water-based conductive media ($\sigma = 10$ mS/m) by a polarized carbon electrode array. (**a**) Top and (**b**) isometric views of the flow velocity field. Flow is in the horizontal direction. Highest velocity is 2 mm/s and is given by red colors in between the posts. Minimum velocity is 0 mm/s, denoted by darker blue colors present on the electrode and channel surfaces due to the no-slip condition. A flow rate of 10 μl/min was simulated. (**c**) Top and (**d**) isometric views of the induced electric field when polarizing electrodes at 10 V_{pp}. Maximum value is 2.5×10^5 V/m, given by lightest colors, and is present on the electrode surfaces. The minimum value of 0 V/m is present in the regions farther away from the electrodes and is illustrated by the dark regions. Simulation results obtained in collaboration with Tecnológico de Monterrey, Campus Monterrey in Mexico and Universitat Rovira i Virgili in Catalonia, Spain

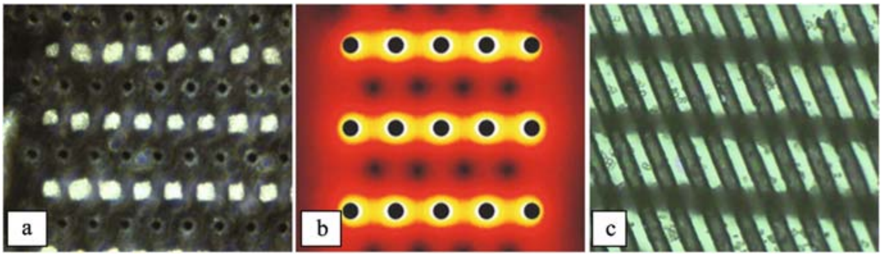

Fig. 5.21 Experimental validation (**a** and **c**) of simulation results (**b**). Latex particles get clustered in nDEP volumes as shown in (**a**) (correlate light areas denoting latex particles with darker areas in b delineating nDEP regions) and yeast cells get trapped in the vicinity of the electrode surfaces by pDEP (correlate darker areas on (**c**) with lighter (**a**) areas of (**b**). Maximum electric field magnitude is 2.5×10^5 V/m and is given in the lightest areas of b. Minimum magnitude is 0 and is given by the darkest areas of (**b**)

the gradient the stronger F_{DEP} is. Figure 5.21 shows the experimental validation of the simulation results: 8 μm latex particles, usually less polar than the media containing them, become clustered by a negative F_{DEP} in nDEP regions, while yeast cells, immersed in a less polar media, get attracted to the electrode surfaces, the pDEP region, by a positive F_{DEP}.

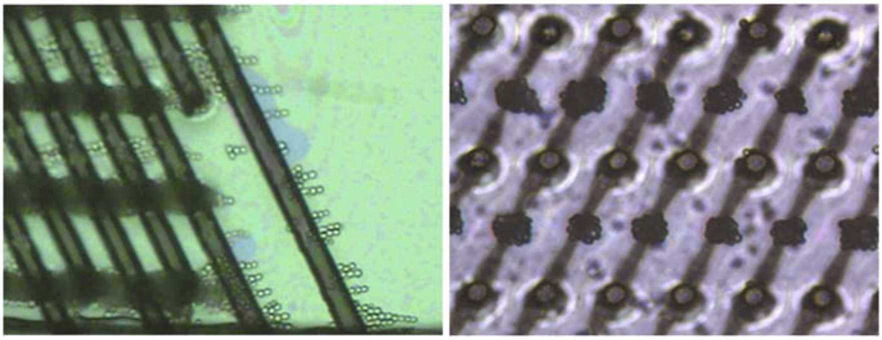

Fig. 5.22 Filtering of yeast cells with pDEP (*left*) and selective positioning of latex particles with nDEP (*right*)

Carbon-DEP has been demonstrated for a variety of functions including positioning [137], filtering [132] and separation of targeted particles [131, 132]. Selective filtering and positioning are shown in Fig. 5.22. The advantages of using 3D electrodes over 2D ones, specifically higher throughput and better efficiency, were demonstrated when using glass-like carbon electrodes to filter viable from non viable yeast cells [131].

A novel multi-stage filter, as depicted in Fig. 5.23, has also been implemented. With this approach it is possible to excite different electrode arrays embedded in a channel using different electric fields. Each one of these fields is optimized in their magnitude and frequency to trap specific particle populations at each array.

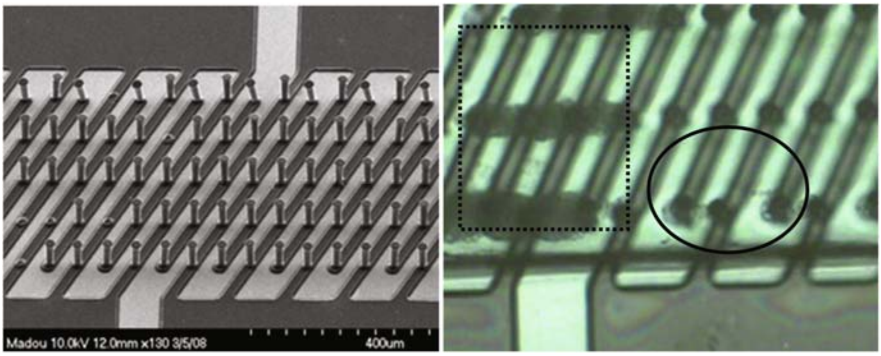

Fig. 5.23 A multi-stage filter featuring two stages. *Left*: fabricated CarbonDEP device. *Right*: Non viable yeast cells are trapped in one array (*dotted square*) while viable yeast get trapped in the other (*solid ellipse*)

By implementing a sequential release protocol one can then retrieve each of the different populations at the end of the channel at different times [132]. Another promising application is the continuous separation of particles by pDEP focusing, as demonstrated in Fig. 5.24. The principle works when the hydrodynamic force overcomes the pDEP trapping force. Since laminar flow is established in the channel, the particles attracted to pDEP regions flush away contained in those streamlines co-linear with the polarized electrode rows (and pDEP areas). Such principle allows continuous separation at higher flow rates than those achieved when implementing separation by trapping, such as in a filter, but requires more complicated

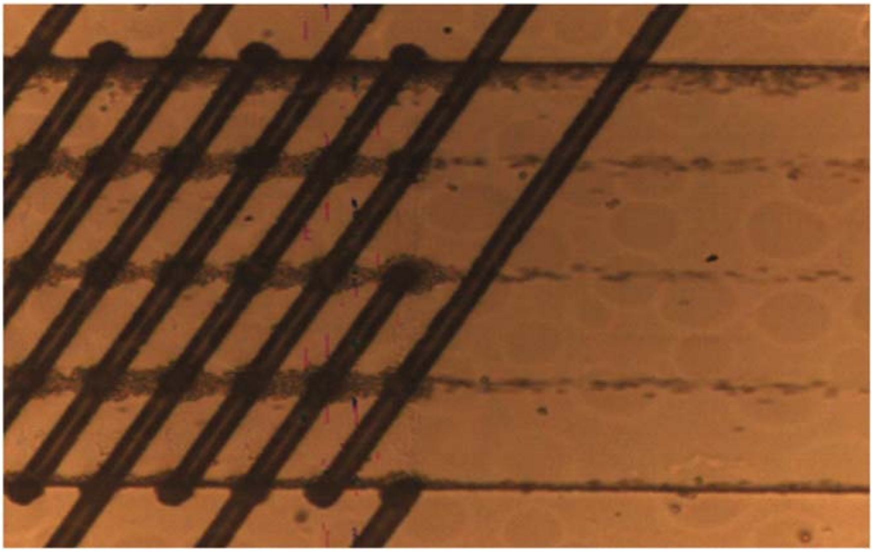

Fig. 5.24 Continuous separation of viable yeast cells using pDEP focusing

geometries for enriched population retrieval. pDEP focusing can be further combined with nDEP focusing to implement a continuous enrichment scheme of two different populations [134]. More recently, carbon-DEP has been integrated in a Compact Disk (CD)-like centrifugal platform (pictured in Fig. 5.25) towards implementing a portable and automated cell separation platform employing DEP [135].

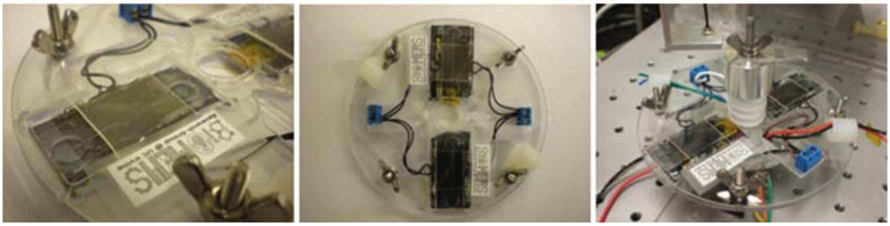

Fig. 5.25 Different views of a SpinDEP platform featuring carbon-DEP devices integrated in a CD-like centrifugal platform

5.6.2 Electrochemical Uses of Carbon in Microfluidic Applications

Previous sections have presented the use of glass-like carbon in dielectrophoresis to manipulate colloids and suspended particles. This subsection is dedicated to discuss the applications of glass-like carbon in electrochemical transducers, specifically sensors and biosensors. We first give a short overview of the specific benefits of using carbon as electrochemical sensors and how photoresist-derived glass-like carbon compares to commercial “glassy” carbon electrodes. Two different sensor geometries, interdigitated electrode arrays and fractal electrodes, are then presented along with their means of fabrication. The subsection ends with an example on the use of carbon electrodes.

Carbon presents a unique combination of properties that make it very suitable for electrochemical applications, namely, good electrical conductivity, acceptable corrosion resistance, availability in high purity, low cost, dimensional and mechanical stability, and ease of fabrication into composite structures [107]. Not surprisingly, the use of carbon in microfluidics is intimately linked to its behavior as electrode material. Regarding the use of carbon as a sensor, an outstanding and very useful property of carbon is that it can be functionalized with surface molecules which allows for the creation of sensors with higher selectivity and lower detection limits. It is important to mention that in order to functionalize its surface, the electrodes first need to be activated. One simple method to make its surface more reactive is by treating it with oxygen or water plasmas [248] and is even possible to selectively functionalize carbon electrodes using variations of the work presented in [249].

The expanding set of techniques for the fabrication of micro- and nanostructures in carbon opens up an entire new world of possibilities for the integration of carbon electrodes with microfluidic systems. Both individual and arrays of micro- and nano-electrodes, created for example with photolithographic methods, enable larger surface to volume ratios and translate into sensors with higher signal-to-noise ratios and enhanced sensitivities [45]. If certain geometries are used, for instance, interdigitated electrode arrays, this sensitivity can be further enhanced using redox cycling mechanisms, as it will be seen further below. The use of micro- and nano-electrodes results in three important consequences for the electrochemical behavior of these electrodes when compared to electrodes at the macro-scale: (1) the mass transport rates to (and from) the electrodes are increased, (2) the double layer capacitance is reduced due to the decrease in surface area, and (3) the ohmic losses (the product of the electrode current and the solution resistance) are reduced due to diminished current [250]. The choice for arrays or individual micro or nano-electrodes will depend on each targeted application, but both types can be successfully combined with microfluidic devices. In this sub-section, only applications related to the use of arrays of microelectrodes will be discussed. Details will be given on the derivation of carbon electrodes from photoresists, such as SU-8, and how its electrochemical behavior compares to the commercial “glassy” carbon.

As mentioned before, several studies have shown that the carbon obtained through pyrolysis of photoresists presents an electrochemical behavior similar to the glass-like carbon derived from other phenolic resins or polyfurfuryl alcohols. Using cyclic voltammetry it can be shown that oxygen reduction at photoresist-derived electrodes begins at about − 0.4 V vs. SCE (Saturated Calomel Electrode), a value similar to that of commercial “glassy” carbon [117, 251]. Moreover, the analysis and comparison of electron-transfer kinetics of various redox systems (such as $Ru(NH_3)_6{}^{3+/2+}$, chlorpromazine, $Fe(CN)_6{}^{3-/4-}$ and dopamine) show well-defined, symmetric voltammograms for all the redox systems under consideration, which indicates that electrodes fabricated through the pyrolysis of photoresist have the same attractive features for electroanalytical applications than their commercial “glassy” counterparts; including low capacitance and weak adsorption properties [65, 252].

We now proceed to detail some possible fabrication techniques and applications for two different sensing arrays: interdigitated and fractal electrodes.

5.6.2.1 Interdigitated Electrode Arrays

Interdigitated electrodes used in electrochemistry typically consist of two comb-like electrodes on a planar surface. A distinct electrochemical advantage of this configuration is that redox compounds can undergo “redox cycling” [253] by oxidizing a compound on one electrode (the generator) and reducing it at the other (the collector) (See Fig. 5.26). The advantages of using interdigitated electrode arrays (IEAs) for the detection of reversible redox species have been studied, both theoretically and experimentally, by several groups [254–256]. One of the pioneering research papers [257] derived the electrical and electrochemical behavior of such electrode arrays and showed that, by decreasing their size, sigmoidal current responses are obtained. These curves are indicative of enhanced mass transport due to nonlinear radial diffusion. Furthermore, reducing the spacing gap between the generators and

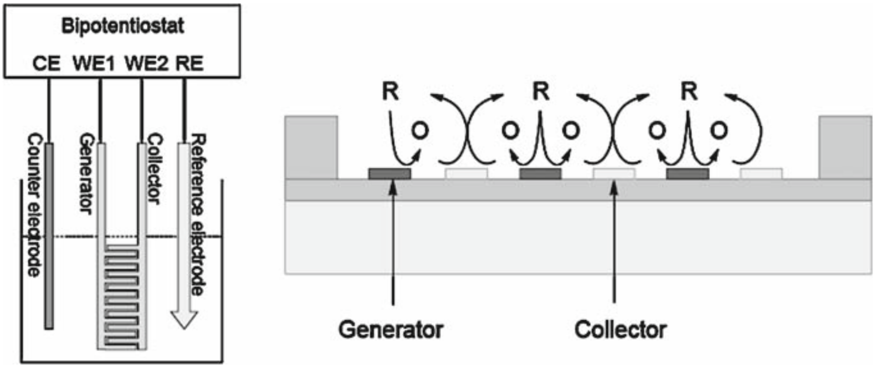

Fig. 5.26 *Left*: Schematic representation of the experimental setup of dual-mode electrochemical experiments using interdigitated electrode arrays. *Right*: Current enhancement mechanism for redox cycling on an interdigitated electrode (R: reduced molecule, O: Oxidized molecule). From [259] Re-printed with permission of BASi Inc

collectors leads to increased collection efficiency, enhanced redox cycling current, and decreased equilibrium time. For instance, by reducing the electrode gap from 1 μm to 50 nm, the collection efficiency increases from 89.40 to 99.95% [258].

Interdigitated electrode arrays are currently microfabricated using noble metals such as gold or platinum, but this results in unstable electrodes if a metallic adhesion layer is placed underneath the noble metal (for instance, Ti under Au), as this creates a galvanic couple that degrades the electrodes in just a few hours of being in contact with the electrolyte [172]. A further disadvantage is that the fabrication process is lengthy as it is based on the lift-off technique [172]. In contrast, the use of photoresist-derived carbon yields much more stable IEAs (as carbon do not degrades when in contact with an electrolyte) and dramatically cuts fabrication time (as it is simplified to a basic photolithography process and pyrolysis). This results in arrays that are simpler to fabricate, easier to miniaturize and less expensive than IEAs made with noble metals.

As mentioned above, interdigitated carbon electrodes can be derived by pyrolyzing polymer microstructures obtained with traditional lithographic methods, but in order to reduce their critical dimensions (gaps and widths), advanced lithographic techniques need to be used. The size reduction of the electrodes in an IEA to a nanoscale yields Interdigitated Nano-Electrode Arrays or INEAs. Two techniques, among others, that allow this size shrinking are electron-beam lithography (EBL) and nano-imprint lithography (NIL). These two methods do not rely on the wavelengths of light in the UV or deep-UV ranges, and therefore allow for much finer patterning of the photoresist precursor. That makes it possible to fabricate electrodes with gaps in the order of a few tens of nanometers. On the commercial side, it is important to note that NIL is expected to be of crucial importance to bring carbon-based INEAs into large-scale production, since it allows for parallel processing of the substrates (see section on NIL). On the other hand, EBL is extremely useful when the objective is to test and optimize different electrode designs, given its higher flexibility in the implementation of electrode geometries (see section on EBL).

Carbon-based INEAs offer high amplification factors that have enabled the monitoring of short-lived chemicals present at very low concentrations, (e.g. exocytosis of catecholamines from neurons) [260, 261]. They have also made possible the sub-femtomole detection of catecholamine in high-performance liquid chromatography (HPLC) [262]. A fabrication technique similar to the C-MEMS one discussed in this chapter was reported by Kostecki in 2000 [116].

5.6.2.2 Fractal Electrodes

Another strategy that can be pursued in order to increase the detection signal from carbon-based sensors is to increase their surface using fractal structures. Fractal-like geometries are ubiquitously found in nature, especially in situations that require minimizing the work lost, due to the transfer network, while maximizing the effective surface area. This is the case in vascular systems and energy-harvesting interfaces, to name a few. Fractals yield advantageous electrochemical characteristics as well [139], and have been proposed as the optimal geometry to be used in the design and fabrication of sensors and energy systems [263, 264].

In order to fabricate carbon fractal electrodes, the general process can be split in two main modules: (1) the backbone and (2) the fractal. The carbon backbone can be conveniently derived from photolitographically defined polymer micro-structures as detailed in the previous sections. The fractal geometries can be built up at the sub-micron and nano-scale using a range of methodologies and fabrication techniques and eventually get combined, if necessary, with the pre-existing carbon backbone architectures to obtain all sorts of fractal-like geometries. Some of the methods and techniques to fabricate fractals and to combine them with the backbone are briefly presented here:

Self-Assembling. Self-assembly is one solution to the problem of synthesizing structures larger than molecules. The stability of covalent bonds enables the synthesis of almost arbitrary configurations of up to 1000 atoms. Larger molecules, molecular aggregates, and forms of organized matter more extensive than molecules cannot be synthesized bond-by-bond. Self-assembly is one strategy for organizing matter on these larger scales, and it offers a route to three-dimensional microsystems [265]. This approach can be used to add pre-fabricated structures, synthesized either from organic precursors or carbonaceous materials, to the Carbon-MEMS (C-MEMS) backbone structures. It is important to note that these C-MEMS structures can already have several levels of “fractality” before being decorated with the self-assembled structures.

Resorcinol-formaldehyde (RF) based carbon xerogel microspheres and high surface area fractal-like structures have been successfully prepared by inverse emulsification of RF sol in cyclohexane in the presence of a non ionic surfactant, followed by pyrolysis at 900°C under inert nitrogen atmosphere. This processing technique leads to either carbon particles or carbon “flowers”, depending on the exact processing conditions. Increasing the surfactant concentration leads to smaller and relatively mono-dispersed spherical particles, whereas further increase in surfactant concentration leads to the formation of oval shaped structure and ultimately to high surface area fractal structures (see Fig. 5.27).

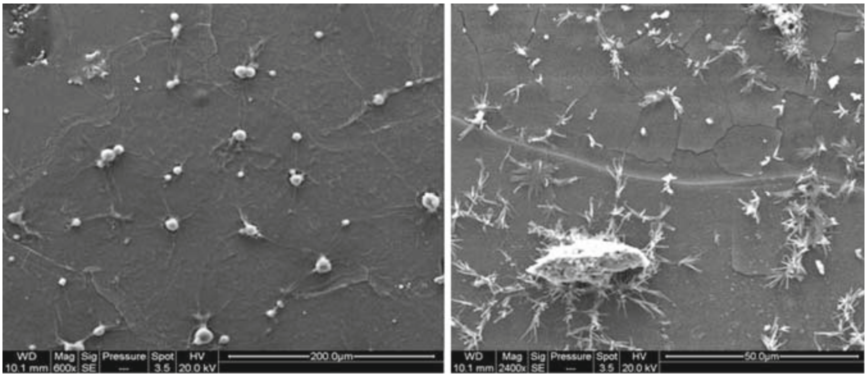

Fig. 5.27 Different geometries based on RF gel processing. Images courtesy of C.S. Sharma from the Indian Institute of Technology, Kanpur

These structures can be easily integrated with C-MEMS structures using different methods. One possible method of integration is described as follows: the RF gel is uniformly distributed over the three dimensional microstructure, for example, by spin coating. After drying, the gel solidifies and covers the three dimensional microstructure. Following pyrolysis, the RF gel is carbonized resulting in a conformal coating of carbon “particles” or “flowers” over the underlying Carbon-MEMS microstructures.

Another possible approach is to use commercially available carbon particles, such as Meso-Carbon-Micro-Beads (MCMB, Osaka Gas Inc., Japan). In this case, carbon particles are uniformly dispersed in a solvent, for example, N-Methyl-2-Pyrrolidone (NMP). The colloidal solution is then uniformly distributed over the three dimensional microstructure, for example, using spin coating. The surface tension of NPM drags the particles to the polymer microstructures during evaporation. Once the solvent evaporates, the carbon particles remain adhered to the microstructures by Van der Waals forces and capillary forces (see Fig. 5.28).

Electrodeposition and Templating. The appearance of fractal interfaces is a common problem in electroplating. Fractal structures can be purposely created when electrodepositing a polymer by controlling the composition of the deposition solution and by controlling the voltage and current [266]. These polymer structures can then be carbonized to yield a carbon fractal. In addition, cracks and other failures in materials often have a fractal nature. These cracks and crevices can be used as templates for electrodeposition.

Chemical Vapor Deposition (CVD). In this method, a standard photolithography process is followed using SU-8 photoresist premixed with carbon nanofibers

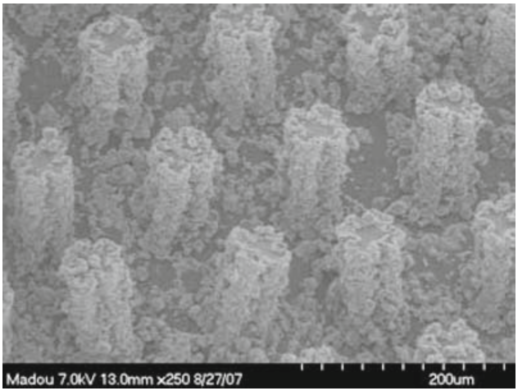

Fig. 5.28 MCMB particles adhered to microstructures after solvent drying

(CNFs). The CNFs are mixed with the SU-8 resin (1% in weight) prior to the process. This doped photoresist is then spin-coated onto a silicon wafer to an approximate thickness of 100 μm. A standard photolithographic process is then conducted. The resulting structures exhibit some clumps of CNFs that are partially embedded inside SU-8 posts. The carbon nanofibers can withstand the pyrolysis process and stay attached to the carbon post [267]. The resulting nanostructures are electrically connected to the carbon microstructure.

It is also possible to use CVD techniques to deposit Multi-Walled Carbon Nano-Tubes (MWCNTs) on the Carbon-MEMS structures [120]. MWCNTs are usually grown on planar substrates; therefore it is quite challenging to grow carbon nanotubes on 3D surfaces because of the difficulty to coat the required catalyst from where the CNT grow uniformly all over a 3D surface. To achieve this, thin Fe films were coated onto the carbon structures through pulsed laser deposition (PLD) on the rotating 3D C-MEMS substrates. The coated C-MEMS substrates were then used for growing MWCNTs in a thermal CVD system.

5.6.2.3 Glucose Sensors

An example of the use of carbon structures as sensors is that of enzyme-based glucose sensors. In enzymatic glucose sensors, glucose oxidase (GOx) is typically used as the biological enzyme to form the electrochemical transducer. In the presence of oxygen, GOx catalyzes the electro-oxidation of glucose, giving as result gluconic acid and oxygen peroxide. Then, the peroxide present at the surface of the carbon electrode is further oxidized to one molecule of oxygen and two protons, with the release of two electrons. The electrochemical current produced in this overall reaction is proportional to the concentration of glucose in the solution, and it can be used as a sensing principle. The complete reaction is represented below:

$$\text{Glucose} + O_2 \rightarrow \text{gluconicacid} + H_2O_2$$
$$H_2O_2 \rightarrow O_2 + 2H^+ + 2e^-$$

The most common materials for the immobilization of GOx include noble metals, such as platinum or gold [268, 269]; and carbon, both graphitic and glass-like carbon [270]. By using novel microfabrication approaches, it is possible to increase the specific surface area of the electrodes to immobilize more glucose oxidase per footprint unit and achieve a sensor with a larger signal per unit of surface [128].

The immobilization of the enzymes on the surface of the carbon electrodes can be done with two main techniques: enzyme [271, 272] and co-deposition [273, 274]. Redox enzymes are incapable of direct contact with the electrodes since their redox centers are insulated from the conductive support by protein matrices [275]. In order to contact these enzymes with the electrode, mediators, which are dependent on the specific enzyme being used, are utilized. Several types of schemes have been developed to enable this electric contact. Examples of such efforts include the development of high-surface-area electrodes by graft polymerization of a redox polymer entrapping the enzyme [276], the utilization of carbon black [277], and the fabrication of cylindrical and porous carbon tubes electrodes with higher surface area [278]. In addition, the utilization of a higher number of smaller electrodes to reduce the thickness of the diffusion layer has also been reported [279]. The use of glass-like carbon micro electrodes, fabricated with the C-MEMS technique, as glucose sensors is demonstrated in [128].

5.6.3 Energy

The world demand for energy is projected to more than double by 2050 and to more than triple by the end of the century [280]. In the portable energy arena, recent years have witnessed an explosion of demand for power-hungry portable electronics like laptop computers and mobile phones. As a direct consequence, the need for portable energy sources is expected to increase dramatically as the market continuously commands the integration of a multitude of functionalities and better data transfer capabilities into portable devices. Even when lithium-based technology is currently the alternative of choice, incremental improvements on existing technologies will not be adequate to supply this demand in a sustainable way. Lithium-ion battery technology requires significant breakthroughs in enhancing battery life and reliability to meet the increasing power demands of portable devices [281].

In the present scenario of a global quest toward a clean and sustainable energy future, fuel cells are perceived to play a key role owing to their high energy efficiency, theoretical energy density (higher than batteries), environmental friendliness and minimal noise. Fuel cells link hydrogen and electricity, two highly compatible energy carriers that embody the ideals of a sustainable energy economy: they are clean, abundant, and adapt flexibly to many sources of fuel production and to many end uses.

However, conventional fuel cells consist of structural components, including gaskets, fasteners and end plates that make the assembly complicated. These structural components act as impediments toward reducing the size of the fuel cells. Therefore, novel design and manufacturing approaches are required to realize component miniaturization and assembly simplification of fuel cells [282]. Recent studies [283–292] have suggested that, in order to comply with the electromechanical integration of the fuel cell structure with high precision, repeatability and productivity, micro electromechanical systems (MEMS) technology is the most attractive fabrication process. MEMS offer a better alternative for small fuel cells for mobile applications, compared to other conventional techniques like machining, molding and fastening. MEMS-based techniques are expected to enable simple and mass-producible fuel cells with uniform specifications, in the same way integrated circuits did it for the electronics industry some years ago [293]. MEMS technology is able to provide the following improvements in the fuel cell [294]: (1) significant reduction of precious (typically Pt) catalyst loading and higher power output due to the controlled microstructure of the three phase boundary for the electrochemical reaction; (2) lower contact resistance at the layer interface and controlled gas permeable structure due to electromechanically integrated fabrication; and (3) flexible connection design of multiple cells. In addition, by using bonding technologies employed in MEMS devices, such as anodic and eutectic bonding, the fuel cell components can be monolithically integrated. Localized bonding at a low temperature, along with a solid polymer electrolyte, could prove beneficial in minimizing the required bonding surface and maximizing the electrochemically active area available in the fuel cell [294]. As a result, components such as gaskets, fasteners and end plates could be eliminated. Furthermore, by integrating auxiliary devices on chip, including micro-pumps, valves, connectors and controllers, small fuel cell systems, or a power-plant-on-a-chip, with high power density could be realized. In addition to the required compactness, portable fuel cells must also feature low manufacturing costs to facilitate their commercial implementation [282, 295].

This section explores the use of microfabricated fuel cells as energy sources for mobile applications. Having introduced the motivation for portable, compact fuel cells, we now proceed to list some of the most important advantages of microfabricated fuel cells, the different types and means of integration. The section closes with an overview of micro PEM fuel cells and enzyme-based biofuel cells featuring carbon-based components.

In general, microfabricated fuel cells offer unique advantages [294, 296]:

(1) As a device is miniaturized, the surface-to-volume ratio of the entire device increases (typically, area scales with l^2 while volume scales with l^3). Thus, the surface-to-volume ratio, in general, scales with proportion to $l^2/l^3 = 1/l$. This has a direct implication in improved heat and mass transport phenomena present in a typical low-temperature polymer-electrolyte membrane-based fuel cell for portable power applications.

(2) Increased power density due to higher surface-to-volume ratio and improved energy density due to the use of liquid fuel and reduced balance of plant.

(3) Better control of fuel cell component fabrication and integration leading to increased catalyst utilization in the electrodes and reduced system complexity.

Among the different types of miniature fuel cells, direct liquid-feed methanol fuel cells (DMFCs) have received widespread acceptance as the potential power source of choice for portable devices, given its enhanced power and energy density. Comprehensive overviews of the progress and challenges in DMFCs are provided in recent reviews [297–304]. Other miniature fuel cell architectures include microfluidic fuel cells [305–308], air-breathing fuel cells [309–311] and biological fuel cells [312–316]. Inherent to these miniature fuel cell architectures is the development, adoption and deployment of suitable microfabrication techniques for component synthesis and compact system integration. The fabrication process also holds the key toward successful commercialization of the fuel cell technology for portable power devices. Effective miniaturization to build portable fuel cells is a challenging task.

There are currently two different approaches for the fabrication and integration of miniaturized fuel cells [293]. A first approach is to follow the design principles of larger fuel cells and stack several cells on top of each other. Vertical stacking is then used to connect the cells in series. In contrast, a second approach avoids the bipolar approach of conventional fuel cells and follows a monolithic, or monopolar, fuel cell design that leverages the surface machining aspect of microfabrication processes. Approaches such as the “flip-flop” interconnect method [289, 317] are used instead of vertical stacking to connect the cells in series. The current trend is toward monopolar planar designs [296]. For further details, the reader is referred to Meyers et al. [293] who compared bipolar and monolithic MEMS fuel cell designs based on silicon technology.

5.6.3.1 Polymer Electrolyte Membrane (PEM) Fuel Cells

The polymer electrolyte membrane (PEM) fuel cell is arguably the front runner among the different types of fuel cells and is poised to cater clean electrical energy to automotive, portable and stationary power devices. A typical PEM fuel cell, shown in Fig. 5.29, exhibits a layered architecture with a proton conducting polymer membrane, typically Nafion®, separating the anode and cathode compartments. The anode and cathode sides each comprises of gas channel, gas diffusion layer (GDL) and catalyst layer (CL). Hydrogen is the fuel in the H_2/air PEM fuel cells for automotive applications, while aqueous methanol is the fuel for direct methanol fuel cells (DMFC) for portable applications. Usually, two thin catalyst layers are coated on both sides of the membrane, forming a membrane-electrode assembly (MEA). Protons, electrons and oxygen combine electrochemically within the active catalyst layer to produce electricity, water and waste heat.

The conventional PEM fuel cell (H_2/air and DMFC) features components fabricated from primarily carbon-based materials for the underlying physico-electrochemical processes to occur. The state-of-the-art catalyst layer, with thickness $\sim$ 10–15 μm, in a PEM fuel cell is a three-phase composite, shown in a high

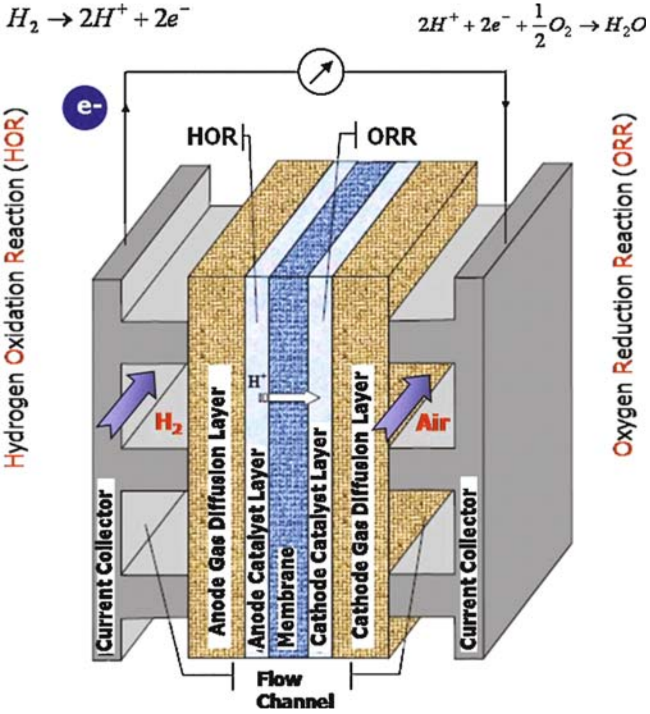

Fig. 5.29 Schematic diagram of a polymer electrolyte fuel cell

resolution transmission electron microscope (TEM) micrograph of an actual catalyst later in Fig. 5.30 [318], and consists of: (1) ionomer, i.e., the ionic phase which is typically Nafion® to provide a passage for protons to be transported in or out, (2) metal (Pt) catalysts supported on carbon, i.e., the electronic phase for electron conduction, and (3) pores for the oxygen gas to be transferred in and product water out. Gottesfeld and Zawodzinski [319], and more recently Eikerling and co-workers [320, 321], have provided good overviews of the catalyst layer structure and functions. Specific properties of the catalyst layer include high catalyst mass activity, high catalyst utilization at all current densities, low mass transport losses, high tolerance to multiple surface area loss mechanisms, tolerance of a wide humidity and temperature operating window, cold start and freeze tolerance, and the ability to be fabricated by robust high volume-compatible, low cost processes. Conventional carbon-supported finely-dispersed electrocatalysts rely on high surface area carbons (carbon blacks or graphitized carbon) for electrical conductivity and on 2–3 nm-sized catalyst particles on those carbon surfaces for high levels of catalyst activity. In an effort to reduce Pt catalyst loading and improve catalyst utilization, recent advances in catalyst layer development include the 3 M® nanostructured thin film (NSTF) catalyst which obviates the use of carbon and ionomer [322, 323]. Catalyst-coated organic nano-whiskers, as shown in Fig. 5.31 [323], form the thin catalyst

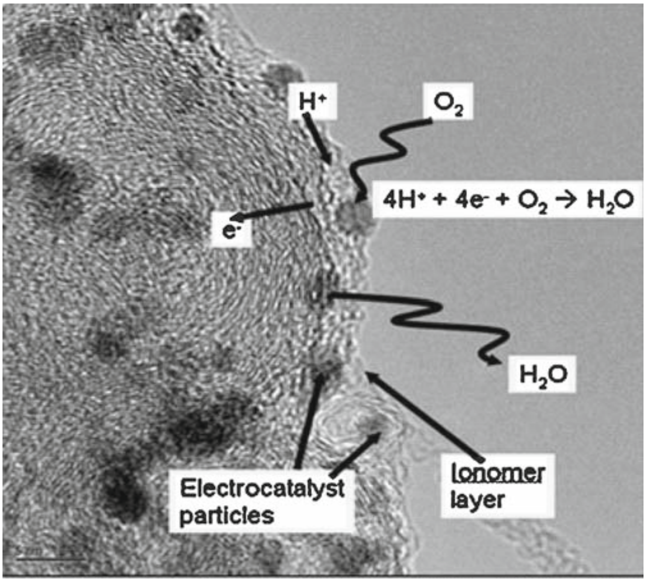

Fig. 5.30 High resolution TEM image of an actual PEM fuel cell catalyst layer illustrating the three-phase interface. Reprinted from [318] with permission from Karren L. More, Oak Ridge National Laboratory, TN, USA

layer ($\sim$ 1 μm) and the electrochemically active area is instead a two-phase interface for the electrochemical reaction to occur. The multi-faceted functionality of the gas diffusion layer includes reactant distribution, liquid water transport, electron transport, heat conduction and mechanical support to the MEA. Carbon-fiber-based porous materials, namely non-woven carbon paper and woven carbon cloth, have received wide acceptance as materials of choice for the PEM fuel cell GDL owing to their high porosity (~ 70% or higher) and good electrical/thermal conductivity. The thickness of typical GDL structures range between 200 and 300 μm. SEM micrographs along with 3D representative microstructures of typical non-woven carbon paper and woven carbon cloth GDL are shown in Fig. 5.32 [324]. Mathias et al. provided a comprehensive overview of GDL structure and functions in [325]. In order to facilitate removal of liquid water from GDL and avoid flooding, the GDL is treated with PTFE (polytetrafluoroethylene) with loading varying from 5–30 weight % in order to induce and/or enhance hydrophobicity [325]. The graphite bipolar plate houses the flow channels and consists of solid and porous plate architectures [326]. The bipolar plate properties include high electronic and thermal conductivities and sufficient mechanical/chemical stability. These carbon based components contribute to the effective water and thermal management, described as maintaining a delicate balance between oxygen and liquid water transport as well as heat dissipation in the fuel cell [327, 328].

The fabrication of micro- and nano-sized carbon components holds great potential in future PEM fuel cell components (e.g. gas diffusion layer, catalyst layer) with

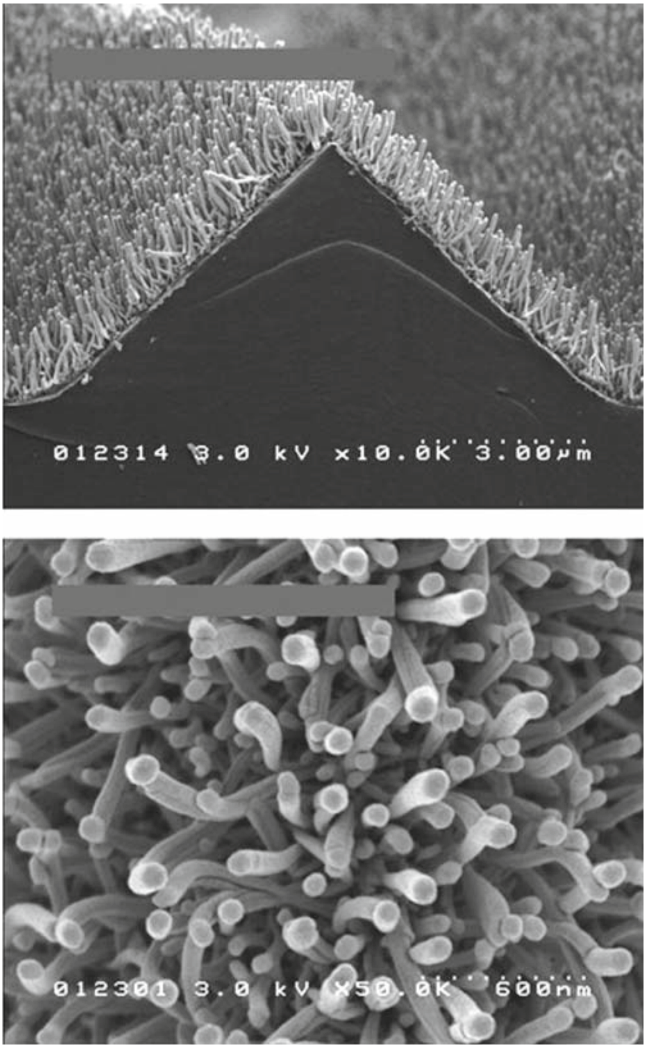

Fig. 5.31 Scanning electron micrographs of typical NSTF catalysts as fabricated on a microstructured catalyst transfer substrate, seen (*top*) in cross-section with original magnification of × 10,000, and (*bottom*) in plan view with original magnification of × 50,000. The dotted scalebar is shown in each micrograph. Reprinted from [323] with permission from Elsevier

improved water and thermal management characteristics. It is widely recognized that the performance degradation and the limiting current behavior in the PEM fuel cell are mainly attributed to the excessive build up of liquid water in the cathode side and the resulting flooding phenomena [327, 329, 330]. Liquid water blocks the open pore space in the CL and the GDL leading to hindered oxygen transport and covers the electrochemically active sites in the CL thereby rendering reduced

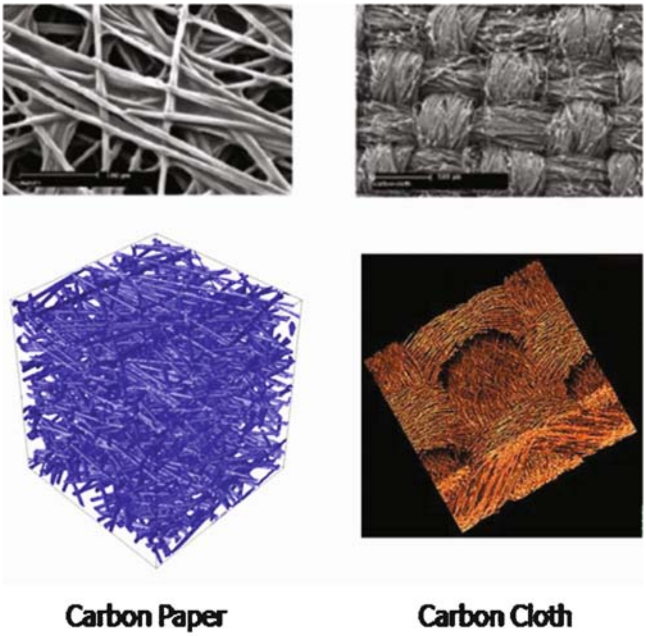

Fig. 5.32 SEM micrographs and representative 3D microstructures of carbon paper and carbon cloth GDL

catalytic activity. The catalyst layer and gas diffusion layer, therefore, play a crucial role in the water management [327] aimed at maintaining a delicate balance between reactant transport from the gas channels and water removal from the electrochemically active sites. In this regard, the capability of the CL as the primary component in the entire fuel cell assembly in generating heat and the impact of the thermal effects on liquid water accumulation and cell performance are of profound importance. Mukherjee and co-workers [324, 330, 331] have recently developed a theoretical framework to study the impact of the evaporative capability due to heat generation in the CL on the water and thermal management and cell performance. Based on a physical description of heat and water balance, they have defined “heat partition factor (β)” which corresponds to the fraction of the total heat generation rate actually available for the evaporation of liquid water in the CL. Considering the heat balance in the CL and GDL as well as the vapor diffusion through the GDL, the heat partition factor can be uniquely defined in terms of the GDL thermal conductivity and the saturation vapor concentration depending on the fuel cell operating temperature. The GDL thermal conductivity and the fuel cell operating temperature through its strong influence on the saturated vapor pressure exhibit profound influence on the heat partition factor which further dictates the net liquid water evaporation and hence the liquid water saturation distribution inside the CL. The variation of the heat partition factor with temperature is shown in Fig. 5.33 for

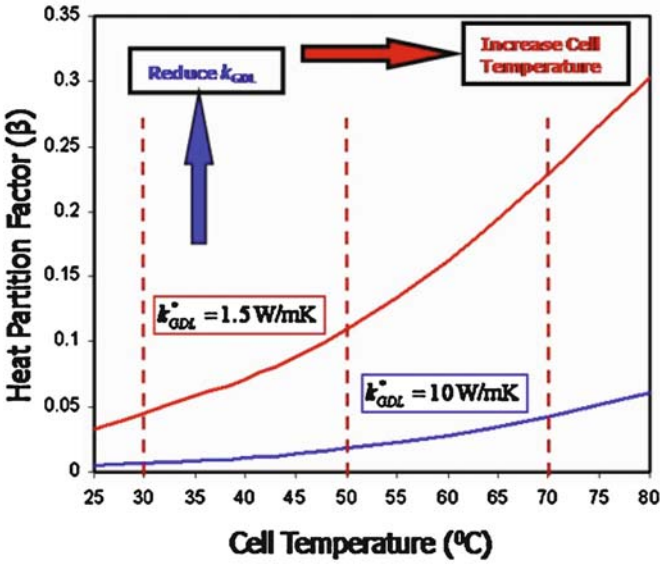

Fig. 5.33 Variation of the heat partition factor with fuel cell operating temperature for two different GDL thermal conductivity values

two different GDL thermal conductivity values. From the figure it can be observed that higher cell operating temperatures and low GDL thermal conductivities promote evaporation in the CL and hence will lower the liquid water saturation level leading to improved performance. The impact of GDL thermal conductivity and operating temperature on the average liquid water saturation level in the CL and electrode performance in terms of the polarization characteristics are shown in Fig. 5.34. The effective thermal conductivity value of 1.5 W/mK is representative of the typical carbon paper and carbon cloth GDL materials currently used in PEM fuel cells. It is evident from this analysis that a lower value of GDL thermal conductivity (e.g. between 0.5 and 1.0 W/mK), while maintaining a high electronic conductivity to avoid voltage loss due to electron transport resistance, would dramatically benefit fuel cell performance. This emphasizes the need for the development of GDL with novel microstructure and morphology, which will essentially act as a thermal insulator in the limiting sense and an electronic conductor.

The abundant use of carbon-based materials inherent to the conventional fuel cell design forms the base for exploiting current techniques for the micro and nanofabrication of carbon, like Carbon MEMS/NEMS (Carbon Micro-/Nano-ElectroMechanical Systems), in the development of component and system architecture for miniature PEM fuel cell systems.

Madou and co-workers [296, 329] have recently pioneered the C-MEMS technique for fabricating bipolar plates and demonstrated their integration in a miniature PEM fuel cell. The bipolar plate fabrication method and its integration into a single cell architecture is detailed in [296] and summarized below:

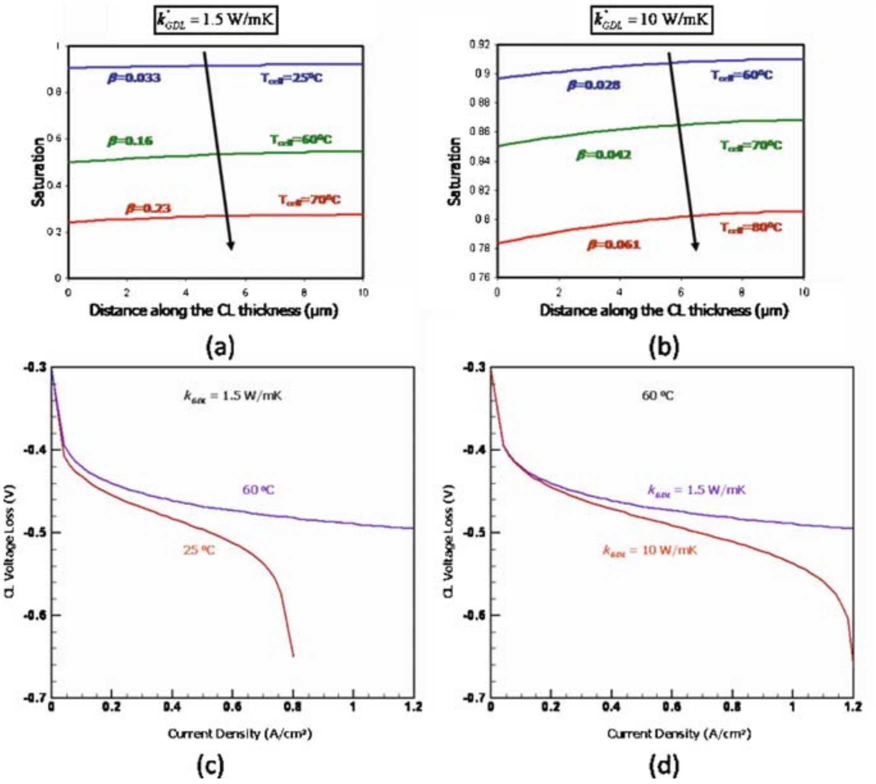

Fig. 5.34 (**a**) Liquid water saturation distributions along the CL thickness for different cell operating temperatures and with GDL thermal conductivity of 1.5 W/mK; (**b**) Liquid water saturation distributions along the CL thickness for different cell operating temperatures and with GDL thermal conductivity of 10 W/mK; (**c**) Effect of the cell operating temperature on the CL voltage loss prediction; (**d**) Effect of the GDL thermal conductivity on the CL voltage loss prediction

(1) Fluidic channel walls and separators are machined from thick polymer sheets and bonded together to create fluidic plates.
(2) The structures are converted into carbon by pyrolysis. A physical binder acts also as an electrical binder.
(3) Commercial fuel cell electrodes are combined with an activated Nafion® membrane to create a membrane electrode assembly (MEA).
(4) The MEA, fluidic plates, and gas inlet/outlets are brought and sealed together by epoxy.

Figure 5.35 shows the fluidic plate structures before carbonization and a three-layer carbon bipolar plate structure made by first bonding Cirlex® fluidic channel walls to a 5 mm Kapton® sheet and then converting the entire structure into carbon. The design and integration of a miniature PEM fuel cell stack using the C-MEMS

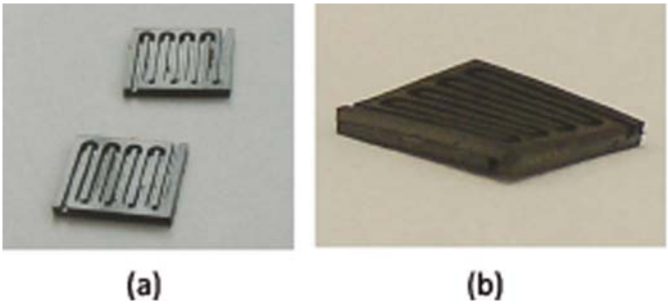

Fig. 5.35 (**a**) Fluidic plate structures before carbonization; (**b**) A three-layer carbon bipolar plate structure made by first bonding Cirlex® fluidic channel walls to a 5 mil Kapton® sheet then converting the entire structure into carbon. Reprinted from [296] with permission from Elsevier.

fabrication technique has also been successfully demonstrated by Madou and co-workers [329]. Figure 5.36 shows a three-cell PEM fuel cell stack configuration. The performance in terms of polarization (I-V curve) and power density characteristics of this microfabricated PEM fuel cell stack are shown in Fig. 5.37. The C-MEMS technique has also been successfully deployed for the development of a direct photosynthetic/metabolic micro bi-fuel cell with improved power capability by Moriuchi and co-workers [315] and is currently being used in the development of an enzyme-based bio fuel cell (detailed below). These recent developments in micro fuel cell component fabrication and system integration truly highlight the enormous

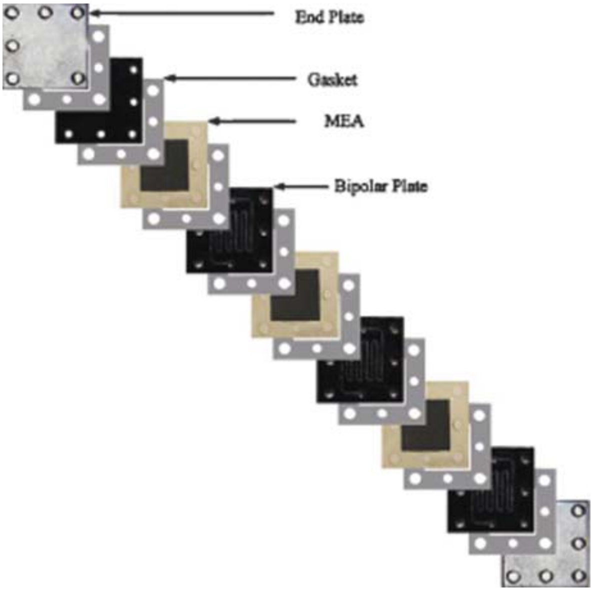

Fig. 5.36 Configuration of a three-cell fuel cell stack. Reprinted from [329] with permission from Elsevier.

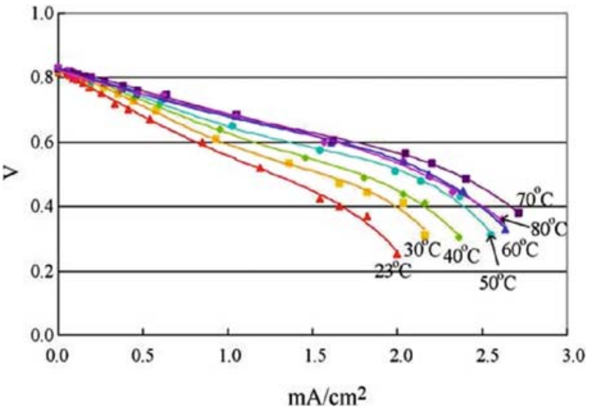

Fig. 5.37 Effect of operating temperature on the fuel cell polarization curve. Reprinted from [329] with permission from Elsevier

promise of the C-MEMS/NEMS techniques in the development of future portable power devices for clean electricity generation.

Concurrent to the success of C-MEMS/NEMS-based devices, it is worth discussing the promise and recent developments of carbon nanotube (CNT) based miniature PEM fuel cell component fabrication and MEMS integration toward improved power output. Kuriyama and co-workers have recently demonstrated the use of multi-walled carbon nanotubes (MWCNT) as a promising carbon material in micro/nano fuel cells. MWCNTs exhibit good electrical conductivity, gas permeability, catalyst support properties and most importantly, suitability for their integration into existent MEMS processes. The MWCNTs were employed for both the gas diffusion and catalyst layers, which were integrated as a single layer with intimate electromechanical contact. The key concept is the integrated anode/cathode configuration, which electromechanically integrates all the components including the flow channel, current collector, gas diffusion layer and catalyst layer. These are deposited and grown on the silicon wafer substrate that serves as the flow channel structure. In a conventional fuel cell, electromechanical contact between all components is controlled by applying external mechanical pressure. However, uniform pressure control in miniature fuel cells requires more complicated assembly and results in higher costs. In contrast, in this configuration all components are deposited and grown layer-by-layer with good electromechanical contact, which eliminates the need for pressurizing the components such as gaskets, fasteners and end plates. It also decreases cell resistance. The three-component micro fuel cell configuration with the polymeric membrane sandwiched between the integrated anode/cathode assembly is shown schematically in Fig. 5.38. The unique aspect of the fabrication process is that the silicon dioxide layer, which is serving as the foundation of MWCNTs growth, is also employed as a sacrificial layer to make the MWCNTs suspend by themselves over the circular holes of a MoSi current collector. Representative I-V and power density characteristics, as a measure for the

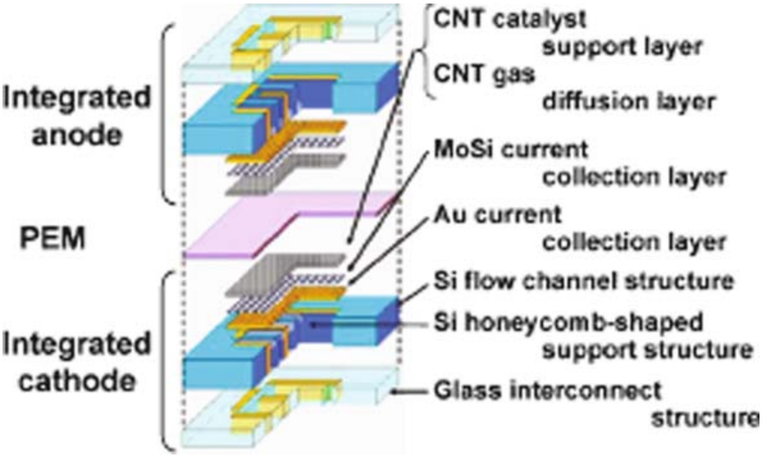

Fig. 5.38 Schematic design of MEMS-based three-component fuel cell. PEM is sandwiched by the integrated anode and cathode. The three components are assembled using a bonding technique without any fasteners. Reprinted from [294] with permission from Elsevier

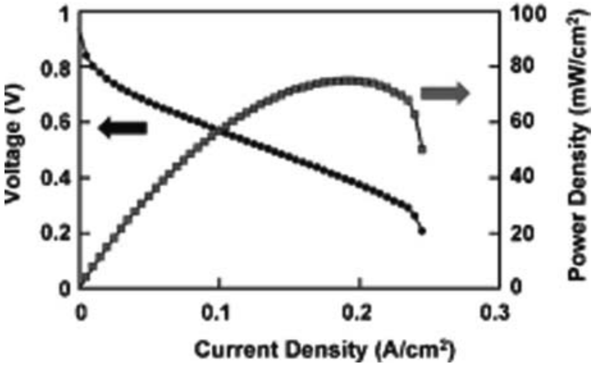

Fig. 5.39 *I–V* and power density characteristic curves of the prototype (active cell area: 1 cm^2; electrolyte: GORE-SELECT®, 30 μm thick; H2: 8.0 sccm; air: 8.0 sccm; no humidification and back-pressure) [294]. Reprinted from [294] with permission from Elsevier

fuel cell prototype performance, are shown in Fig. 5.39. The details of the fabrication process, fuel cell prototype integration, MWCNT characterization and cell performance are reported in [294].

Other recent developments in CNT based 3D architectures show promise in modifying the thermal and electronic properties. Prasher et al. [332] has recently demonstrated that a 3D fibrous bed with CNT arrays behaves as a thermal insulator with effective thermal conductivity as low as 0.2 W/mK while maintaining significantly high electronic conductivity. This further underscores the tremendous potential of C-MEMS/NEMS techniques [294, 296, 327] along with layer-by-layer 3D assembly of CNT based structures [333] in the fabrication of components and system integration toward dramatic improvement of micro fuel cells performance for powering emergent engineering devices.

5.6.3.2 Enzyme-Based Bio Fuel Cells

Basic enzymatic biofuel cells contain many of the same components as a hydrogen/oxygen fuel cell. However, rather than employing metallic electrocatalysts at the anode and the cathode, the electrocatalyst used are oxidoreductase enzymes. This is a class of enzymes that can catalyze oxidation–reduction reactions. Since these enzymes are selective electrocatalysts, the separator could be an electrolyte solution, gel, or polymer, or not be present at all.

The miniaturization of bio-fuel cells is mostly driven by its use in portable electronics and biomedical devices. These applications require continued energy supply and small dimensions, and both can be achieved using enzymatic bio-fuel cells. Even when the substrates used for the immobilization of enzymes are generally metals (mostly gold and platinum), carbon offers an excellent alternative given its favorable electrochemical properties. Furthermore, Carbon-MEMS technology represents a good option for the miniaturization of enzymatic bio-fuel cells because it is a relatively easy way to miniaturize carbon electrodes.

In order to miniaturize fuel cell components (mainly, the anode and the cathode), the main challenge is to reduce the size of the electrodes while keeping large current densities. Single carbon fiber fuel cells have been already demonstrated by Heller et al. [334]. This approach might be enough for applications that need very small amounts of power (sensors, transmitters, etc.), but in applications that need larger power and energy densities (body implants, power sources for electronic devices, etc.), the amount of enzyme immobilized in one single carbon fiber is not enough to power the entire device.

The Carbon-MEMS process brings several advantages when used as substrate material for the immobilization of enzymes in bio-fuel cell applications because:

1. It is possible to fabricate carbon electrodes with high surface area, which offers more immobilization sites per footprint. This increases the specific current substantially, due to the high local enzyme concentration.
2. Its surface presents a micro porous structures, with pore dimension small enough to trap the enzyme (size of the enzymes is about 80 Å) and big enough to let the electrolyte pass through. This also may lead to longer lifetime of the bio-fuel cell [335].
3. It is possible to fabricate bio-fuel cells with both cathode and anode on the same surface.
4. The integration of carbon nanotubes and carbon nanofibers with Carbon-MEMS could allow achieving direct electrical connection between enzyme and carbon electrode.
5. Fractal structures can be fabricated and integrated with Carbon-MEMS.

As pointed out above, one of the main advantages that Carbon-MEMS brings to the miniaturization of bio-fuel cells is the possibility for enhancing the total surface area of the electrodes by combining carbon nano-tubes and carbon nano-fibers with pre-existing three-dimensional microstructures. As it has been demonstrated by Calabrese-Barton et al. the addition of carbon nano-fibers to carbon cloth improves the total current density of the bio-fuel cell by one order of magnitude [336]. This combined top-down (lithography) and bottom-up (chemical vapor deposition) approach is bringing the possibility of creating enzyme-based bio-fuel cells into reality (see the section on fractal electrodes in the discussion about glucose sensors)

Even though the use of Carbon-MEMS represents a big advantage over current technologies, there are other big challenges to be overcome in order to make this approach a success. The most relevant one is to be able to covalently attach the enzyme to the Carbon-MEMS surface, respecting both angle and distance of the redox center from the carbon electrode. By achieving this, the obtained current will be higher than in the case of a multilayer of enzymes connected through a conducting wire (molecular wire) to the electrode surface. Although such achievement might not make much of a difference in a sensor configuration, it would represent a significant 50% improvement for an energy conversion device.

It is important to note that an extensive future research effort is warranted to develop suitable C-MEMS/NEMS based techniques in order to infuse transformational breakthroughs imperative to the success of the emerging electrochemical energy conversion systems which will ultimately pave the way toward securing a sustainable energy future.

References

1. Ferchault de Reaumur R (1722) L'art de convertir le fer forge en acier, et l′art d′adoucir le fer fondu, ou de faire des ouvrages de fer fondu aussi finis que le fer forge. Available from http://www.books.google.com.
2. Lavoisier A (1789) Traite Elementaire de Chimie. Available from http://gallica.bnf.fr/.
3. Shevlin PB (1972) Formation of atomic carbon in the decomposition of 5-tetrazolyldiazonium chloride. J. Am. Chem. Soc. 94:1379–1380.
4. Dewar MJS, Nelson DJ, Shevlin PB, and Biesiada KA (1981) Experimental and theoretical investigation of the mechanism of deoxygenation of carbonyl compounds by atomic carbon. J. Am. Chem. Soc. 103:2802–2807.
5. Sladkov AM, Kasatochkin VI, Kudryavstev YP, and Korshak VV (1968) Synthesis and properties of valuable polymers of carbon. Russ. Chem. Bull. 17:2560–2566.
6. Sergushin IP, Kudryavstev YP, Elizen VM et al. (1977) X-ray Electron and X-ray spectral study of Carbyne. J. Struct. Chem. 18:698–700.
7. Whittaker AG (1978) Carbon: A new view of its high-temperature behavior. Science. 200:763–764.
8. Smith PPK and Buseck PR (1982) Carbyne forms of carbon: Do they exist? Science 216:984–986.
9. Whittaker AG (1985) Carbyne forms of carbon: Evidence for their existence. Science 229:485–486.
10. Lagow RJ, Kampa JJ, Wei H et al. (1995) Synthesis of linear acetylenic carbon: The "sp" carbon allotrope. Science 267:362–367.

11. Baughman RH (2006) Chemistry: Dangerously seeking linear carbon. Science. 312:1009–1010.
12. Frondel C and Martin UB (1967) Lonsdaleite, a Hexagonal polymorph of diamond. Nature. 214:587–589.
13. Bundy FP and Kasper JS (1967) Hexagonal diamond – a new form of carbon. J. Chem. Phys. 46:3437–3446.
14. Kroto HW, Heath JR, O′Brien SC, Curl RF, and Smalley RE (1985) C60: Buckminsterfullerene. Nature. 318:162–163.
15. Novoselov KS, Geim AK, Morozov SV et al. (2004) Electric field effect in atomically thin carbon films. Science. 306:666–669.
16. Meyer JC, Geim AK, Katsnelson MI, Novoselov KS, Booth TJ, and Roth S (2007) The structrue of suspended graphene sheets. Nature. 446:60–63.
17. Geim AK and Kim P (2008) Carbon wonderland. Scientific American. 298:68–75.
18. Rode AV, Gamalay EG, and Luther-Davies B (2000) Formation of cluster-assembled carbon nano-foam by high repetition-rate laser ablation. Appl. Phys. A. 70: 135–144.
19. Rode AV, Gamalay E, and Luther-Davies B (2002) Electronic and Magnetic properties of carbon nanofoam produced by high-repetition-rate laser ablation. Appl. Surf. Sci. 197:644–649.
20. Rode AV, Gamalay E, Christy AG et al. (2004) Unconventional magnetism in all-carbon nanofoam. Phys. Rev. B. 70:054407-1-054407-9.
21. Rode AV, Gamalay E, Christy AG et al. (2005) Strong paramagnetism and possible ferromagnetis in pure carbon nanofoam produced by laser ablation. J. Magn. Magn. Mater. 290–291:298–301.
22. Sullivan JP, Friedmann TA, and Hjort K (2001) Diamond and amorphous carbon MEMS. MRS Bulletin. April:309–311.
23. Robertson J (2002) Diamond-like amorphous carbon. Mat. Sci. Eng. R. 37:129–281.
24. Hauser JJ (1977) Electrical, structural and optical properties of amorphous carbon. J. Non-Cryst. Solids. 23:21–41.
25. Andersson L (1981) A review of recent work on hard i-C films. Thin Solid Films. 86:193–200.
26. Robertson J (1986) Amorphous carbon. Adv. Phys. 35:317–375.
27. Robertson J (1991) Hard amorphous (diamond-like) carbons. Prog. Solid State Chem. 21:199–333.
28. Fitzer E, Kochling KH, Boehm HP, and Marsh H (1995) Recommended terminology for the description of carbon as a solid. Pure Appl. Chem. 67:473–506.
29. Anderson PW (1958) Abscence of diffusion in certain random lattices. Phys. Rev. 109:1492–1505.
30. Dobbs HS (1974) Vitreous Carbon and the brittle fracture of amorphous solids. J. Phys. D: Appl. Phys. 7:24–34.
31. Bragg RH and Hammond ML (1965) X-ray study of pyrolytic graphites and glassy carbons. Carbon. 3:340–340.
32. Rothwell WS (1968) Small-angle x-ray scattering from glassy carbon. J. Appl. Phys. 39:1840–1845.
33. McFeely SP, Kowalczyk SP, Ley L, Cavell RG, Pollak RA, and Shirley DA (1974) X-ray photoemission studies of diamond, graphite, and glassy carbon valence bands. Phys. Rev. B. 9:5268–5278.
34. Nishikawa K, Fukuyama K, and Nishizawa T (1998) Structure change of glass-like carbon with heat treatment, studied by small angle x-ray scattering: i. glass-like carbon prepared from phenolic resin. Jpn. J. Appl. Phys. 37:6486–6491.
35. Fukuyama K, Nishizawa T, and Nishikawa K (2001) Investigation of the pore structure in glass-like carbon prepared from furan resin. Carbon. 39:2017–2021.

36. Iwashita N, Park CR, Fujimoto H, Shiraishi M, and Inagaki M (2004) Specification for a standard procedure of X-ray diffraction measurements on carbon materials. Carbon. 42: 701–714.
37. Dekanski A, Stevanovic J, Stevanovic R, Nikolic BZ, and Jovanovic VM (2001) Glassy carbon electrodes: I. Characterization and electrochemical activation. Carbon 39:1195–1205.
38. Oberlin A and Oberlin M (1983) Graphitizability of carbonaceous materials as studied by TEM and X-ray diffraction. J. Microsc. 132:353–363.
39. Yamada S and Sato H (1962) Some physical properties of glassy carbon. Nature 193:261–262.
40. Lewis JC, Redfern B, and Cowlard FC (1963) Vitreous carbon as a crucible material for semiconductors. Sol. State Electron. 6:251–254.
41. Cowlard FC and Lewis JC (1967) Vitreous carbon – a new form of carbon. J. Mater. Sci. 2:507–512.
42. Cahn W and Harris B (1969) Newer forms of carbon and their uses. Nature. 221:132–141.
43. Halpin MK and Jenkins GM (1969) Interaction of glassy carbon with alkali metal vapours. Proc. R. Soc. Lond. A. 313:421–431.
44. Jenkins GM and Kawamura K (1976) Polymeric Carbon – Carbon Fibre, Glass and Char. Cambridge University Press, London, New York.
45. Wang C, Jia G, Taherabadi LH, and Madou MJ (2005) A novel method for the fabrication of high-aspect ratio C-MEMS structures. J. MEMS. 14:348–358.
46. Jenkins GM, Kawamura K, and Ban LL (1972) Formation and structure of polymeric carbons. Proc. R. Soc. Lond. A. 327:501–517.
47. Kakinoki J (1965) A model for the structure of "glassy carbon". Acta. Cryst. 18:578.
48. Jenkins GM and Kawamura K (1971) Structure of glassy carbon. Nature. 231:175–176.
49. Pesin LA (2002) Structure and Properties of glass-like carbon. J. Mater. Sci. 37:1–28.
50. Shiraishi M (1984) Kaitei Tansozairyo Nyumon (Introduction to Carbon Materials). Tanso Zairyo Gakkai 29–33.
51. Fedorov VB, Shorshorov MK, and Khakimova DK (1978) Carbon and its interaction with metals [in Russian]. Metallurgiya, Moscow:119–129.
52. Pesin LA and Baitinger EM (2002) A new structural model of glass-like carbon. Carbon. 40:295–306.
53. Yoshida A, Kaburagi Y, and Hishiyama Y (1991) Microtexture and magnetoresistance of glass-like carbons. Carbon. 29:1107–1111.
54. Fitzer E, Schaefer W, and Yamada S (1969) The formation of glasslike carbon by pyrolysis of polyfurfuryl alcohol and phenolic resin. Carbon. 7:643.
55. Vohler O, Reiser P, Martina R, and Ovrehoff D (1970) New forms of Carbon. Angew. Chem. Int. Ed. Engl. 9:414–425.
56. Kawamura K and Kimura S (1983) Glass-like carbon made from epoxy resin cured with 2, 4, 6-Trinitrophenol. Bull. Chem. Soc. Jpn. 56:2499–2503.
57. Aggarwal RK, Bhatia G, Bahl OP, and Malik M (1988) Development of glass-like carbon from phenol formaldehyde resins employing monohydric and dihydric phenols. J. Mater. Sci. 23:1677–1684.
58. Callstrom MR, Neenan TX, McCreery RL, and Alsmeyer DC (1990) Doped glassy carbon materials (DGC): low-temperature synthesis, structure, and catalytic behavior. J. Am. Chem. Soc. 112:4954–4956.
59. Neenan TX, Callstrom MR, Bachman BJ, McCreery RL, and Alsmeyer DC (1990) Doped glassy carbon materials (DGC): Their synthesis from polymeric precursors and investigation of their properties. Br. Polym. J. 23:171–177.
60. Hutton HD, Huang W, Alsmeyer DC et al. (1993) Synthesis, characterization, and electrochemical activity of halogen-doped glassy carbon. Chem. Mater. 5:1110–1117.
61. Schueller OJA, Brittain ST, and Whitesides GM (1997) Fabrication of glassy carbon microstructures by pyrolysis of microfabricated polymeric precursors. Adv. Mater. 9: 477–480.

62. Shah HV, Brittain ST, Huang Q, Hwu S-, Whitesides GM, and Smith DW (1999) Bis-o-diynylarene (BODA) Derived polynaphthalenes as precursors to glassy carbon microstructures. Chem. Mater. 11:2623–2625.
63. Hishiyama Y, Igarashi K, Kanaoka I et al. (1997) Graphitization behavior of Kapton-derived carbon film related to structure, microtexture and transport properties. Carbon. 35: 657–668.
64. Kim J, Song X, Kinoshita K, Madou M, and White R (1998) Electrochemical studies of carbon films from pyrolyzed photoresist. J. Electrochem. Soc. 145:2314–2319.
65. Ranganathan S, McCreery RL, Majji SM, and Madou M (2000) Photoresist-derived carbon for microelectromechanical systems and electrochemical applications. J. Electrochem. Soc. 147:277–282.
66. Singh A, Jayaram J, Madou M, and Akbar S (2002) Pyrolysis of negative photoresists to fabricate carbon structures for microelectromechanical systems and electrochemical applications. J. Electrochem. Soc. 149:E78–E83.
67. Malladi K, Wang C, and Madou M (2006) Fabrication of suspended carbon microstructures by e-beam writer and pyrolysis. Carbon. 44:2602–2607.
68. Lee L (1965) Mechanisms of thermal degradation of phenolic condensation polymers. II. Thermal stability and degradation schemes of epoxy resins. J. Polym. Sci: Part A. 3: 859–882.
69. Fitzer E and Schafer W (1970) The effect of crosslinking on the formation of glasslike carbons from thermosetting resins. Carbon. 8:353–364.
70. Gac NA, Spokes GN, and Benson SW (1970) Thermal degradation of nadic methyl anhydride-cured epoxy novolac. J Polym Sci A. 8:593–608.
71. Jenkins GM, Kawamura K, and Ban LL (1972) Formation and structure of polymeric carbons. Proc. R. Soc. Lon. A. 327:501–517.
72. Lyons AM, Wilkins CW, and Robbins M (1983) Thin pinhole-free Carbon films. Thin Solid Films. 103:333–341.
73. Nakagawa H and Tsuge S (1987) Studies on thermal degradation of epoxy resins by high-resolution pyrolysis-gas chromatography. J. Anal. Appl. Pyrolysis. 12:97–113.
74. Chen KS and Yeh RZ (1996) Pyrolysis kinetics of epoxy resin in a nitrogen atmosphere. J. Hazard. Mater. 49:105–113.
75. Beyler CL and Hirschler MM (2002) Thermal decomposition of polymers. In: SFPE Handbook of Fire Protection Engineering.
76. Ma CM, Chen C, Kuan H, and Chang W (2004) Processability, Thermal, Mechanical, and Morphological Properties of Novolac Type-Epoxy Resin-Based Carbon-Carbon Composite. J. Comp. Mater. 38:311–322.
77. Mehrotra BN, Bragg RH, and Rao AS (1983) Effect of heat treatment temperature (HTT) on density, weight and volume of glass-like carbon (GC). J. Mater. Sci. 18:2671–2678.
78. Spain IL (1981) The electronic transport properties of graphite, carbons, and related materials. In: Walker Jr. PL and Thrower PA (eds) Chemistry and Physics of Carbon, Marcel Dekker, Inc., New York.
79. Pocard NL, Alsmeyer DC, McCreery RL, Neenan TX, and Callstrom MR (1992) Doped glassy carbon: A new material for electrocatalysis. J. Mater. Chem. 2:771–784.
80. Weintraub E and Miller LB (1915) Microphone. 1156509.
81. Davidson HW (1962) The properties of G. E. C. impermeable carbon. Nucl. Eng. 7:159–161.
82. Redfern B and Greens N (1963) Bodies and Shapes of Carbonaceous Materials and Processes for their Production. US 3109712.
83. Kotlensky WV and Martens HE (1965) Tensile properties of glassy carbon to 2,900 C. Nature. 206:1246–1247.
84. Zittel HE and Miller FJ (1965) A Glassy-carbon electrode for voltammetry. Anal. Chem. 37:200–203.
85. Lewis JB, Murdoch R, and Moul AN (1969) Heat of combustion of vitreous carbon. Nature. 221:1137–1138.

86. Benson J (1969) Carbon offers advantages as implant material in human body. NASA Technical Brief.
87. Benson J (1971) Elemental carbon as a biomaterial. J. Biomed. Mater. Res. 5:41–47.
88. Von Fraunhofer JA, L′estrange PR, and Mack AO (1971) Materials science in dental implantation and a promising new material: vitreous carbon. Biomed. Eng. 6:114–118.
89. Hucke EE, Fuys RA, and Craig RG (1973) Glassy Carbon: a potential Dental Implant Material. J. Biomed. Mater. Res. 7:263–274.
90. Stanitski CL and Mooney V (1973) Osseus attachment to vitreous carbons. J. Biomed. Mater. Res. 7:97–108.
91. Hobkirk JA (1976) Tissue reactions to implanted vitreous carbon and high purity sintered alumina. J. Oral. Rehabil. 4:355–368.
92. Haubold A (1977) Carbon in prosthetics. Annals of the New York Academy of Sciences. 283:383–395.
93. Maropis PS, Molinari JA, Appel BN, and Baumhammers A (1977) Comparative study of vitreous carbon, pyrolytic carbon, pyrolytic graphite/silicon-carbide, and titanium implants in rabbit mandibules. Oral Surg. Oral Med. Oral Pathol. 43:506–512.
94. Sherman AJ (1978) Bone reaction to orthodontic forces on vitreous carbon dental implants. Am. J. Orthod. 74:79–87.
95. Jenkins GM and Grigson CJ (1979) The fabrication of artifacts out of glassy carbon and carbon-fiber-reinforced carbon for biomedical applications. J. Biomed. Mater. Res. 13: 371–394.
96. Williams MW (1972) Optical properties of glassy carbon from 0 to 82 eV. J. Appl. Phys. 43:3460–3463.
97. Taylor RJ and Humffray AA (1973) Electrochemical studies on glassy carbon electrodes I. Electron-transfer kinetics. J. Electroanal. Chem. 42:347–354.
98. Nathan MI, Smith JE, and Tu KN (1974) Raman spectra of glassy carbon. J. Appl. Phys. 45:2370–2370.
99. Blaedel WJ and Jenkins RA (1974) Steady-state voltammetry at glassy carbon electrodes. Anal. Chem. 46:1952–1955.
100. Taylor RJ and Humffray AA (1975) Electrochemical studies on glassy carbon electrodes II. Oxygen reduction in solutions of high pH. J. Electroanal. Chem. 64:63–84.
101. Norvell VE and Mamantov G (1977) Optically transparent vitreous carbon electrode. Anal. Chem. 49:1470–1472.
102. Shigemitsu T and Matsumoto G (1979) Electrical Properties of glassy-carbon Electrodes. Med. Biol. Eng. Comput. 17:470.
103. Bourdillon C, Bourgeois JP, and Thomas D (1980) Covalent Linkage of glucose oxidase on modified glassy carbon electrodes. Kinetic phenomena. J. Am. Chem. Soc. 102:4231–4235.
104. Van der Linden, WE and Dieker JW (1980) Glassy carbon as electrode material for electro analytical chemistry. Anal. Chim. Acta. 119:1–24.
105. Hebert NE, Snyder B, McCreery RL, Kuhr WG, and Brazil SA (2003) Performance of pyrolyzed photoresist carbon films in a microchip capillary electrophoresis device with sinusoidal voltammetric detection. Anal. Chem. 75:4265–4271.
106. McCreery RL (1991) Carbon electrodes: structural effects on electron transfer kinetics. In: Bard AJ (ed) Electroanalytical Chemistry, Marcel Dekker, New York.
107. Kinoshita K (1988) Carbon, Electrochemical and Physicochemical Properties. Wiley-Interscience, New York.
108. Fitzer E, Mueller K, and Schaefer W (1971) The chemistry of the pyrolytic conversion of organic compounds to carbon. In: Walker Jr. PL (ed) Chemistry and Physics of Carbon, Marcel Dekker, Inc., New York.
109. Oberlin A (1989) High-Resolution TEM studies of carbonization and graphitization. In: Thrower PA (ed) Chemistry and Physics of Carbon, Marcel Dekker, Inc., New York.
110. Wang J (1981) Reticulated vitreous carbon – a new versatile electrode material. Electrochim. Acta. 26:1721–1726.

111. Friedrich JM, Ponce-de-Leon C, Reade GW, and Walsh FC (2004) Reticulated vitreous carbon as an electrode material. J. Electroanal. Chem. 561:203–217.
112. Schueller OJA, Brittain ST, Marzolin C, and Whitesides GM (1997) Fabrication and Characterization of Glassy Carbon MEMS. Chem. Mater. 9:1399–1406.
113. Schueller OJA, Brittain ST, and Whitesides GM (1999) Fabrication of glassy carbon microstructures by soft lithography. Sens. Actuators A: Phys. 72:125–139.
114. Schueller OJA, Brittain S, and Whitesides GM (2000) Fabrication of Carbon Microstructures.6143412.
115. Zhao X, Xia Y, Schueller OJA, Qin D, and Whitesides GM (1998) Fabrication of microstructures using shrinkable polystyrene films. Sens. Actuators A: Phys. 65:209–217.
116. Kostecki R, Song X, and Kinoshita K (2000) Influence of geometry on the electrochemical response of carbon interdigitated microelectrodes. J. Electrochem. Soc. 147:1878–1881.
117. Ranganathan S and McCreery RL (2001) Electroanalytical performance of carbon films with near-atomics flatness. Anal. Chem. 73:893–900.
118. Lorenz H, Despont M, Fahrni M, LaBianca N, Vettiger P, and Renaud P (1997) SU-8: a low-cost negative resist for MEMS. J. Micromech. Microeng. 7:121.
119. Shaw JM, Gelorme JD, LaBianca NC, Conley WE, and Holmes SJ (1997) Negative photoresists for optical lithography. IBM J. Res. Dev. 41:81–94.
120. Wang C and Madou M (2005) From MEMS to NEMS with carbon. Biosens. Bioelectron. 20:2181–2187.
121. Park BY, Taherabadi L, Wang C, Zoval J, and Madou MJ (2005) Electrical properties and shrinkage of carbonized photoresist films and the implications for carbon microelectromechanical systems devices in conductive media. J. Electrochem. Soc. 152:J136–J143.
122. Wang C, Taherabadi L, Jia G, Madou M, Yeh Y, and Dunn B (2004) C-MEMS for the manufacture of 3D microbatteries. Electrochem. Solid-State Lett. 7:A435–A438.
123. Galobardes F, Wang C, and Madou M (2006) Investigation on the solid electrolyte interface formed on pyrolyzed photoresist carbon anodes for C-MEMS lithium-ion batteries. Diam. Relat. Mater. 15:1930–1934.
124. Min H, Park BY, Taherabadi L et al. (2008) Fabrication and properties of a carbon/polypyrrole three-dimensional microbattery. J. Power Sources. 178:795–800.
125. Teixidor GT, Zaouk RB, Park BY, and Madou MJ (2008) Fabrication and characterization of three-dimensional carbon electrodes for lithium-ion batteries. J. Power Sources. 183: 730–740.
126. Park BY and Madou MJ (2006) Design, fabrication, and initial testing of a miniature PEM fuel cell with micro-scale pyrolyzed carbon fluidic plates. J. Power Sources. 162:369–379.
127. Lin P, Park BY, and Madou MJ (2008) Development and characterization of a miniature PEM fuel cell stack with carbon bipolar plates. J. Power Sources. 176:207–214.
128. Xu H, Malladi K, Wang C, Kulinsky L, Song M, and Madou M (2008) Carbon post-microarrays for glucose sensors. Biosens. Bioelectron. 23:1637–1644.
129. Turon Teixidor G, Gorkin III RA, Tripathi PP et al. (2008) Carbon microelectromechanical systems as a substratum for cell growth. Biomed. Mater. 3:034116.
130. Park BY and Madou MJ (2005) 3-D electrode designs for flow-through dielectrophoretic systems. Electrophoresis. 26:3745–3757.
131. Martinez-Duarte R, Rouabah HA, Green NG, Madou M, and Morgan H (2007) Higher Efficiency and Throughput in Particle Separation with 3D Dielectrophoresis with C-MEMS. Proceedings of uTAS 2007: Paris, France, October 7–11 1:826–828.
132. Martinez-Duarte R, Andrade-Roman J, Martinez SO, and Madou MJ (2008) A High Throughput Multi-stage, Multi-frequency Filter and Separation Device based on Carbon Dielectrophoresis. Proceedings of NSTI Nanotech 2008: Boston, MA, June 1–5 3: 316–319.
133. Martinez-Duarte R, Cito S, Collado-Arredondo E, Martinez SO, and Madou M (2008) Fluido-dynamic and Electromagnetic Characterization of 3D Carbon Dielectrophoresis with Finite Element Analysis. Proceedings of NSTI Nanotech 2008: Boston, MA, 3:265–268.

134. Martinez-Duarte R, Cito S, Collado-Arredondo E, Martinez SO, and Madou MJ (2008) Fluido-dynamic and electromagnetic characterization of 3D carbon dielectrophoresis with finite element analysis. Sens. Transd. J. 3:25–36.
135. Martinez-Duarte R, Gorkin R, Abi-Samra K, and Madou MJ (2009) The integration of 3D carbon dielectrophoresis on a rotating platform. Proc. Transd. 2009: Denver, CO, June 21–25: 2147–2150.
136. Madou MJ, Park BY, and Paradiso AC (2006) Method and Apparatus for Dielectrophoretic Separation.US 2006/0260944A1.
137. Park BY, Zaouk R, and Madou M (2004) Validation of lithography based on the controlled movement of light-emitting particles. Proc. Soc. Photo Opt. Instrum. Eng. 5374:566–578.
138. Martinez-Duarte R, Madou MJ, Kumar G, and Schroers J (2009) A Novel Method for Amorphous Metal Micromolding using Carbon MEMS. Proc. Transd. 2009.: June 21–25: 188–191.
139. Park BY, Zaouk R, Wang C, and Madou MJ (2007) A case for fractal electrodes in electrochemical applications. J. Electrochem. Soc. 154:P1–P5.
140. Sharma CS, Kulkarni MM, Sharma A, and Madou M (2009) Synthesis of carbon xerogel particles and fractal-like structures. Chem. Eng. Sci. 64:1536–1543.
141. Jeong OC and Konishi S (2008) Three-dimensionally combined carbonized polymer sensor and heater. Sens. Actuators. A. 143:97–105.
142 oleman JN, Khan U, Blau WJ, and Gun'ko YK (2006) Small but strong: A review of the mechanical properties of carbon nanotube–polymer composites. Carbon. 44: 1624–1652.
143. Hafner JH, Bronikowski MJ, Azamian BR et al. (1998) Catalytic growth of single-wall carbon nanotubes from metal particles. Chem. Phys. Lett. 296:195–202.
144. Madou MJ (2009) Manufacturing Techniques for Microfabrication and Nanotechnology. CRC Press, Boca Raton, FL.
145. Metz TE, Savage RN, and Simmons HO (1992) In Situ Control of Photoresist Coating Processes. Semicond. Int. 15:68–69.
146. Thompson LF (1994) An introduction to lithography. In: Thompson LF, Willson CG, and Bowden MJ (eds) Introduction to Microlithography, 2nd edn. American Chemical Society, Washington, DC.
147. Webster RJ (1998) Thin film polymer dielectrics for high-voltage applications under severe environments. Master of Science in Electrical Engineering, Virginia Polytechnic Institute and State University.
148. Chilton JA and Goosey MT (1995) Special Polymers for Electronics and Optoelectronics, Chapman and Hall, London, 351.
149. Madou M and Florkey J (2000) From Batch to Continuous Manufacturing of Microbiomedical Devices. Chem. Rev. 100:2679–2691.
150. Reichmanis R, Nalamasu O, Houlihan FM, and Novembre AE (1999) Radiation chemistry of polymeric materials. Polym. Int. 48:1053–1059.
151. Shaw JM, Gelorme JD, LaBianca NC, Conley WE, and Holmes SJ (1996) Negative photoresists for optical lithography. IBM J. Res. Dev. 41:81–94.
152. Ito H (1996) Chemical amplification resists: History and development within IBM. IBM J. Res. Dev. 41:69–80.
153. Gelorme JD, Cox RJ, and Gutierrez SAR (1989) Photoresist Composition and Printed Circuit Boards and Packages made therewith. 4882245.
154. Angelo R, Gelorme J, Kucynski J, Lawrence W, Pappas S, and Simpson L (1992) Photocurable epoxy composition with sulfonium salt photoinitiator.5102772.
155. Harris TW (1976) Chemical Milling. Clarendon Press, Oxford.
156. Reznikova EF, Mohr J, and Hein H (2005) Deep Photo-Lithography Characterization of SU-8 Resist Layers. Microsys. Tech. 11:282–291.
157. Lee SJ, Shi W, Maciel P, and Cha SW (2003) IEEE University/Government/Industry Microelectronics Symposium. Boise, ID, 389–390.

158. Bertsch A, Lorenz H, and Renaud P (1999) 3D Microfabrication by Combining Microstereolithography and Thick Resist UV Lithography. Sens. Act. A. 73:14–23.
159. Yang R and Wang W (2005) A numerical and experimental study on gap compensation and wavelength selection in UV-Lithography of Ultra-High Aspect Ratio SU-8 Microstructures. Sens. Act B. 110:279–288.
160. del Campo A and Greiner C (2007) SU:8 a photoresist for high-aspect-ratio and 3D submicron lithography. J. Micromech. Microeng. 17:R81–R95.
161. Wolf S and Tauber RN (2000) Silicon Processing for the VLSI Era. Lattice Press, Sunset Beach.
162. Arnone C (1992) The laser-plotter: A versatile lithographic tool for integrated optics and microelectronics. Microelectron. Eng. 17:483–486.
163. Duffy DC, McDonald JC, Schueller OJA, and Whitesides GM (1998) Rapid prototyping of microfluidic systems in poly(dimethylsiloxane). Anal. Chem. 70:4974–4984.
164. Sure A, Dillon T, Murakowski J, Lin C, Pustai D, and Prather DW (2003) Fabrication and characterization of three-dimensional silicon tapers. Optics Express. 11:3555–3561.
165. Windt DL and Cirelli RA (1999) Amorphous carbon films for use as both variable-transmission apertures and attenuated phase shift masks for deep ultraviolet lithography. J. Vac. Sci. Technol. B17:930–932.
166. Stauffer JM, Oppliger Y, Regnault P, Baraldi L, and Gale MT (1992) Electron beam writing of continuous resist profiles for optical applications. J. Vac. Sci. Technol. B10:2526.
167. Le Barny P (1987) In: Stroeve P and Franses E (eds) Molecular Engineering of Ultrathin Polymeric Films, Elsevier, New York.
168. Moreau WM (1987) Semiconductor Lithography: Principles, Practices and Materials. Springer, New York.
169. Cataldo A (1999) IBM Uses X-Ray Lithography to Build Prototypes. Semiconductor Business News.
170. Ehrfeld W and Schmidt A (1998) Recent Developments in Deep X-Ray Lithography. J. Vac. Sci. Technol. B16:3526–3534.
171. Rosolen GC (1999) Automatically aligned electron beam lithography on the nanometer scale. Appl. Surf. Sci. 144–145:467–471.
172. Skjolding LHD, Teixidor GT, Emnéus J, and Montelius L Negative UV–NIL (NUV–NIL) – A mix-and-match NIL and UV strategy for realisation of nano- and micrometre structures. Microelectronic Engineering. 86:654–656.
173. Editorial (1991) Ion Beam Focused to 8-nm Width. Res. Dev. September:23.
174. Sanchez JL, van Kan JA, Osipowicz T, Springham SV, and Watt F (1998) A high resolution beam scanning system for deep ion beam lithography. Nucl. Instr. Meth. Phys. Res. B136–B38:385–389.
175. van Kan JA, Sanchez JL, Xu B, Osipowicz T, and Watt F (1999) Micromachining using focused high energy ion beams: Deep ion beam lithography. Nucl. Instr. Meth. Phys. Res. B148:1085–1098.
176. Seliger RL, Ward JW, Wang V, and Kubena RL (1979) A high intensity scanning ion probe with submicrometer spot size. Appl. Phys. Lett. 34:310–312.
177. Brodie I and Muray JJ (1982) The Physics of Microfabrication. Plenum Press, New York.
178. Youn SW, Takahashi M, Goro H, and Maeda R (2006) A study on focused ion beam milling of glassy carbon molds for the thermal imprinting of quartz and borosilicate glasses. J. Micromech. Microeng. 16:2576–2584.
179. Youn SW, Takahashi M, Goto H, Kobayashi T, and Maeda R (2006) The effect of heat-treatment conditions on mechanical and morphological properties of a FIB-milled glassy carbon mold with micro patterns. J. Micromech. Microeng. 16:1277–1284.
180. Youn SW, Takahashi M, Goto H, Maeda R, and Kobayashi N (2006) AFM, SEM and Nano/micro-indentation studies of the FIB-milled glassy carbon surface heat-treated at different conditions. DTIP 2006: April 26–28, 2006.

181. Youn SW, Takahashi M, Goto H, and Maeda R (2006) Microstructuring of glassy carbon mold for glass embossing – Comparison of focused ion beam, nano/femtosecond-pulsed laser and mechanical machining. Microelectronic Eng. 83:2482–2492.
182. Youn SW, Takahashi M, Goto H, and Maeda R (2007) Fabrication of micro-mold for glass embossing using focused ion beam, femto-second laser, eximer laser and dicing techniques. J. Mater. Process. Technol. 187–188:326–330.
183. Chou SY, Krauss PR, and Renstrom PJ (1995) Imprint of sub-25 nm vias and trenches in polymers. Appl. Phys. Lett. 67:3114–3116.
184. Chou SY, Krauss PR, and Renstrom PJ (1996) Imprint Lithography with 25-Nanometer Resolution. Science 272:85–87.
185. Colburn M, Johnson S, Stewart M et al. (1999) Step and flash imprint lithography: a new approach to high-resolution patterning. Proc. SPIE. 3676:379–389.
186. Reyes DR, Iossifidis D, Auroux P, and Manz A (2002) Micro Total Analysis Systems. 1. Introduction, Theory and Technology. Anal. Chem. 74:2623–2636.
187. Auroux P, Iossifidis D, Reyes DR, and Manz A (2002) Micro total analysis systems. 2. Analytical standard operations and applications. Anal. Chem. 74:2637–2652.
188. Dittrich PS, Tachikawa K, and Manz A (2006) Micro total analysis systems. Latest advancements and trends. Anal. Chem. 78:3887–3907.
189. Janasek D, Franzke J, and Manz A (2006) Scaling and the design of miniaturized chemical-analysis systems. Nature. 442:374–380.
190. Rheea M and Burns MA (2008) Microfluidic assembly blocks. Lab Chip. 8:1365–1373.
191. Andersson H and van den Berg A (2003) Microfluidic devices for cellomics: a review. Sens. Actuators B: Chem. 92:315–325.
192. Chung TD and Kim HC (2007) Recent Advances in miniaturized microfluidic flow cytometry for clinical use. Electrophoresis. 28:4511–4520.
193. Duffy DC, McDonald JC, Schueller OJA, and Whitesides GM (1998) Rapid prototyping of microfluidic systems in poly(dimethylsiloxane). Anal. Chem. 70:4974–4984.
194. Xia Y and Whitesides GM (1998) Soft lithography. Ann. Rev. Mat. Sci. 28:153–184.
195. Zhao X, Xia Y, and Whitesides GM (1997) Soft lithographic methods for nano-fabrication. J. Mater. Chem. 7:1069–1074.
196. Anderson JR, Chiu DT, Jackman RJ et al. (2000) Fabrication of topologically complex three-dimensional microfluidic systems in PDMS by rapid prototyping. Anal. Chem. 72: 3158–3164.
197. Becker H and Gartner C (2000) Polymer microfabrication methods for microfluidic analytical applications. Electrophoresis. 21:12–26.
198. Becker H and Locascio LE (2002) Polymer microfluidic devices. Talanta. 56:267–287.
199. del Campo A and Arzt E (2008) Fabrication approaches for generating complex micro- and nanopatterns on polymeric surfaces. Chem. Rev. 108:911–945.
200. Izumi Y, Katoh M, Ohte T, Ohtani S, Kojima A, and Saitoh N (1996) Heating effects on modifying carbon surface by reactive plasma. Appl. Surf. Sci. 100–101:179–183.
201. Pohl HA (1978) Dielectrophoresis. Cambridge University Press, Cambridge.
202. Pohl HA (1958) Some effects of nonuniform fields on dielectrics. Appl. Phys. 29: 1182–1188.
203. Sanchis A, Brown AP, Sancho M et al. (2007) Dielectric characterization of bacterial cells using dielectrophoresis. Bioelectromagnetics. 28:393–401.
204. Minerick AR, Zhou R, Takhistov P, and Chang H-C (2003) Manipulation and characterization of red blood cells with alternating current fields in microdevices. Electrophoresis. 24:3703–3717.
205. Hughes MP, Morgan H, and Rixon FJ (2001) Dielectrophoretic manipulation and characterization of herpes simplex virus-1 capsids. Eur. Biophys. J. Biophys. Lett. 30:268–272.
206. Markx GH and Davey CL (1999) The dielectric properties of biological cells at radiofrequencies: applications in biotechnology. Enzyme Microb. Technol. 25:161–171.

207. Crane JS and Pohl HA (1968) A study of living and dead yeast cells using dielectrophoresis. J. Electrochem. Soc. 115:584–586.
208. Morgan H and Green NG (2003) AC Electrokinetics: Colloids and Nanoparticles. Research Studies Press LTD, Hertfordshire, England.
209. Ramos A, Morgan H, Green NG, and Castellanos A (1998) Ac electrokinetics: a review of forces in microelectrode structures. J. Phys. D.: Appl. Phys. 31:2338–2353.
210. Castellanos A, Ramos A, González A, Green NG, and Morgan H (2003) Electrohydrodynamics and dielectrophoresis in microsystems: scaling laws. J. Phys. D. 36:2584–2597.
211. Rousselet J, Markx GH, and Pethig R (1998) Separation of erythrocytes and latex beads by dielectrophoretic levitation and hyperlayer field-flow fractionation. Colloids and Surfaces A: Physiochem. Eng. Aspects. 140:209–216.
212. Hughes MP, Morgan H, Rixon FJ, Burt JPH, and Pethig R (1998) Manipulation of herpes simplex virus type 1 by dielectrophoresis. Biochimica et Biophysica Acta-General Subjects. 1425:119–126.
213. Becker FF, Wang X-, Huang Y, Pethig R, Vykoukal J, and Gascoyne PRC (1995) Separation of human breast cancer cells from blood by differential dielectric affinity. Proc. Natl. Acad. Sci. USA 92:860–864.
214. Flanagan LA, Lu J, Wang L et al. (2008) Unique dielectric properties distinguishing stem cells and their differentiated progeny. Stem Cells. 26:656–665.
215. Lapizco-Encinas BH, Simmons BA, Cummings EB, and Fintschenko Y (2004) Insulator-based dielectrophoresis for the selective concentration and separation of live bacteria in water. Electrophoresis 25:1695–1704.
216. Srivastava SK, Pullen SA, and Minerick AR (2008) Dielectrophoretic characterization of erythrocytes: Positive ABO blood types. Electrophoresis 29:5033–5046.
217. Cummings EB and Singh AK (2003) Dielectrophoresis in Microchips Containing Arrays of Insulating Posts: Theoretical and Experimental Results. Anal. Chem. 75:4724–4731.
218. Cummings EB and Singh AK (2000) Dielectrophoretic trapping without embedded electrodes.; September 18–19, 2000 Copyright 2003 SciSearch Plus. 4177:164–173.
219. Lapizco-Encinas BH, Ozuna-Chacón S, and Rito-Palomares M (2008) Protein manipulation with insulator-based dielectrophoresis and DC electric fields. J. Chromatogr. A 1206: 45–51.
220. Zheng LF, Brody JP, and Burke PJ (2004) Electronic manipulation of DNA, proteins, and nanoparticles for potential circuit assembly. Biosens. Bioelectron. 20:606–619.
221. Tracy NI and Ivory CF (2008) Protein separation using preparative-scale dynamic field gradient focusing. Electrophoresis 29:2820–2827.
222. Betts WB (1995) The potential of dielectrophoresis for the real-time detection of microorganisms in foods. Trends Food Sci. Technol. 6:51–58.
223. Klodzinska E and Buszewski B (2009) Electrokinetic detection and characterization of intact microorganisms. Anal. Chem. 81:8–15.
224. Markx GH, Huang Y, Zhou XF, and Pethig R (1994) Dielectrophoretic characterization and separation of microorganisms. Microbiology. 140:585–591.
225. Suzuki M, Yasukawa T, Shiku H, and Matsue T (2005) Separation of live and dead microorganisms in a micro-fluidic device by dielectrophoresis. Bunseki Kagaku. 54:1189–1195.
226. Castellarnau M, Errachid A, Madrid C, Juarez A, and Samitier J (2006) Dielectrophoresis as a tool to characterize and differentiate isogenic mutants of Escherichia coli. Biophys. J. 91:3937–3945.
227. Demierre N, Braschler T, Muller R, and Renaud P (2008) Focusing and continuous separation of cells in a microfluidic device using lateral dielectrophoresis. Sens. Actuators B: Chem. 132:388–396.
228. Vahey MD and Voldman J (2008) An equilibrium method for continuous-flow cell sorting using dielectrophoresis. Anal. Chem. 80:3135–3143.

229. Fatoyinbo HO, Hoettges KF, and Hughes MP (2008) Rapid-on-chip determination of dielectric properties of biological cells using imaging techniques in a dielectrophoresis dot microsystem. Electrophoresis. 29:3–10.
230. Gascoyne P and Vykoukal J (2004) Dielectrophoresis-based sample handling in general-purpose programmable diagnostic instruments. Proc. IEEE. 92:22–42.
231. Wang XB, Yang J, Huang Y, Vykoukal J, Becker FF, and Gascoyne PRC (2000) Cell separation by dielectrophoretic field-flow-fractionation. Anal. Chem. 72:832–839.
232. Gascoyne PRC, Wang XB, Huang Y, and Becker FF (1997) Dielectrophoretic separation of cancer cells from blood. IEEE Trans. Ind. Appl. 33:670–678.
233. Müller T, Fiedler S, Schnelle T, Ludwig K, Jung H, and Fuhr G (1996) High frequency electric fields for trapping of viruses. Biotechnol. Tech. 10:221–226.
234. Ermolina I, Milner J, and Morgan H (2006) Dielectrophoretic investigation of plant virus particles: Cow pea mosaic virus and tobacco mosaic virus. Electrophoresis. 27:3939–3948.
235. Grom F, Kentsch J, Müller T, Schnelle T, and Stelzle M (2006) Accumulation and trapping of hepatitis A virus particles by electrohydrodynamic flow and dielectrophoresis. Electrophoresis 27:1386–1393.
236. Berman D, Rohr ME, and Safferman RS (1980) Concentration of polio virus in water by molecular filtration. Appl. Environ. Microbiol. 40:426–428.
237. Hughes MP (2002) Strategies for dielectrophoretic separation in laboratory-on-a-chip systems. Electrophoresis. 23:2569–2582.
238. Hughes MP (2002) Nanoelectromechanics in Engineering and Biology. CRC Press, Boca Raton, FL.
239. Simmons BA, McGraw GJ, Davalos RV, Fiechtner GJ, Fintschenko Y, and Cummings EB (2006) The development of polymeric devices as dielectrophoretic separators and concentrators. MRS Bulletin 31:120–124.
240. Cummings EB (2003) Streaming dielectrophoresis for continuous-flow microfluidic devices. IEEE Eng. Med. Biol. Mag. 22:75–84.
241. Wang L, Flanagan L, and Lee AP (2007) Side-wall vertical electrodes for lateral field microfluidic applications. J. MEMS. 16:454–461.
242. Voldman J, Gray M, Toner M, and Schmidt M (2002) A Microfabrication-based Dynamic Array Cytometer. Anal. Chem. 74:3984–3990.
243. Illiescu C, Xu GL, Samper V, and Tay FEH (2005) Fabrication of a dielectrophoretic chip with 3D silicon electrodes. J. Micromech. Microeng. 15:494–500.
244. Fatoyinbo H, Kamchis D, Whattingham R, Ogin SL, and Hughes M (2005) A high-throughput 3-D composite dielectrophoretic separator. IEEE Trans. Biomed. Eng. 52: 1347–1349.
245. de Paula CC, Garcia Ramos A, da Silva AC, Cocchieri Botelho E, and Rezende MC (2002) Fabrication of glassy carbon spools for utilization in fiber optic gyroscopes. Carbon. 40: 787–788.
246. Iacono ST, Perpall MW, Wapner PG, Hoffman WP, and Smith Jr. DW (2007) Carbonization and thermal expansion of glassy carbon derived from bis-ortho-diynylarenes. Carbon 45:931–935.
247. Hull R (1999) Properties of Crystalline Silicon. The Institution of Engineering and Technology, London.
248. Anne A, Blanc B, Moiroux J, and Saveant JM (1998) Facile derivatization of glassy carbon surfaces by N-Hydroxysuccinimide esters in view of attaching biomolecules. Langmuir. 14:2368–2371.
249. Nowall WB, Wipf DO, and Kuhr WG (1998) Localized avidin/biotin derivatization of glassy carbon electrodes using SECM. Anal. Chem. 70:2601–2606.
250. Fleischmann M, Pons S, Rolison DR, and Schmidt PP (1987) Ultramicroelectrodes. Datatech Systems Inc. Morganton, NC.
251. Hadi M, Rouhollah A, Yousefi M, Taidy F, and Malekfar R (2006) Electrochemical Characterization of a pyrolytic carbon film electrode and the effect of anodization. Electroanalysis 18:787–792.

252. McCreery RL (2008) Advanced carbon electrode materials for molecular electrochemistry. Chem. Rev. 108:2646–2687.
253. Lawrence NS, Beckett EL, Davis J, and Compton RG (2002) Advances in the voltammetric analysis of small biologically relevant compounds. Anal. Biochem. 303:1–16.
254. Aoki K and Tanaka M (1989) Time-dependence of diffusion-controlled currents of a soluble redox couple at interdigitated microarray electrodes. J. Electroanal. Chem. 266:11–20.
255. Niwa O and Tabei H (1994) Voltammetric measurements of reversible and quasi-reversible redox species using carbon film based interdigitated array microelectrodes. Anal. Chem. 66:285–289.
256. Dam VAT, Olthuis W, and van den Berg A (2007) Redox cycling with facing interdigitated array electrodes as a method for selective detection of redox species. Analyst. 132: 365–370.
257. Bard AJ, Crayston JA, Kittlesen GP, Varco Shea T, and Wrighton MS (1986) Digital simulation of the measured electrochemical response of reversible redox couples at microelectrode arrays: consequences arising from closely spaced ultramicroelectrodes. Anal. Chem. 58:2321–2331.
258. Yang X and Zhang G (2005) Diffusion-controlled redox cycling at nanoscale interdigitated electrodes. Proceedings of the COMSOL Multiphysics Conference, Boston MA.
259. Iwasaki Y and Morita M (1995) Electrochemical Measurements with Interdigitated Array Microelectrodes Current Separations. Curr. Sep. 14:2–8.
260. Spegel C, Heiskanen A, Pedersen S, Emneus J, Ruzgas T, and Taboryski R (2008) Fully automated microchip system for the detection of quantal exocytosis from single and small ensembles of cells. Lab Chip. 8:323–329.
261. Spegel C, Heiskanen A, Skjolding LHD, and Emneus J (2008) Chip based electroanalytical systems for cell analysis. Electroanalysis 20:680–702.
262. Tabei H, Takahashi M, Hoshino S, Niwa O, and Horiuchi T (1994) Subfemtomole detection of catecholamine with interdigitated array carbon microelectrodes in HPLC. Anal. Chem. 66:3500–3502.
263. Fruchter L, Crepy G, and Le Mehaute A (1986) Batteries, identified fractal objects. J. Power Sources. 18:51–62.
264. Pajkossy T (1991) Electrochemistry at fractal surfaces. J. Electroanal. Chem. 300:1–11.
265. Whitesides GM and Grzybowski B (2002) Self-assembly at all scales. Science; Science. 295:2418–2421.
266. Maddison DS (1993) Fractal analysis of polypyrrole deposition. Synth. Met. 57:3544–3549.
267. Wang C, Zaouk R, and Madou M (2006) Local chemical vapor deposition of carbon nanofibers from photoresist. Carbon 44:3073–3077.
268. Khan GF and Wernet W (1997) Design of enzyme electrodes for extended use and storage life. Anal. Chem. 69:2682–2687.
269. de la Guardia M (1995) Biochemical sensors: The state of the art. Microchim. Acta. 120:243–255.
270. Gorton L (1995) Carbon paste electrodes modified with enzymes, tissues, and cells. Electroanalysis 7:23–45.
271. Heller A (1990) Electrical wiring of redox enzymes. Acc. Chem. Res. 23:128–134.
272. Mao F, Mano N, and Heller A (2003) Long tethers binding redox centers to polymer backbones enhance electron transport in enzyme “wiring” hydrogels. J. Am. Chem. Soc. 125:4951–4957.
273. Wang J and Angnes L (1992) Miniaturized glucose sensors based on electrochemical codeposition of rhodium and glucose oxidase onto carbon-fiber electrodes. Anal. Chem. 64:456–459.
274. Ciriello R, Cataldi T, Centonze D, and Guerrieri A (2000) Permselective behavior of an electrosynthesized, nonconducting thin film of poly(2-naphthol) and its application to enzyme immobilization. Electroanalysis. 12:825–830.
275. Vielstich W, Lamm A, and Gasteiger H (2003) Handbook of Fuel Cells: Fundamentals, Technology, Applications. John Wiley & Sons, Ltd. Chichester.

276. Tamaki T and Yamaguchi T (2006) High-surface-area three-dimensional biofuel cell electrode using redox-polymer-grafted carbon. Ind. Eng. Chem. Res. 45:3050–3058.
277. Arechederra RL, Treu BL, and Minteer SD (2007) Development of glycerol/O2 biofuel cell. J. Power Sources. 173:156–161.
278. Brunel L, Denele J, Servat K et al. (2007) Oxygen transport through laccase biocathodes for a membrane-less glucose/O2 biofuel cell. Electrochem. Commun. 9:331–336.
279. Lim KG and Palmore GTR (2007) Microfluidic biofuel cells: The influence of electrode diffusion layer on performance. Biosens. Bioelectron. 22:941–947.
280. Report on Basic Research Needs to Assure a Secure Energy Future (2003) U. S. Department of Energy. Available from http://www.science.doe.gov/bes/reports/list.html.
281. Thomas EV, Bloom I, Christophersen JP, and Battaglia VS (2008) Statistical methodology for predicting the life of lithium-ion cells via accelerated degradation testing. J. Power Sources. 184:312–317.
282. Sakaue E (2005) Micromachining/nanotechnology in direct methanol fuel cell. Digest IEEE Conference on MEMS: Miami Beach, FL, Jan 30–Feb 3 1:600–605.
283. Jankowski AF, Hayes JP, Graff RT, and Morse JD (2002) Micro-fabricated thin film fuel cells for portable power requirements. Materials Research Society Proceedings. San Francisco, CA, April 1–5 730:93–98.
284. Hayase M, Kawase T, and Hatsuzawa T (2004) Miniature 250 μm thick fuel cell with monolithically fabricated silicon eletrodes. Electrochem. Solid-State Lett. 7:A231–A234.
285. Modroukas D, Modi V, and Frechette LG (2005) Micromachined silicon structures for free-convection PEM fuel cells. J. Micromech. Microeng. 15:S193–S201.
286. Min KB, Tanaka S, and Esashi M (2002) MEMS-based polymer electrolyte fuel cell. Electrochemistry 70:924–927.
287. Kravitz SH, Apblett CA, Schmidt CF, Beggans MH, and Hecht AM (2002) A silicon micro fuel cell with a porous silicon nitride membrane electrode assembly. Abstracts of the Electrochemical Society Meeting: Salt Lake City, UT, October 20–25 1:708.
288. Kelley SC, Deluga GA, and Smyrl WH (2000) A miniature methanol/air polymer electrolyte fuel cell. Electrochem. Solid-State Lett. 3:407–409.
289. Lee SJ, Chang-Chien A, Cha SW et al. (2002) Design and fabrication of a micro fuel cell array with “flip-flop” interconnection. J. Power Sources. 112:410–418.
290. Motokawa S, Mohamedi M, Momma T, Shoji S, and Osaka T (2004) MEMS-based design and fabrication of a new concept micro direct methanol fuel cell (u-DMFC). Electrochem. Commun. 6:562–565.
291. D′Arrigo G, Spinella C, Arena G, and Lorenti S (2003) Fabrication of miniaturized Si-based electrocatalytic membranes. Mater. Sci. Eng. C. 23:13–18.
292. Erdler G, Frank M, Lehmann M, Reinecke H, and Muller C (2006) Chip integrated fuel cell. Sensor Actuat. A-Phys. 132:331–336.
293. Meyers JP and Maynard HL (2002) Design considerations for miniaturized PEM fuel cells. J. Power Sources 109:76–88.
294. Kuriyama N, Kubota T, Okamura D, Suzuki T, and Sasahara J (2008) Design and fabrication of MEMS-based monolithic fuel cells. Sensor Actuat. A-Phys. 145–146:354–362.
295. Dyer CK (2002) Fuel cells for portable applications. J. Power Sources 106:31–34.
296. Park BY and Madou MJ (2006) Design, fabricaion, and initial testing of a miniature PEM fuel cell with micro-scale pyrolyzed carbon fluidic plates. J. Power Sources 162:369–379.
297. Gottesfeld S and Wilson MS (2000) Polymer electrolyte fuel cells as potential power sources for portable electronic devices. In: Osaka T and Datta M (eds) Energy Storage Systems for Electronics Devices, Gordon and Breach Science Publishers, Singapore.
298. Arico AS, Srinivasan S, and Antonucci V (2001) DMFCs: from fundamental aspects to technology development. Fuel Cells 1:133–161.
299. Müller J, Frank G, Colbow K, and Wilkinson D (2003) Transport/kinetic limitations and efficiency losses. In: Vielstich W, Gasteiger HA, and Lamm A (eds) Handbook of Fuel Cells, John Wiley and Sons Ltd., England.

300. Neergat M, Friedrich KA, and Stimming U (2003) New material for DMFC MEAs. In: Vielstich W, Gasteiger HA, and Lamm A (eds) Handbook of Fuel Cells, John Wiley and Sons Ltd., England.
301. Narayanan SR, Valdez TI, and Rohatgi N (2003) DMFC system design for portable applications. In: Vielstich W, Gasteiger HA, and Lamm A (eds) Handbook of Fuel Cells, John Wiley and Sons Ltd., England.
302. Lu G and Wang CY (2004) Two-phase microfluidics, heat and mass transport in direct methanol fuel cells. In: Sunden B and Faghri M (eds) Transport Phenomena in Fuel Cells, WIT Press, Boston, MA.
303. Gottesfeld S (2007) Polymer electrolyte and direct methanol fuel cells. In: Bard AJ and Stratman M (eds) Encyclopedia of Electrochemistry, John Wiley and Sons Ltd., Weinheim.
304. Shaffer CE and Wang CY (2009) Performance modeling and cell design for high concentration methanol fuel cells. In: Vielstich W, Yokokawa H, and Gasteiger HA (eds) Advances in Electrocatalysis, Materials, Diagnostics and Durability, John Wiley and Sons Ltd., England.
305. Choban ER, Markoski LJ, Wieckowski A, and Kenis PJA (2004) Microfluidic fuel cell based on laminar flow. J. Power Sources. 128:54–60.
306. Kjeang E, McKechnie J, Sinton D, and Djilali N (2007) Planar and three-dimensional microfluidic fuel cell architectures based on graphite rod electrodes. J. Power Sources. 168:379–390.
307. Kjeang E, Djilali N, and Sinton D (2009) Microfluidic fuel cells: A review. J. Power Sources. 186:353–369.
308. Li A, Chan SH, and Nguyen NT (2007) A laser-micromachined polymeric membraneless fuel cell. J. Micromech. Microeng. 17:1107–1113.
309. Litster S and Djilali N (2008) Theoretical performance analysis of microstructured air-breathing fuel cells. Electrochem. Solid-State Lett. 11:B1–B5.
310. Jiang Y, Wang X, Zhong L, and Liu L (2006) Design, fabrication and testing of a silicon-based air-breathing micro direct methanol fuel cell. J. Micromech. Microeng. 16:S233–S239.
311. Cao J, Zou Z, Huang Q et al. (2008) Planar air-breathing micro-direct methanol fuel cell stacks based on micro-electronic-mechanical-system technology. J. Power Sources. 185:433–438.
312. Chiao M, Lam K, and Lin L (2006) Micromachined microbial and photosynthethic fuel cells. J. Micromech. Microeng. 16:2547–2553.
313. Barton SC, Gallaway J, and Atanassov P (2004) Enzymatic biofuel cells for implantable and microscale devices. Chem. Rev. 104:4867–4886.
314. Kerzenmacher S, Ducree J, Zengerle R, and von Stetten F (2008) Energy harvesting by implantable abiotically catalyzed glucose fuel cells. J. Power Sources. 182:1–17.
315. Moriuchi T, Morishima K, and Furukawa Y (2008) Improved power capability with pyrolyzed carbon electrodes in micro direct photosynthetic/metabolic bio-fuel cell. Int. J. Precision Eng. Manuf. 9:23–27.
316. Topcagic S and Minteer SD (2006) Development of a membraneless ethanol/oxygen biofuel cell. Electrochim. Acta. 51:2168–2172.
317. O'Hayre R, Braithwaite D, Hermann W et al. (2003) Development of portable fuel cell arrays with printed-circuit technology. J. Power Sources. 124:459–472.
318. More KL and Reeves KS (2005) Microstructural characterization of PEM fuel cell MEAs. DOE Hydrogen Program Annual Merit Review Proceedings: Arlington, VA, May 23–26 1.
319. Gottesfeld S and Zawodzinski TA (1997) Polymer electrolyte fuel cells. In: Tobias C (ed) Advances in Electrochemical Science and Engineering, Wiley and Sons, New York.
320. Eikerling M, Kornyshev AA, and Kulikovsky AA (2007) Physical modeling of cell components, cells and stacks. In: Macdonald DD and Schmuki P (eds) Encyclopedia of Electrochemistry, VCH-Wiley, Weinheim.
321. Eikerling M, Kornyshev AA, and Kulikovsky AA (2006) Water in polymer electrolyte fuel cells: Friend or foe? Phys. Today. 59:38–44.

322. Debe MK (2003) Novel catalysts, calatyst support and catalysts coated membrane methods. In: Vielstich W, Lamm A, and Gasteiger HA (eds) Handbook of Fuel Cells – Fundamentals, Technology and Applications, John Wiley and Sons Ltd., England.
323. Debe MK, Schmoeckel AK, Vernstrom GD, and Atanasoski R (2006) High voltage stability of nanostructured thin film catalysts for PEM fuel cells. J. Power Sources. 161:1002–1011.
324. Mukherjee PP, Sinha PK, and Wang CY (2007) Impact of gas diffusion layer structure and wettability on water management in polymer electrolyte fuel cells. J. Mater. Chem. 17:3053–3089.
325. Mathias MF, Roth J, Fleming J, and Lehnert W (2003) Diffusion media materials and characterization. In: Lietsich W, Lamm A, and Gasteiger HA (eds) Handbook of Fuel Cells – Fundamentals, Technology and Applications, John Wiley and Sons Ltd., Chicester.
326. Weber AZ and Darling RM (2007) Understanding porous water transport plates in polymer-electrolyte fuel cells. J. Power Sources. 168:191–199.
327. Wang CY (2004) Fundamental models for fuel cell engineering. Chem. Rev. 104:4727–4766.
328. Wang CY (2003) Two-phase flow and transport. In: Anonymous (ed) Handbook of Fuel Cells – Fundamentals, Technology and Applications, John Wiley and Sons Ltd., Chicester.
329. Lin P, Park BY, and Madou MJ (2008) Development and characterization of a miniature PEM fuel cell stack with carbon bipolar plates. J. Power Sources. 176:207–214.
330. Mukherjee PP (2007) Pore-Scale Modeling and Analysis of the Polymer Electrolyte Fuel Cell Catalyst Layer. PhD Dissertation, The Pennsylvania State University.
331. Mukherjee PP and Wang CY (2008) A Catalyst layer Flooding Model for Polymer Electrolyte Fuel Cells. Proceedings of ASME Fuel Cell 2008: Denver, CO, June 16–18 1.
332. Prasher RS, Hu XJ, Chalopin Y et al. (2009) Turning carbon nanotubes from exceptional heat conductors into insulators. Phys. Rev. Lett. 102:105901–105904.
333. Lee SW, Kim B, Chen S, Shao-Horn Y, and Hammond PT (2009) Layer-by-Layer assembly of all carbon nanotube ultrathin films for electrochemical applications. J. Am. Chem. Soc. 131:671–679.
334. Mano N, Mao F, and Heller A (2003) Characteristics of a miniature compartment-less Glucose–O2 biofuel cell and its operation in a living plant. J. Am. Chem. Soc. 125:6588–6594.
335. Klotzbach T, Watt M, Ansari Y, and Minteer SD (2006) Effects of hydrophobic modification of chitosan and Nafion on transport properties, ion-exchange capacities, and enzyme immobilization. J. Membr. Sci. 282:276–283.
336. Barton SC, Sun Y, Chandra B, White S, and Hone J (2007) Mediated enzyme electrodes with combined micro- and nanoscale supports. Electrochem. Solid-State Lett. 10:B96–B100.